



**Politecnico
di Torino**

**Numerical Modeling to Support the Development
of Structural Damage Detection Systems in
Prestressed Concrete Bridges**

A MASTER'S THESIS

BY

Enzo Antezana Pierinelli

MASTER OF SCIENCE IN CIVIL ENGINEERING
STRUCTURES

October 2024

*Numerical Modeling to Support the Development
of Structural Damage Detection Systems in
Prestressed Concrete Bridges*

A Master's Thesis

by

Enzo Antezana Pierinelli

Supervised by:

Prof. Giulio Ventura

Prof. Mauro Corrado

Acknowledgments

I would like to sincerely thank my advisors, Professors Giulio Ventura and Mauro Corrado, for their invaluable support and guidance throughout this research path. I have gained so much knowledge working with them, and their mentorship has made this entire process both enriching and enjoyable. Their insights were essential to the development of this work.

I would also like to thank my family, particularly my sister Fiorenza, with whom I share a deep love of learning. Even though our academic paths are quite different, her companionship and support throughout this process have been incredibly important to me and to the completion of this work.

Abstract

This thesis advances the field of structural engineering by developing advanced numerical models to simulate the behavior of prestressed concrete beams, specifically focusing on the dynamics of steel tendon breakage. Employing the Finite Element Method (FEM) through LS-DYNA, the present study integrates both implicit and explicit analysis methods to achieve a detailed representation of steel and concrete interactions under stress and failure conditions.

The research begins with the application of prestress to the steel tendon, followed by an implicit analysis aimed at establishing a static solution for the interaction between the steel and concrete parts. This phase is critical for understanding the pre-failure stress distribution within the beam. Subsequently, an explicit analysis introduces a simulated tendon rupture, employing a cohesive contact model to effectively simulate the slippage effect between steel and concrete. This model accounts for realistic interaction dynamics, crucial for assessing changes in acceleration and other dynamic responses, which are essential for SHM systems to detect and accurately recognize failure events.

The explicit phase is particularly focused on capturing the propagation of acceleration waves following tendon breakage, a phenomenon that has significant implications for real-time structural health monitoring and predictive maintenance. Through the results, findings suggest the following conclusions:

FEM as a Predictive Tool: FEM proves to be an effective approach for generating synthetic data post steel tendon breakage. This technique accurately simulates the dynamics of acceleration wave propagation, ensuring that the synthetic data closely resemble real-life behaviors in prestressed concrete beams.

Insights into Structural Dynamics: The model's ability to capture the immediate effects of tendon breakages provides critical insights into the dynamic responses of prestressed concrete structures. The data collected and analyzed from the numerical simulations provide a valuable dataset for developing advanced monitoring technologies that detect and respond to failures in real time, thereby enhancing the safety and durability of critical infrastructure elements.

Keywords: *Finite Element Method (FEM), Prestressed Concrete, LS-DYNA, Structural Health Monitoring, Steel Tendon Breakage, Wave Propagation, Cohesive Contact Model, Implicit Analysis, Explicit Analysis*

Contents

1	Introduction	7
1.1	Background and Significance	7
1.2	Prestressed Concrete Overview	8
1.3	Structural Health Monitoring	9
1.4	Objectives	10
2	Literature Review	11
2.1	Finite Element Method in Prestressed Concrete Structures	11
2.2	Wire breakage monitoring	13
2.3	Proposed Methodology	14
3	Theoretical Framework	17
3.1	Finite Element Method	17
3.1.1	Theoretical Notes on FEM	18
3.1.2	FEM Analysis phases	21
3.2	Time Integration Algorithms	22
3.2.1	Explicit Analysis	22
3.2.2	Implicit Analysis	24
3.3	Wave Propagation in Materials	24
3.3.1	Governing Equations	25
3.3.2	Types of Waves in Solids	25
4	On LS-DYNA & Model Development Basis	27
4.1	Model Development	27
4.2	Detailed Software Considerations	27
4.2.1	Contact Types	27
4.2.2	Element Formulation	29
4.2.3	Element Size	32
4.2.4	Damping	33

4.2.5	Mesh Control	33
4.2.6	Time step	35
5	Finite Element Model	37
5.1	Finite Element Models	37
5.1.1	Geometry	37
5.1.2	Mesh Generation	39
5.1.3	Material Properties	40
5.1.4	Contact Definition	41
5.1.5	Prestressing Load	42
5.1.6	Damping Definition	43
6	Results	45
6.1	Overview of the Analysis	45
6.2	Type of Results and Relevance	46
6.3	Results	47
6.3.1	Nodal Accelerations - Concrete Boundary	48
6.3.2	Nodal Accelerations - Steel Boundary	53
6.3.3	Slippage behavior - Steel separation	56
7	Model & Data Validation	60
7.1	Mesh	60
7.1.1	Mesh Control Parameters Verification	60
7.1.2	Mesh Sensitivity	64
7.2	Energy Balance	71
7.3	Data Validation	74
7.3.1	Experimental Results	74
7.3.2	Comparison Between Experimental and Numerical Data	77
8	Conclusion and Recommendations	79
8.1	Summary of Findings	79
8.2	Study Limitations	81
8.3	Practical Applications	82
8.4	Recommendation for Future Research	82
	Appendix Legend	87
A	Input Cards on LS-DYNA	88
B	Nodal Accelerations	91

List of Figures

1.1	SHM task [2]	10
3.1	General 3-dimensional body [15]	19
4.1	Bilinear cohesive mixed-mode law	29
4.2	Four node tetrahedron	30
4.3	Tetrahedral Aspect Ratio Calculation	35
5.1	Geometrical properties of the prestressed RC beam	38
5.2	Meshed geometry - Model 1	39
5.3	Meshed geometry - Model 2	40
5.4	Bilinear cohesive law	42
6.1	Points for data recollection - Model 1	47
6.2	Acceleration of concrete node A, $\zeta = 0\%$ - Model 1	48
6.3	Acceleration of concrete node A, $\zeta_K = 2\%$ - Model 1	49
6.4	Acceleration of concrete node A, $\zeta_K = 4\%$ - Model 1	49
6.5	Acceleration of concrete node A, $\zeta_M = 2\%$ - Model 1	50
6.6	Acceleration of concrete node A, $\zeta_M = 4\%$ - Model 1	50
6.7	Acceleration of concrete node A, $\zeta_M = 2\%$, $\zeta_K = 2\%$ - Model 1	51
6.8	Acceleration of concrete node A, $\zeta_M = 4\%$, $\zeta_K = 4\%$ - Model 1	51
6.9	Acceleration of concrete node A, $\zeta_M = 4\%$, $\zeta_K = 4\%$ - Model 2	52
6.10	Acceleration of concrete node B, $\zeta_M = 4\%$, $\zeta_K = 4\%$ - Model 2	52
6.11	Acceleration of concrete node C, $\zeta_M = 4\%$, $\zeta_K = 4\%$ - Model 2	53
6.12	Acceleration of steel node - Model 1	54
6.13	Acceleration of steel node - Model 2	55
6.14	Trimmed acceleration of steel node - Model 2	56
6.15	Steel parts separation - Model 1	57
6.16	Steel parts separation - Model 2	58
7.1	Element Jacobians	61

7.2	Element Jacobians Histogram	61
7.3	Aspect ratio results	62
7.4	Aspect Ratio Histogram	62
7.5	Skewness results	63
7.6	Skewness Histogram	64
7.7	Acceleration Models 1, 2 and 3	65
7.8	Acceleration Models 4 and 5	66
7.9	Energy Components Variation - Model 1	68
7.10	Energy Components Variation - Model 1	68
7.11	Energy Components Variation - Model 1	69
7.12	Energy Components Variation - Model 1	69
7.13	Energy Components Variation - Model 1	70
7.14	Energy Components Variation - Model 1	70
7.15	Energy Components Comparison - Model 1 and 6	71
7.16	Energy components - Model 2	73
7.17	Energy Balance - Model 2	73
7.18	Acceleration - Experimental dataset 1	75
7.19	Acceleration - Experimental dataset 2	75
7.20	Acceleration - Experimental dataset 3	75
7.21	Acceleration - Experimental dataset 4	75
7.22	Acceleration - Experimental dataset 5	76
7.23	Acceleration - Experimental dataset 6	76
7.24	Acceleration - Experimental dataset 7	76
7.25	Acceleration - Experimental dataset 8	76
7.26	Acceleration - Experimental dataset 9	77
7.27	Acceleration - Experimental dataset 10	77
1	Acceleration of node A, $\zeta = 0\%$	91
2	Acceleration of node B, $\zeta = 0\%$	92
3	Acceleration of node C, $\zeta = 0\%$	92
4	Acceleration of node A, $\zeta_K = 2\%$	93
5	Acceleration of node B, $\zeta_K = 2\%$	94
6	Acceleration of node C, $\zeta_K = 2\%$	94
7	Acceleration of node A, $\zeta_K = 4\%$	95
8	Acceleration of node B, $\zeta_K = 4\%$	96
9	Acceleration of node C, $\zeta_K = 4\%$	96
10	Acceleration of node A, $\zeta_M = 2\%$	97

11	Acceleration of node B, $\zeta_M = 2\%$	98
12	Acceleration of node C, $\zeta_M = 2\%$	98
13	Acceleration of node A, $\zeta_M = 4\%$	99
14	Acceleration of node B, $\zeta_M = 4\%$	100
15	Acceleration of node C, $\zeta_M = 4\%$	100
16	Acceleration of node A, $\zeta_M = 2\%$, $\zeta_K = 2\%$	101
17	Acceleration of node B, $\zeta_M = 2\%$, $\zeta_K = 2\%$	102
18	Acceleration of node C, $\zeta_M = 2\%$, $\zeta_K = 2\%$	102
19	Acceleration of node A, $\zeta_M = 4\%$, $\zeta_K = 4\%$	103
20	Acceleration of node B, $\zeta_M = 4\%$, $\zeta_K = 4\%$	104
21	Acceleration of node C, $\zeta_M = 4\%$, $\zeta_K = 4\%$	104

List of Tables

5.1	Concrete material characterization	41
5.2	Steel material characterization	41
5.3	Tiebreak contact characterization	42
5.4	Prestressing load definition	43
5.5	Damping types and values for different models	43
7.1	Sensitivity Analysis Models	65
7.2	Time Domain Sensitivity Results	66
7.3	Frequency Domain Sensitivity Results	67
7.4	Energy data	72

Chapter 1

Introduction

1.1 Background and Significance

Prestressed concrete technology has been gaining significance and being widely used in a variety of structural applications. This method has proven particularly effective for structures requiring a larger span-to-depth ratio, such as bridges and viaducts, due to its ability to accelerate construction timelines and enhance overall performance. Furthermore, by employing prestressed concrete, there is a notable improvement in the mechanical performance of structural members, which helps in significantly reducing cracking, increasing stiffness and enhancing the durability of constructions.

Structural failures pose severe risks, with bridge collapses providing clear examples of the potential consequences. These incidents not only lead to significant economic losses and disruptions but also, more critically, to loss of life. Such failures underscore the vital importance of both designing and continuously monitoring structural elements, especially in the case of prestressed concrete members. Various factors can precipitate these failures, from design flaws and material fatigue to improper maintenance practices. Therefore, it is of crucial importance that these structures are not only designed based on the criteria stated in the design codes but also subject to rigorous ongoing inspections and maintenance. Implementing robust monitoring systems can help detect early signs of distress in prestressed concrete structures, thereby preventing deterioration and averting potential collapses. Ensuring the safety and integrity of these critical infrastructures is essential, making the development of effective predictive tools and methodologies a priority in the field of structural engineering.

While prevention of structural failures is a fundamental aspect of engineering, un-

derstanding the dynamics that occur after such failures is equally critical. This knowledge can significantly enhance the resilience of infrastructure by contributing to more effective response strategies and recovery plans. In the field of prestressed concrete, where failures can have profound implications, accurately simulating and predicting the behavior following tendon breakage is essential. This approach not only helps in assessing the immediate impacts, but also in comprehending the behaviors leading up to a total collapse, so that preventive actions can be implemented. By focusing on the post-failure behavior of these structures, this research aims to contribute to safer, more reliable engineering practices, ultimately leading to structures that are better equipped to handle this kind of stress.

1.2 Prestressed Concrete Overview

Concrete is inherently strong in compression but weak in tension, with compressive strength approximately ten times greater than its tensile strength. Under flexural loading, cracks can rapidly form in concrete members. To mitigate this, steel is introduced into the tensile zone of the member, applying a longitudinal force that considerably reduces crack formation. This not only enhances the bending, shear, and torsional capacity of the section but also optimizes the utilization of concrete's compressive properties. The applied longitudinal force, known as the prestressing force, is introduced by tensioning the steel tendons before external loads are applied to the member.

Prestressing systems are primarily categorized into two types: pre-tensioning and post-tensioning. In pre-tensioning, the steel tendons are tensioned before the concrete is poured. This is achieved through the use of anchorages that are supported by bulkheads, capable of sustaining the high tension forces exerted on the tendons. This process can involve tensioning individual steel strands or simultaneous tensioning of all strands in one jacking operation [1].

On the other hand, post-tensioning involves tensioning the strands after the concrete has hardened. This method requires the installation of special ducts along the longitudinal axis of the concrete member, facilitating the tensioning of the strands once the concrete has hardened. There are two main variations in post-tensioning: bonded, where corrugated steel ducts are filled with cementitious grout to secure the strands, and unbonded, which uses grease to allow relative movement of the strand within the structural member.

Prestressed concrete is extensively utilized in structures requiring large span-to-

depth ratios, such as bridges and large-span buildings. While this technology offers significant structural advantages, it also presents unique challenges, particularly regarding the corrosion and deterioration of the steel tendons. These issues are more critical in prestressed concrete than in non-prestressed elements because the structural strength of prestressed concrete members is directly dependent on the prestressing force, which in turn is function of the area of the prestressing tendons [1]. Consequently, any compromise in tendon integrity can significantly impact the overall durability and safety of the structure, underscoring the importance of thorough monitoring and maintenance to prevent such deterioration.

The prestressing load should be high enough to be able to compensate for the losses in concrete given by high creep, and shrinkage. For this, high-strength steel is used to provide such high stresses, with values of initial prestressing range in the order of 1000 MPa [1].

Failures in these structural elements, especially in critical infrastructure like bridges, have a profoundly negative impact. One common mode of failure is tendon breakage, often initiated by corrosion. Corrosion can occur under various conditions, such as exposure to atmospheric condition, stress, or temperature variations, making control of these parameters is crucial for maintaining structural integrity. The prestressing elements, composed of high-tensile steel wires unified form tendons, these are crucial to the structure's strength. It is important to note that the failure of a single wire or tendon does not necessarily result in the collapse of the entire structural member or structure, but it could significantly compromise its integrity and safety.

1.3 Structural Health Monitoring

Structural Health Monitoring (SHM) is essentially the integration of traditional experimental and theoretical structural mechanics with electronics, material science, and information and communication technologies [2]. Is a vital process in civil engineering that involves the continuous observation, evaluation, and analysis of a structure's condition to ensure its safety, functionality, and longevity. Structural health monitoring uses sensors and data processing techniques to detect, analyze, and interpret changes in a structure's condition, enabling the early identification of damage, deterioration, or failure. In essence, SHM allows for timely maintenance, reduces the risk of catastrophic failure, and extends the lifespan of critical infrastructure. SHM can be understood as a tool performing the task shown in Figure 1.1, where the lifetime functions represent a priori assumed decay of the performance index starting from the

design value [2].

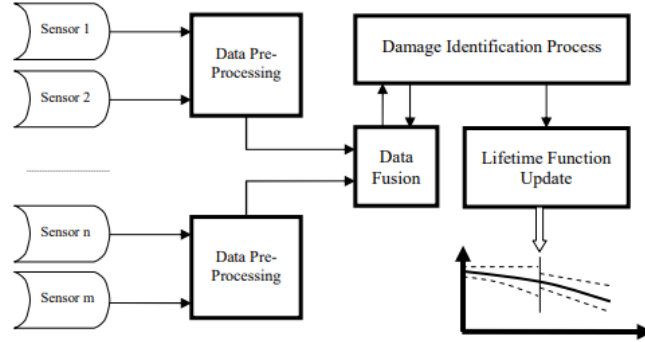


Figure 1.1: SHM task [2]

In this study, the focus is on developing a numerical model to simulate the behavior of a prestressed concrete beam following the breakage of a steel tendon. While SHM could utilize this approach to monitor the condition of the beam by detecting changes through wave propagation, the primary goal here is to generate data and insights that can support such applications. Understanding wave propagation patterns in materials, as explored in this thesis, provides essential information that can be used in future SHM efforts to identify and assess damage more effectively, potentially enhancing the early detection of failures and improving structural safety

1.4 Objectives

The primary objective of this thesis is to analyze and understand the post-breakage behavior of prestressed concrete beams following steel tendon rupture. To achieve this, several advanced numerical models are developed using the Finite Element Method (FEM), facilitated through the use of LS-DYNA. The specific objectives to fulfill this goal include:

- **Developing a Numerical Model:** Construct an accurate numerical model using LS-DYNA that incorporates advanced meshing techniques, detailed contact definition, and in general comprehensive modeling parameters. This model will accurately represent the behavior of real structural members, capturing the essential dynamics of prestressed concrete beams post-tendon rupture.
- **Analyzing and Wave Propagation:** Utilize both implicit and explicit FEM analysis to investigate the wave propagation within prestressed concrete beams under failure conditions. This analysis aims to provide a deeper understanding of the structural impacts of tendon breakage, specifically in wave propagation.

Chapter 2

Literature Review

2.1 Finite Element Method in Prestressed Concrete Structures

The Finite Element Method (FEM) is a powerful computational tool widely used in engineering to simulate and analyze complex physical phenomena and geometries. FEM has evolved from a modest method for solving simple structural problems into a sophisticated, versatile technique capable of addressing a wide range of engineering challenges. This section reviews its application in structural engineering, particularly focused on its role in analyzing the behavior of prestressed concrete structures, damage and failure mechanisms.

FEM is implemented through various finite element software platforms, which incorporate numerical models designed to represent the real behavior of structural elements. Some of the earliest work done by Faherty in 1972 utilized FEM to analyze both reinforced and prestressed concrete beams, incorporating nonlinear concrete properties and a linear bond-slip relationship [3]. This early application highlighted the method's capacity to account for complex material interactions and provided a foundational understanding of how prestressed concrete behaves under various load conditions.

Nonlinear finite element analysis (FEA) techniques are fundamental in modeling the complex behavior of prestressed concrete structures under various loading conditions. Mang and Meschke (1991) [4] provide a comprehensive review of the development of these techniques. Their study introduces significant advancements, such as the "smeared-crack concept," which allows for practical large-scale analyses

of concrete structures under ultimate load. They emphasize the importance of tension stiffening due to bond slip between concrete and steel reinforcement, which plays a crucial role in predicting structural behavior accurately, especially under complex loading as thermal gradients and wind loads. The introduction of a nonlocal failure criterion for concrete further enhances the precision of failure predictions in finite element models. The authors highlight the necessity of incorporating realistic material models to improve the reliability of structural assessments under diverse loading conditions.

In a complementary approach, Lee and Fenves (1998) [5] propose a plastic-damage model adjusted for concrete structures subjected to cyclic loading. This model integrates fracture-energy-based damage mechanics with stiffness degradation to simulate the material's response under various loading conditions. It uses two damage variables, one for tensile damage and another for compressive damage, allowing a separate representation of damage change in tension and compression. The model also accounts for stiffness recovery during unloading, effectively simulating crack closure and reopening under cyclic loads. Numerical simulations demonstrate the model's capacity to capture the behavior of concrete structures under both monotonic and cyclic loading, providing accurate predictions of stiffness degradation and recovery due to microcrack formation and closure.

Accurately modeling the bond-slippage behavior between steel reinforcement and concrete is crucial for understanding the performance of prestressed concrete structures. Arab, Badie, and Manzari (2011) [6] offer a detailed study of this behavior through two primary FEM techniques: the extrusion technique and the embedment technique. The extrusion technique employs friction-based contact simulations to capture detailed local effects, such as bond slippage, effectively simulating nonlinear stress variations and local phenomena like slippage and pressure at the interface. However, this method is computationally expensive. In contrast, the embedment technique, though less detailed, provides an efficient approximation of the overall response, making it suitable for broader applications where computational resources are limited. The study also identifies optimal friction coefficients and notes that bond stresses follow a nonlinear distribution rather than the linear approximation often assumed in practice.

Continuing on this topic, Yapar et al. (2015) [7] develop an advanced nonlinear finite element model specifically for pretensioned prestressed concrete beams, which incorporates plasticity and damage behavior of concrete along with slip-bond failure mechanisms of strands. Their model, validated against experimental data, accurately

captures interfacial bond characteristics, bond-slip behavior, and damage evolution at the concrete-steel interface. It effectively predicts stress transfer mechanisms such as adhesion, friction, and the Hoyer effect, demonstrating its importance in assessing the performance of prestressed beams throughout their service life and after repair.

Padmarajaiah and Ramaswamy (2002) [8] focus on the bond-slip behavior in prestressed concrete beams reinforced with steel fibers. Their FEM analysis study the effects of varying prestressing levels, fiber volume fractions, and fiber locations. The study finds that the strategic placement of steel fibers, particularly over partial depths on the tensile side, enhances both the flexural capacity and ductility of the beams. The research highlights the importance of considering bond-slip effects in the design of prestressed beams to optimize their structural performance, offering insights into the effective placement of reinforcement for enhanced load-bearing capacity.

2.2 Wire breakage monitoring

Monitoring wire breakage in prestressed concrete structures is crucial for ensuring their safety and structural integrity. The development of effective monitoring techniques has gained significant attention in recent years due to the need for early detection and prevention of catastrophic failures. This subchapter reviews key studies that have advanced the field of wire breakage monitoring, emphasizing the relevance of integrating these methods with finite element modeling (FEM) to assess post-breakage behavior.

Recent research has focused on utilizing acoustic event detection and machine learning techniques to monitor wire breakage in prestressed concrete structures effectively. Farhadi et al. (2023) [9] propose a novel approach using sound event detection (SED) techniques to identify wire breakage events in prestressed concrete bridges. This method leverages Mel-frequency cepstral coefficients (MFCCs) to extract acoustic features from the signals generated during wire breakage, which are then classified using a back-propagation neural network (BPNN). Experimental validation using data from two bridges in Italy demonstrated that the combination of MFCCs and BPNN provides accurate real-time monitoring and diagnosis of bridge safety. This method offers significant advantages over traditional approaches by enabling continuous, automated, and non-invasive monitoring, even in noisy environments, potentially leading to safer and more durable infrastructure.

Building on this approach, Farhadi et al. (2024) [10] introduce an innovative method for automated monitoring of prestressing tendon breakage in concrete bridges,

utilizing acoustic event detection and classification (AE/DC). This study employs advanced signal processing techniques and deep learning models, such as pretrained convolutional neural network (CNN) architectures (e.g., VGG19, ResNet50, Inception, Xception), enhanced with a Bottleneck Attention Mechanism to improve classification performance. Additionally, the authors developed a custom hybrid model, AcousticNet, which incorporates dilated convolutional layers, gated recurrent units, and multihead attention mechanisms to enhance event classification accuracy. The proposed models were validated through extensive laboratory and real-world data, demonstrating robustness and adaptability in real-time structural health monitoring scenarios. This advancement marks a significant step forward in integrating deep learning with signal processing, providing a reliable, non-invasive method for the early detection of wire breakage in prestressed concrete structures.

Acoustic Emission (AE) techniques are widely recognized for their effectiveness in detecting crack formation and damage in concrete structures. The work by the RILEM Technical Committee (2010) [11], [12] and [13] underscores the critical role of AE and related non-destructive evaluation (NDE) techniques in crack detection and damage evaluation of concrete structures. The guidelines emphasize the importance of AE data in monitoring and assessing the integrity of concrete under in-service conditions, highlighting its ability to detect elastic waves generated by dynamic events, such as crack nucleation, delamination, and micro-crack formation. The study outlines methods for measuring AE signals, including parameters like peak amplitude, rise time, and duration, which are essential for classifying and quantifying crack activity. Additionally, the guidelines propose a standardized approach for the classification of active cracks and damage qualification using AE, providing early warning of structural deterioration. These recommendations highlight the value of AE techniques for real-time, continuous monitoring of concrete structures, thus enhancing safety and enabling proactive maintenance strategies.

2.3 Proposed Methodology

Significant research has been conducted in the field of structural behavior analysis using the Finite Element Method (FEM) as a predictive tool to understand various behaviors within the field of prestressed concrete. However, despite these advancements, there remains a notable gap in the literature specifically concerning the development of insights into the post-breakage phenomenon. Particularly, the wave propagation and subsequent behaviors following steel tendon rupture are not extensively studied. This research aims to address this gap by focusing on the detailed simulation of these

specific dynamics, providing new insights into the structural responses post-tendon failure.

Understanding the dynamic response of prestressed concrete beams following tendon rupture requires a carefully designed methodological approach. The methodology of this thesis is focused on creating detailed numerical simulation models using Finite Element Method (FEM) in LS-DYNA. These simulations are designed to accurately model the post-breakage behavior of the prestressed concrete beams and investigate wave propagation and structural dynamics in response to tendon rupture.

The methodology is based on several key components:

1. **Numerical Model development:** The numerical model is elaborated in LS-DYNA using linear elastic material definitions for both the concrete and steel components. Prestressing is applied as an initial stress state to the steel tendons. The meshing process is adjusted to the specific needs of the analysis, with mesh size being determined by the maximum frequency of interest. A denser mesh is used near the steel tendon rupture area due to the smaller geometry, allowing for an accurate representation of stress concentrations. Uniform tetrahedral elements are applied across the model to maintain consistency.
2. **Wave Propagation Simulation:** Simulating wave propagation after the tendon rupture begins with an implicit analysis, designed to reach an equilibrated state for the initial stress condition. This equilibrated solution is then used as the starting configuration for the explicit analysis, which captures the rapid wave propagation following the rupture. The explicit analysis is particularly well-suited for these short-duration dynamic events and ensures that both static and dynamic behaviors are accurately modeled.
3. **Model Validation:** Validation of the numerical model is a critical part of this thesis. The process involves several steps:
 - Mesh quality validation according to established literature thresholds.
 - Mesh sensitivity analysis, where different mesh sizes are tested to confirm consistent results in both time and frequency domains.
 - Energy balance validation, ensuring that the model behaves according to physical principles.
 - Semi-qualitative comparison of simulation results with real-world experimental data from beam tests, reinforcing the accuracy of the model.

4. **Data Collection and Post-Processing:** The primary data collected from the simulations is acceleration response, which is analyzed using both Fourier Transform and Short-Time Fourier Transform (STFT) techniques. This enables the evaluation of structural behavior in both time and frequency domains.

Chapter 3

Theoretical Framework

3.1 Finite Element Method

The Finite Element Method (FEM) serves as a powerful tool, enabling the approximation of solutions to real-world problems that are governed by physical laws. These problems are often expressed through algebraic, differential, or integral equations [14]. FEM addresses several limitations of traditional variational methods by facilitating the derivation of approximation functions within subregions of the domain. Three main characteristics underline its advantages:

1. **Geometric Complexity Management:** FEM approximates a geometrically complex domain as a collection of simpler, manageable subdomains known as finite elements. This subdivision simplifies the overall problem into smaller, more manageable parts.
2. **Approximation Functions:** Over each subdomain, the approximation functions are derived based on the premise that any continuous function can be represented as a linear combination of algebraic polynomials. This approach allows for a flexible and accurate representation of complex functions across the domain.
3. **Interpolation and Governing Equations:** The relationships among undetermined nodal values are established by ensuring that the governing equations are satisfied for each element. The approximation functions, derived from interpolation theory, are therefore named interpolation functions. This methodical approach ensures that the FEM model sticks closely to the physical behaviors described by the governing equations.

3.1.1 Theoretical Notes on FEM

In Finite Element Method, the general aim is to find an approximate solution u to a differential equation of the form [14]:

$$u \approx \sum_{j=1}^n u_j \psi_j \quad (3.1)$$

Where u represents the solution for a particular differential equation, u_j are the values of u at the element nodes, and ψ_j are the interpolation functions. In the finite element method, the given domain is divided into subdomains, for which an approximate solution is developed for each one of the defined subdomains [14]. Substitution of equation 3.1 into the governing differential equation does not always result in the required number of linearly independent algebraic equations for the unknown coefficients u_j . In order to ensure the same amount of equations as unknowns is to use weighted integrals of the error in the equation to be zero [14].

Variational method by means of the use of integral statements provides and help for obtaining as many algebraic equations as there are unknown coefficients in the approximation. Variational methods differs from each other in the choice of the weight function w and the integral statement, which decrease the choice of the approximation function [14]. Finite Element Method follows variational method in the search for an approximate solution for a given subdomain (i.e. element) of the domain.

Finite element Method applied in the linear analysis of solids, has for standard formulation the displacement method, other methods such as mixed formulations, where not only the displacements are employed as unknown variables, are preferred for other specific types of problems [15]. The principle of virtual work is the basic relationship used for the finite element formulation.

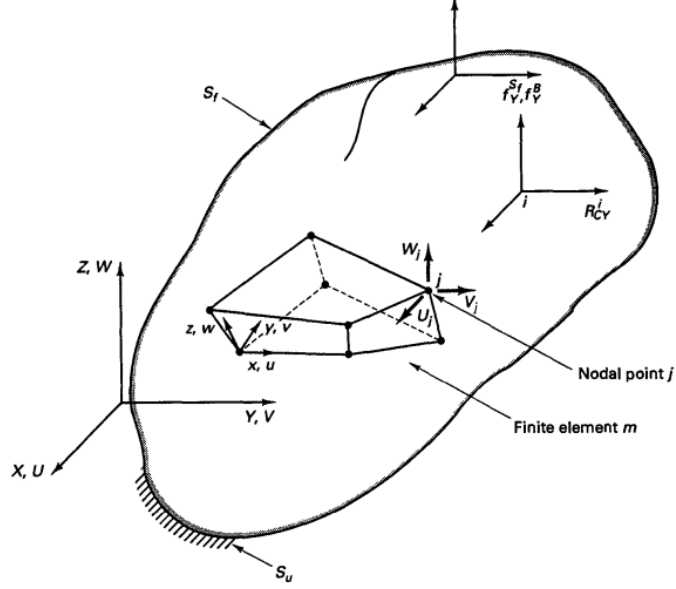


Figure 3.1: General 3-dimensional body [15]

Considering the equilibrium of a generic three-dimensional body, located in the fixed coordinate system X, Y, Z , as shown in figure 3.1. The body is supported on the area S_u with prescribed displacement U^{S_u} and subjected to surface tractions f^{S_f} on the surface area S_f . In addition, the body is subjected to body forces f^B , and concentrated loads R_C^i (where i is the point of load application).

Given the geometry of the body, the applied loads, the support condition on S_u , the material stress-strain law, and the initial stresses in the body it is computed the displacements U of the body and the corresponding strains and stresses, establishing the governing differential equations of equilibrium, which then would have to be solved subjected to the boundary conditions [15].

The foundation of the displacement-based finite element solution lies in the principle of virtual work. This principle states that the equilibrium of the body referenced in figure 3.1 requires that for any small and compatible virtual displacements imposed on the body in its state of equilibrium, the total internal virtual work generated by the imposed displacement must equal the total external virtual work.

$$\int_V \bar{D}^T T dV = \int_V \bar{U}^T f^B dV + \int_{S_f} \bar{U}^{S_f T} f^{S_f} dS + \sum_i \bar{U}^{i T} R_C^i \quad (3.2)$$

Where \bar{U} are the virtual displacements and \bar{D} are the corresponding virtual strains. When the principle of virtual work is satisfied, equilibrium, compatibility, and stress-strain law hold.

From equation 3.1 considering each subdomain (i.e. element), and a generalize matrix form, element strains are:

$$D = B\hat{U} \quad (3.3)$$

Where B is the strain-displacement matrix, \hat{U} is a column vector containing the nodal values u_j .

Stresses are:

$$T = CD + T^I \quad (3.4)$$

Where C is the elasticity matrix.

From the assumption of the displacement shown in equation 3.1 it is possible to derive the equilibrium equations corresponding to the nodal point displacements of the assemblage of finite elements, for a single element (m).

$$\sum_m \int_V \bar{D}^T T dV = \sum_m \int_V \bar{u}^T f^B dV + \sum_m \int_{S_1, \dots, S_q} \bar{u}^{S^T} f^S dS + \sum_i \bar{u}^{i^T} R_C^i \quad (3.5)$$

Where S_1, \dots, S_q are the element surfaces that are part of the body surface S .

Finally by means of equation 3.1 and equation 3.3, equilibrium equation is obtained of the form:

$$KU = R \quad (3.6)$$

The load vector R involves the effect of element body forces, initial stresses, and concentrated loads. The general equilibrium equation, considering inertial forces (by means of D'Alembert principle) and damping forces is of the form:

$$M\ddot{U} + C\dot{U} + KU = R \quad (3.7)$$

Where

$$C = \sum_m \int_V k H^T H dV = \sum_m C^{(m)} \quad (3.8)$$

$$M = \sum_m \int_V \rho H^T H dV = \sum_m M^{(m)} \quad (3.9)$$

$$K = \sum_m \int_V B^T C B dV = \sum_m K^{(m)} \quad (3.10)$$

Where two properties must be met, since in general, in finite element analysis, differential equilibrium is not exactly satisfied at all points of the domain, but it must be met [15]:

- Nodal point equilibrium.
- Element equilibrium.

The solution to a problem by FEM, starts from the discretization of the domain, into finite elements whose solution type is known. FEM computes field variables at node level for which the interpolation functions (called shape functions) are needed to know the variables on the domain of each element.

3.1.2 FEM Analysis phases

Once the fundamental principles of the Finite Element Method (FEM) have been revised, the application via a computational program, as demonstrated in this thesis with LS-DYNA, follows the next framework:

1. Pre-processing Phase:

In this initial phase, the structural model is developed, incorporating all necessary parameters for the analysis. This includes the creation of the mesh and the specification of boundary conditions, material properties, type of elements, etc. The goal is to prepare a detailed and accurate representation of the physical system to be analyzed, ensuring that all relevant physical and geometric properties are correctly modeled.

2. Processing Phase:

During this phase, the problem is solved numerically. Based on the type of analysis specified, the solver, for this case, LS-DYNA, processes the input data, which includes mesh configurations, material properties, and boundary condi-

tions. The solver computes the solution to the governing equations of the model, effectively simulating the behavior of the structure under loading condition established.

3. Post-processing Phase:

This final phase involves analyzing and interpreting the results obtained from the solver. The outputs from the numerical model are evaluated to determine their relevance and accuracy in representing the real-world scenario. This may include visualizing stress distributions, deformations, wave propagation, or other critical parameters, and validating these results to ensure that the model provides an accurate and useful approximation of reality.

3.2 Time Integration Algorithms

Time integration algorithms are key tools in numerical analysis, helping solve and converge into solutions of nonlinear dynamic response. It is possible to distinguish two main types of algorithms, Implicit time integration methods, and Explicit time integration methods.

Transient analysis of nonlinear problems requires a stable and accurate solution of the equation 3.7, a possibility for the solution of the equilibrium equation is by means of direct time integration in which the equilibrium relations are satisfied at discrete time points Δt . The solution is stepped forward in time by assuming time variation of displacements, velocities, and accelerations within the specified time interval Δt [16].

3.2.1 Explicit Analysis

Typically, explicit analysis is employed for short-period dynamic simulations, such as impact and crash analyses, due to its computational efficiency in these contexts. However, this method is generally considered too resource-intensive for long-duration or static analyses. Unlike implicit methods, explicit analysis does not require iterative convergence to reach a solution, as nodal accelerations are directly calculated.

Assuming that the solution have being determined at the discrete time intervals Δt up to to time t , explicit integration techniques applies equation 3.7 at the time for which the displacements are known to obtain the solution at time $t + \Delta t$ [16].

Softwares such us LS-DYNA, which is utilized for the current study, solve via explicit algorithm considering internal and external forces summed at each nodal

point. Nodal acceleration is then computed by dividing by the nodal mass. The solution follows by integrating this acceleration over time [17]. The solution process initiates with the computation of nodal acceleration at time t , followed by calculation of velocities at time $t+1/2$, and displacements at time $t+1$. From these displacements, strains are derived, and subsequently stresses [18]. This cycle is realized for each time step.

LS-DYNA uses the explicit central difference scheme to integrate the equations of motion, in which is assumed that

$$\ddot{U}^t = \frac{1}{\Delta t^2}(U^{t-\Delta t} - 2U^t + U^{t+\Delta t}) \quad (3.11)$$

$$\dot{U}^t = \frac{1}{2\Delta t}(-U^{t-\Delta t} + U^{t+\Delta t}) \quad (3.12)$$

The displacement solution for time $t + \Delta t$ is obtained by considering equation 3.7 at time t .

$$M\ddot{U}^t + C\dot{U}^t + KU^t = R^t \quad (3.13)$$

Substituting the relations for \ddot{U}^t and \dot{U}^t from 3.11 and 3.12 into equation 3.13 it is obtained

$$\left(\frac{1}{\Delta t^2}M + \frac{1}{2\Delta t}C\right)U^{t+\Delta t} = R^t - \left(K - \frac{2}{\Delta t^2}M\right)U^t - \left(\frac{1}{\Delta t^2}M - \frac{1}{2\Delta t}C\right)U^{t-\Delta t} \quad (3.14)$$

From which we can solve for $U^{t+\Delta t}$, which is computed considering the conditions at time t i.e. equation 3.13, reason why the scheme is called *explicit method*. A special consideration to the Central Difference scheme is that it requires that the selected time step Δt be smaller than the critical value Δt_{cr} which is function of the smallest period of the finite element model. For this consideration, Central Difference is said to be *conditionally stable* [15].

$$\Delta t \leq \Delta t_{cr} = \frac{T_n}{\pi} \quad (3.15)$$

3.2.2 Implicit Analysis

Contrary to explicit integration techniques, implicit ones use equation 3.7 at a time for which the solution is not known, to obtain the response at time $t + \Delta t$ [16]. Solvers using implicit analysis require a numerical solver to invert the stiffness matrix over the course of a time step, always a matrix factorization has to be performed for the solution of the equation within an iteration, even when the mass matrix is a diagonal matrix [19].

LS-DYNA employs a similar solution algorithm for both nonlinear implicit static and dynamic analyses. The primary distinction lies in the inclusion of dynamic terms in the calculation of residual forces, which are functions of displacement U , velocity \dot{U} , and acceleration \ddot{U} . This approach utilized the Newmark time integration scheme, the dependence of the last two is set by

$$\dot{U}^{t+\Delta t} = \dot{U}^t + [(1 - \delta)\ddot{U}^t + \delta\ddot{U}^{t+\Delta t}] \Delta t \quad (3.16)$$

$$U^{t+\Delta t} = U^t + \dot{U}^t \Delta t + [(\frac{1}{2} - \alpha)\ddot{U}^t + \alpha\ddot{U}^{t+\Delta t}] \Delta t^2 \quad (3.17)$$

Where Δt is the time step size, α and δ are the parameters of the integration method, which determine the integration accuracy and stability. In addition, the equilibrium equation 3.7 is considered at time $t + \Delta t$, accounting for displacements, velocities and accelerations at time $t + \Delta t$ [15].

$$M\ddot{U}^{t+\Delta t} + C\dot{U}^{t+\Delta t} + KU^{t+\Delta t} = R^{t+\Delta t} \quad (3.18)$$

Solving equation 3.17 for $\ddot{U}^{t+\Delta t}$ in terms of $U^{t+\Delta t}$, after substitution in equation 3.16 it is obtained $\ddot{U}^{t+\Delta t}$ and $\dot{U}^{t+\Delta t}$ in terms of $U^{t+\Delta t}$ which can be solved by equation 3.18 [15].

3.3 Wave Propagation in Materials

Given that the focus of this study is on the post-breakage behavior, particularly how waves propagate through concrete, a thorough review of the theoretical framework is essential. Analyzing wave propagation provides insights into the energy distribution and stress concentrations within a structure immediately after failure.

3.3.1 Governing Equations

Wave propagation in solids is primarily described by the equations of motion derived from continuum mechanics and the principles of elasticity. The basic governing equation for an elastic wave in a solid medium is called equation of motion for a continuum, a set of three equations derived from the equilibrium on a cubic element in a continuum undergoing internal motions and the application of Newton's law to the medium [20].

$$\rho \frac{\partial^2 u}{\partial t^2} = \nabla \cdot \sigma + f \quad (3.19)$$

Where ρ is the material density, u is the displacement vector field, $\nabla \cdot \sigma$ is the divergence of the stress tensor (internal stresses), and f is the body forces per unit volume (external forces).

The need for a relationship between stress and displacement is essential, and it is provided by the constitutive laws, that relate stress to strain, hence stress to displacement gradients, which for isotropic, homogeneous materials Hooke's law is followed (the most general form of constitutive law for linear elasticity) [20].

$$\sigma_{ij} = C_{ijkl} \epsilon_{kl} \quad (3.20)$$

The constant C_{ijkl} are known as *elastic moduli* and characterize the material properties of the medium. In its general form C_{ijkl} is a third-order tensor which relates the nine elements of the strain and stress tensors resulting in nine equations, which by symmetry can be reduced to six. Recalling the one-dimensional Hooke's Law.

$$\sigma = E \epsilon \quad (3.21)$$

This allows the formulation of wave equations specifically Longitudinal waves (P-waves), transverse (S-waves), and surface waves (Rayleigh and Love waves). The velocity of these waves depends upon the material's elastic modulus, Poisson's ratio, and density.

3.3.2 Types of Waves in Solids

On one hand, longitudinal waves, or primary waves (P-waves), involve particle motion parallel to the direction of the wave propagation, and represent the fastest

type of elastic waves. The velocity of P-waves in a solid is given by:

$$v_p = \sqrt{\frac{E(1-\nu)}{\rho(1+\nu)(1-2\nu)}} \quad (3.22)$$

On the other hand, transverse waves, or secondary waves (S-waves), involve particle motion perpendicular to the direction of wave propagation. S-waves are slower than P-waves and their velocity is given by:

$$v_s = \sqrt{\frac{G}{\rho}} = \sqrt{\frac{E}{2\rho(1+\nu)}} \quad (3.23)$$

Rayleigh waves combine longitudinal and vertical shear motion, while Love waves involve horizontal shear motion. They travel along the surface of a solid material and decay exponentially with depth.

Chapter 4

On LS-DYNA & Model Development Basis

4.1 Model Development

In this thesis, LS-DYNA, now a part of ANSYS, serves as the primary software for developing the simulation and finite element model. The integration of LS-DYNA with other ANSYS software tools enhances the capabilities of our modeling processes. This collaboration allows for the utilization of specialized programs such as SpaceClaim, a computer-aided design (CAD) tool with better mesh generation capabilities. The subsequent sections will detail the software parameters and how SpaceClaim and other tools complement LS-DYNA to optimize model development.

4.2 Detailed Software Considerations

4.2.1 Contact Types

In finite element analysis, accurately defining how different parts of a model interact is crucial for obtaining reliable simulations and actual representation of reality. This section explores two primary methods used to define contact in finite element models, each specified to different types of interactions and modeling requirements. These methods are the kinematic constraint method, and the penalty method, each offering distinct advantages and suitable for specific applications within LS-DYNA.

Kinematic Constraint Method

In the kinematic constraint method, constraints are imposed on the global equations by a transformation of the nodal displacement components of the slaves nodes along the contact interface which eliminates the normal degree of freedom of the nodes [21]. This contact type is primarily employed for tying interface together, where the slaves nodes are constrained to follow the movements of the master side nodes. This method is particularly useful for situations where no relative motion between the connected parts is desired.

Penalty Method

The penalty method provides a way to simulate contact by introducing a stiffness-based penalty factor between the interacting surfaces by placing normal interface springs between all penetrating nodes and the contact surface, then the spring stiffness matrix must be assembled into the global stiffness matrix [21]. This method does not strictly enforce a no-penetration condition as the kinematic constraint does; instead, it allows a certain degree of interpenetration, which is resisted by a force proportional to the penetration depth (i.e. by the spring). The penalty method is widely used for simulating contacts where small penetrations can be tolerated, such as in the case of rubber seals or gaskets in engineering applications.

In LS-DYNA, the *tiebreak* contact type is categorized within the penalty-based contacts. This approach allows for the simulation of contact behaviors that include the potential for separation and failure at the interface, providing a realistic modeling of physical contacts that can degrade under stress. The *tiebreak* contact type enables the specification of contact stress, σ both normal and tangential, as a function of the separation distance at an interface, as set in the predefined interface contact law. The law is characterized by the energy release rate (energy per unit required to release the contact) and the maximum interface stress (peak contact stress before the softening phase). The contact law utilized in the present study is described as follows.

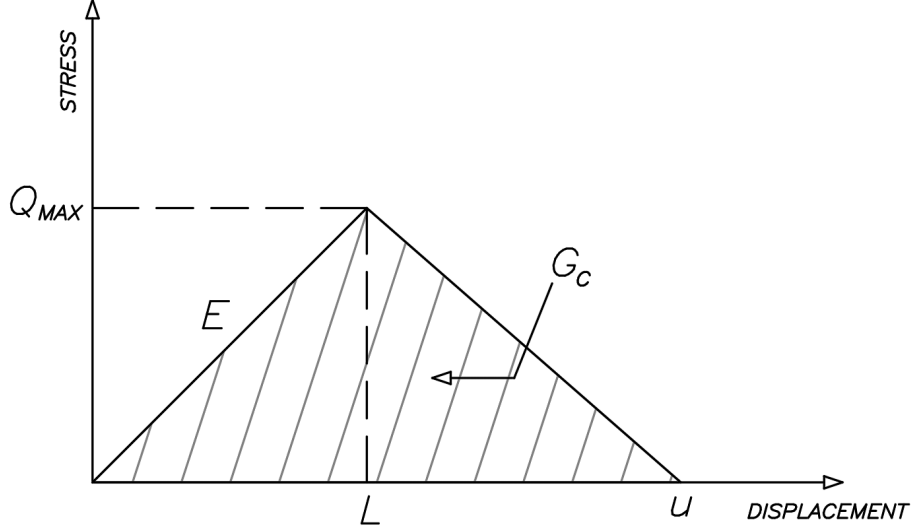


Figure 4.1: Bilinear cohesive mixed-mode law

Where Q_{max} represents either the normal failure stress or the shear failure stress, E is the normal or tangential stiffness, and G_c is either the normal or shear energy release rate, the relationships are shown above.

$$L = \frac{Q_{max}}{E} \quad (4.1)$$

$$u = \frac{2G_c}{EL} \quad (4.2)$$

To ensure the maximum is not past the failure point it is set $u/L > 1$

$$\frac{u}{L} = \frac{2G_c}{ELxL} = \frac{2G_c}{E\left(\frac{Q_{max}}{E}\right)^2} > 1 \quad (4.3)$$

4.2.2 Element Formulation

In finite element analysis (FEA), choosing the right type of element is important, since it affects how accurate and efficient the simulation will be. Solid elements are often used to build most models that comes with different topologies, each designed for different kinds of analyses. The typical solid elements used are tetrahedral and hexahedral elements, in which many categories are to be selected from, depending on the type of analysis and mesh desired.

In this study, tetrahedral elements were chosen due to their flexibility in mesh sizing compared to hexahedral elements. This flexibility is especially beneficial for

models where different components demand varying levels of detail. For instance, the steel tendons in the prestressed concrete beams require a finer mesh because of their reduced size. Contrary, the concrete parts can be modeled with a coarser mesh. Tetrahedral elements are ideally suited for this task, as they easily adjust to diverse meshing requirements, thus enabling precise and efficient modeling of distinct components within the same framework.

For the development of the finite element model using LS-DYNA, element 13 was selected, which corresponds to a nodal pressure tetrahedron.

Node Pressure Tetrahedral Element

Standard formulations for tetrahedral elements often exhibit volumetric locking phenomena and stiff behavior, due to the fact that the volume of the elements must remain constant [22], which can adversely affect the accuracy of simulations, especially under compressive load conditions. To address this issue, the advanced tetrahedral element, which incorporates nodal pressure variables, offers a significant improvement. This element type effectively alleviates volumetric locking, ensuring more reliable simulations, with a better performance overall than the standard 4-node tetrahedral element.

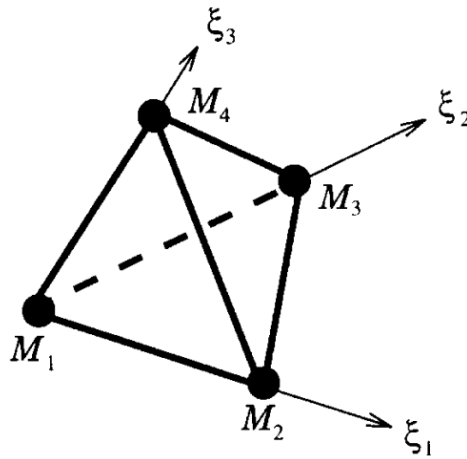


Figure 4.2: Four node tetrahedron [22]

The four-node tetrahedron element shown in figure 4.2 is a standard isoparametric tetrahedron, the formulations for the node pressure tetrahedral element are expressed below, extracted from [22]. Starting from the standard four-node tetrahedron element, the geometry is interpolated in terms of the shape functions N_a , and the isoparametric coordinates ξ_1, ξ_2 , and ξ_3 , where a represents the nodes.

$$X^{(e)} = \sum_{a=1}^n N_a(\xi_1, \xi_2, \xi_3) X_a \quad (4.4)$$

The volumetric strain energy is approximated by assuming that the volume ratio J remains constant over the volume attached to each node

$$\Pi_{vol}(x) = \sum_{a=1}^n U(J_a) V_a \quad (4.5)$$

Where J is expressed in terms of current and initial nodal volumes

$$J_a = \nu_a / V_a, \quad \nu_a = \sum_{e=1}^{m_a} \frac{1}{4} \nu^{(e)} \quad (4.6)$$

From where the corresponding volumetric internal forces are obtained by differentiation in the direction of the virtual velocities to obtain the volumetric internal virtual work (D being the differentiation operator)

$$\delta W_{vol} = D\Pi_{vol}[\delta v] = \sum_{a=1}^n p_a V_a D J_a[\delta v] \quad (4.7)$$

Where the average nodal pressure is represented as follows

$$p_a = \left. \frac{dU}{dJ} \right|_{J=\nu_a/V_a} = k \left(\frac{\nu_a - V_a}{V_a} \right) \quad (4.8)$$

The directional derivative of the average nodal volumetric strain in the direction of δv is obtained from equation 4.6 and 4.9

$$D J_a[\delta v] = J_a \operatorname{div} [\delta v] \quad (4.9)$$

$$D J_a[\delta v] = \frac{1}{V_a} D \nu_a[\delta v] = \frac{1}{V_a} \sum_{e=1}^{m_a} \frac{1}{4} \nu^{(e)} \operatorname{div} \delta v^{(e)} \quad (4.10)$$

From equation 4.10, equation 4.7 can be written as

$$\delta W_{vol} = \sum_{a=1}^n \sum_{e=1}^{m_a} \frac{1}{4} p_a \nu^{(e)} \operatorname{div} \delta v^{(e)} = \sum_{e=1}^m \bar{p}^{(e)} \nu^{(e)} \operatorname{div} \delta v^{(e)} \quad (4.11)$$

Where

$$\bar{p}^{(e)} = \frac{1}{4} \sum_{a=1}^4 p_a^{(e)} \quad (4.12)$$

Is the average element pressure and would correspond with the pressure at the centroid of the element obtained from a linear interpolation from nodal values. On the other hand, the internal equivalent forces in terms of the average element pressure is defined as

$$T_{vol,a}^{(e)} = \bar{p}^{(e)} \nu^{(e)} \nabla N_a^{(e)} \quad (4.13)$$

The employment of the described advanced element does not significantly increase computational expenses in comparison to the standard four-node tetrahedron element. Additionally, the issue of locking, is effectively mitigated for sufficiently large meshes [22].

4.2.3 Element Size

Element size plays a crucial role in finite element (FE) models as it directly impacts the accuracy and convergence of the simulation results to real solutions. A key criterion for defining the maximum element size is *wavelength resolution*; the elements must be sufficiently small to capture the specified and desired maximum frequency of interest. This ensures that the model accurately represents the dynamic behavior of the structure, particularly in scenarios involving high-frequency wave propagation. In order to obtain the step size, the following condition is imposed [23]

$$\Delta x \leq \frac{\lambda_{min}}{n} \quad (4.14)$$

Where λ_{min} is the minimum wavelength in the configuration that can be computed from the maximum frequency of interest and the velocity of the wave, n is a parameter that controls the accuracy, with typical values ranging from 10 - 20, and Δx corresponds to the element size.

Regarding element size distribution along the geometry, following the recommendations from Cook, et al [24], element size should not change abruptly, in cases where it does, the discrete mass matrix will be a poor representation of the real continuous mass matrix. This will arise in wave reflection and additional numerical noise when

waves cross boundaries between elements.

4.2.4 Damping

Since the model aims to simulate real behavior as closely as possible, introducing damping is essential to replicate the energy dissipation that occurs in actual scenarios. In LS-DYNA, two main options are relevant to our study: stiffness-weighted damping and mass-weighted damping. Stiffness-weighted damping is introduced through Rayleigh damping, which accounts for energy dissipation based on the material stiffness and mass properties. Mass-weighted damping, on the other hand, is applied globally to the nodes as a mass-weighted nodal damping, providing a damping effect proportional to the mass of the structure.

The damping matrix on Rayleigh damping can be defined as [17]

$$C = \alpha M + \beta K \quad (4.15)$$

Where C , M and K are the damping, mass and stiffness matrices, respectively and the constants α and β are the mass and stiffness proportional damping constants [17].

While for the mass proportional damping, the damping matrix is defined as [17]

$$C = 2\omega_i \xi_i \delta_{ij} \quad (4.16)$$

Where ω_i is the i -th frequency and ξ_i is its corresponding modal damping parameter.

Generally, stiffness-proportional damping is more effective at higher frequencies and is orthogonal to rigid body motion. In contrast, mass-proportional damping is more effective at lower frequencies and will damp rigid body motion [17].

4.2.5 Mesh Control

In the field of finite element analysis, the quality of the mesh is of prime importance. Effective mesh control is crucial as it directly influences the accuracy, efficiency, and reliability of a model. A well-constructed mesh accurately represents the physical characteristics of the modeled structure. To ensure the creation of a high-quality mesh, various parameters must be carefully considered and optimized. These parameters determine how well the mesh obeys to the geometry of the structure, how it

behaves under load, and how accurately it represents the physical phenomena being studied. Knupp [25] defines mesh quality as "the characteristics of a mesh that permit a particular numerical partial differential equation (PDE) simulation to be efficiently performed, with fidelity to the underlying physics, and with the accuracy required for the problem". The upcoming sections will detail these critical parameters.

Element Jacobians

The element Jacobians, which represent the determinant of the Jacobian matrix, contain critical information about the volume, shape, and orientation of the elements. These Jacobians provide insight into the volume distortion when compared to an ideally shaped reference element [26]. A negative Jacobian indicates that the element is inverted, and will not enable the analysis to continue since stability at element level involves the requirement of Jacobian positiveness and rank sufficiency [27]. The criteria established by literature regarding analysis via element Jacobians, states the following:

- They be positive in value [27], [25]
- Preferably greater than 0.2 in magnitude [28]
- The majority of element Jacobians should fall above 0.7 in magnitude [28]

Aspect Ratio

Aspect ratios (AR) are a key geometrical metric used to evaluate the shape quality of finite elements. The computation of the aspect ratio varies depending on the type of element being analyzed. In this study, for tetrahedral elements, the aspect ratio is determined by dividing the length of the longest edge by the minimum altitude of the smallest side figure 4.3. For optimal model accuracy, the following considerations are to be followed

- The most accurate solutions are achieved when the aspect ratio is close to unity [29]
- The majority of elements should have aspect ratios between 1 and 4 [30]
- Elements with the poorest aspect ratios should be positioned away from critical areas of interest to minimize their impact on the results [26]

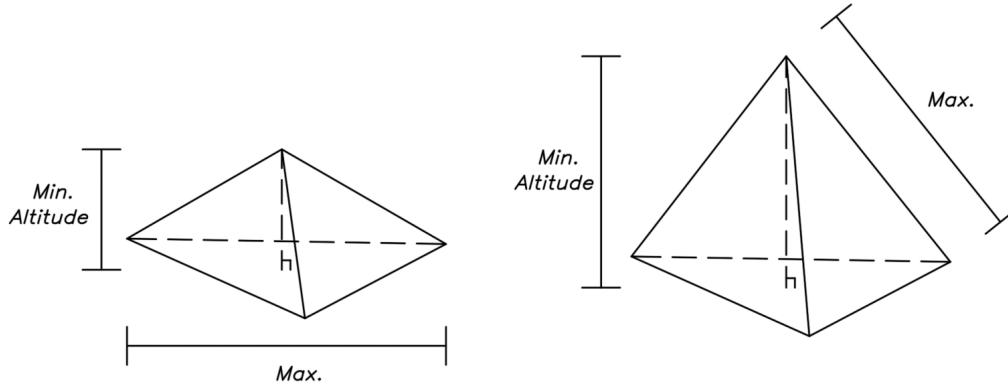


Figure 4.3: Tetrahedral Aspect Ratio Calculation

Skewness

Skewness is measured by the angle related to two lines that passes through the midpoints [31]. It is one of the primary ways to define element quality and can be checked by the comparison with an idea equilateral element [32]. For the evaluation of the parameter, the following considerations are to be followed

- Maximum value is unity
- Minimum value is zero
- All values should be below 0.95
- The majority should be below 0.5 [32]

4.2.6 Time step

Courant-Friedrichs-Lewy Condition

Defining the time step is crucial in finite element simulations as it directly impacts both the accuracy and stability of the results. Richard Courant, Kurt Friedrichs, and Hans Lewy demonstrated that for an explicit numerical scheme, stability and convergence to the correct solution depend on meeting the Courant-Friedrichs-Lewy (CFL) condition [33]. This condition specifies that the time step must be small enough relative to the spatial discretization and wave speeds within the model to ensure that information propagates correctly through the computational domain, 4.15.

$$\Delta t \leq C_{CFL} \frac{\Delta x}{v} \quad (4.17)$$

Where v is the magnitude of the velocity of interest, Δt is the time step, Δx is the

length interval, typically the element length, and C_{CFL} is the Courant number. In other words, the CFL condition gives an upper limit of the time step, referenced to the wave propagation over a defined FE length. The value assumed of the Courant coefficient is typically 1, but it may be lower in order to obtain higher accuracy.

Chapter 5

Finite Element Model

5.1 Finite Element Models

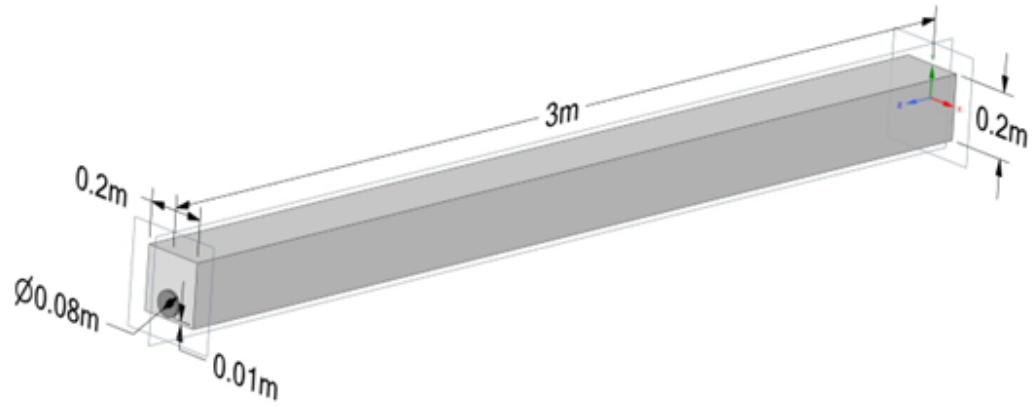
This chapter outlines the criteria and parameters selected for the creation of the different developed models, highlighting the considerations that influenced these choices. Additionally, the methodology and analysis procedures followed in the model's development are presented, offering a comprehensive view of the steps taken to ensure the accuracy and reliability of the simulations.

5.1.1 Geometry

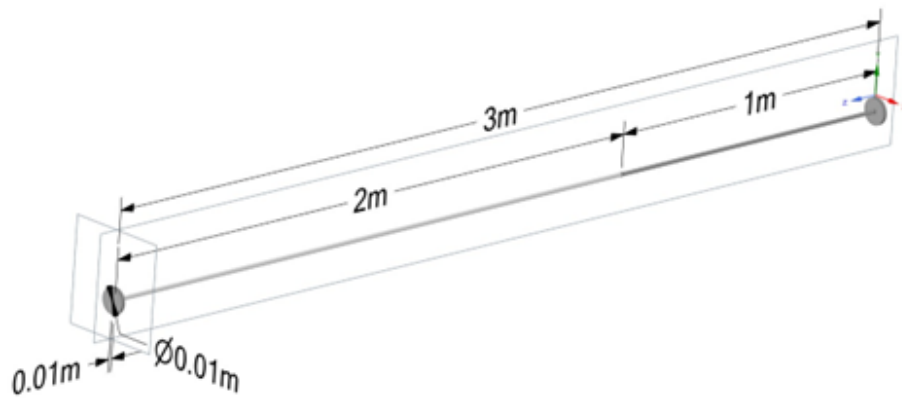
The first model's geometry is based on a typical reinforced concrete beam with a rectangular cross-section measuring 200 millimeters in width and height. A steel tendon with a diameter of 12 millimeters is included within the beam 50 millimeters from the centroid. Additionally, two steel plates at each face of the prestressed reinforced concrete beam with a diameter of 80 millimeters and a thickness of 10 millimeters were incorporated to limit slippage between concrete and steel to the second stage of the analysis (explicit analysis, see Section 3.2.1). Detailed section and geometrical properties of the beam and tendon are illustrated in Figure 5.1.

In contrast, the second model features a larger geometry, with a total length of 20 meters. This model does not include the steel plates used in the first model. Instead, the slip between steel and concrete is controlled by merging the nodes at the boundary between the steel and concrete sections during both the implicit and explicit phases of the analysis. This approach adapts to the condition of a larger model while significantly reducing the amount of unknowns introduced into the system.

The geometry of Model 1 is shown in Figure 5.1, where the geometrical properties of both the steel are displayed. The geometry of Model 2 is not illustrated due to its substantial similarity to the first model.



(a)



(b)

Figure 5.1: Geometrical properties of the prestressed RC beam

As shown in Figure 5.1b, the cut is introduced at $1/3$ of the length from the left end, geometrically, at this point, a discontinuity in terms of parts is introduced. In other words, the steel tendon is divided in two different parts connected by a contact as defined in Subsection 5.1.4.

5.1.2 Mesh Generation

The mesh for first the model's geometry presented in the previous subsection 5.1.1, was generated using ANSYS CAD system SpaceClaim, selected for its advanced modeling capabilities. As established in 4.2.5, tetrahedral elements were employed across all model components due to their superior adaptability to complex geometries. Based on the criteria established in the Element Size subsection (see 4.2.3), and considering a maximum frequency of interest of 20,000 Hz with an accuracy factor of 10, Equation 4.14 indicates that the maximum allowable element size to capture that frequency should be no more than 25 millimeters, the selected size was 22 millimeters.

Given the steel tendon's diameter of 12 millimeters, applying a 25-millimeter element size was unrealistic. To address this, a constant element size of 6 millimeters was used for the steel tendon (see 5.2c) to ensure accurate representation. Consequently, the concrete mesh was designed to be consistent, with element sizes gradually increasing from 6 millimeters at the contact elements with the steel tendon to 22 millimeters at the outer face of the concrete (see 5.2a, 5.2b). This way the accuracy needed for the interaction between the different material parts is maintained while optimizing the overall mesh for computational efficiency.

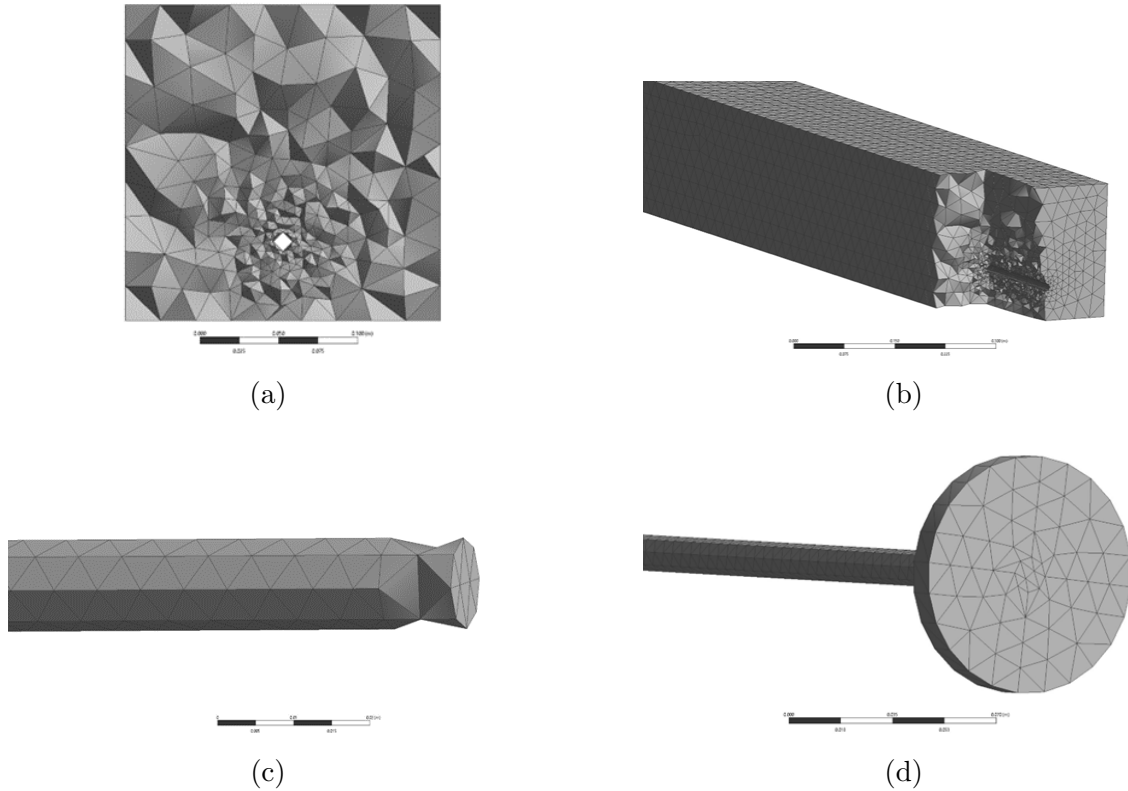


Figure 5.2: Meshed geometry - Model 1

Additionally, the steel plates, which serve as supporting elements, were primarily intended to control slip behavior during the implicit analysis rather than to contribute significantly during the explicit run. Therefore, a constant mesh size of 6 millimeters was chosen for the plates, using tetrahedral elements to maintain consistency across the model (see 5.2d). This size was selected to balance the need for mesh uniformity with the plate’s role in the simulation.

In the second model, due to its larger geometrical size, it was not possible to create a mesh with the same level of refinement as in the first model, figures 5.3b and 5.3b show the meshed geometry. The total number of elements and nodes in a mesh with similar characteristics would not allow a model of that size to run efficiently. Therefore, a maximum concrete element size of 35 millimeters was used, with the steel tendon elements set at 8 millimeters. Also, the use of steel plates was omitted, instead, nodes at the section boundary between concrete and steel were merged, reducing the amount of contacts in the model, thus the complexity of it.

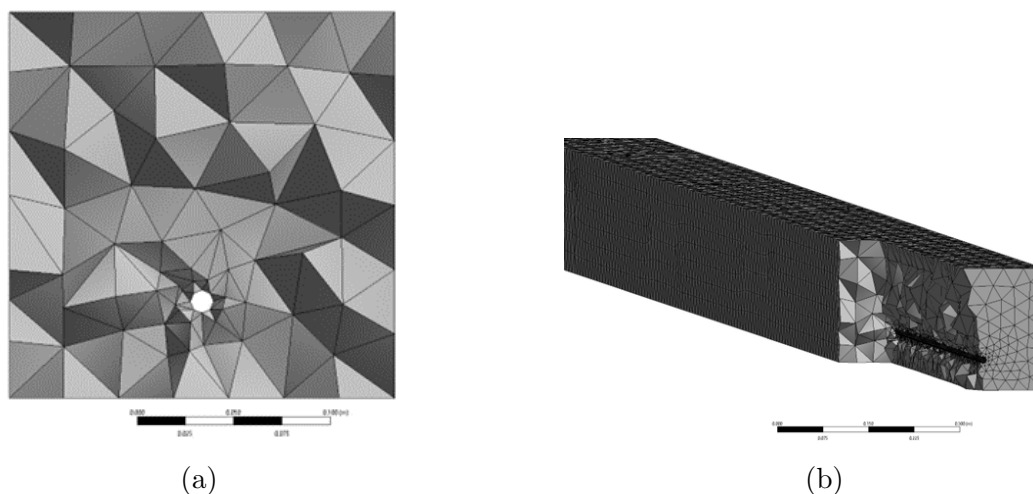


Figure 5.3: Meshed geometry - Model 2

5.1.3 Material Properties

The material type selected for the models, both for concrete and steel parts, is an elastic material, specifically *MAT_001* in LS-DYNA (refer to Appendix A for the exact definition of the command). To accurately define this material, three key properties were specified: mass density, Young’s modulus, and Poisson’s ratio. These properties are essential for characterizing the elastic behavior of the material in the model. The specific values used for these properties are detailed in Table 5.1, and 5.2 below.

Table 5.1: Concrete material characterization

Parameter	Value
Mass Density [ρ]	2400kg/m ³
Young's Modulus [E]	19.4GPa
Poisson's ratio [ν]	0.1414

Table 5.2: Steel material characterization

Parameter	Value
Mass Density [ρ]	7750kg/m ³
Young's Modulus [E]	200GPa
Poisson's ratio [ν]	0.3

5.1.4 Contact Definition

As outlined in Subsection 4.2.1, two primary contact types were defined within the models, defined to the specific material connectivity and desired behaviors. The first type is the *kinematic constraint* contact, which is commonly used for tying entities in contact. In this model, the specific contact type employed was (refer to Appendix A for the exact definition of the command):

`CONTACT_TIED_SURFACE_TO_SURFACE_CONSTRAINED_OFFSET`

The second type is the *penalty-based* contact, which allows the inclusion of a failure criterion within the contact definition (see 4.2.1, *Penalty-Based Method*). The specific contact type utilized for this purpose was (refer to Appendix A for the exact definition of the command):

`CONTACT_AUTOMATIC_SURFACE_TO_SURFACE_TIEBREAK`

On one hand, the *kinematic constraint* contact was applied between the two defined steel tendons. To simulate tendon breakage, this contact definition was designed to *die* by its control parameter *Death Time* at a given time of the simulation, so the modeling of the steel tendon was realized as two separate bodies connected by this contact definition. On the other hand, the *penalty-based* contact was implemented to simulate slippage behavior at the concrete-steel interface. This approach included a failure criterion based on the parameters specified in Table 5.3, allowing for a more realistic representation of the interface behavior between the two defined materials.

With the defined parameters stated in table 5.3, the bilinear cohesive law for the contact for both failure modes is the one shown in Figure 5.4.

Table 5.3: Tiebreak contact characterization

Parameter	Value
Normal failure stress [$NFLS^*$]	2 MPa
Shear failure stress [$SFLS^*$]	2 MPa
Normal energy release rate [$ERATEN^*$]	$1000 J/m^2$
Shear energy release rate [$ERATES^*$]	$1000 J/m^2$
Normal Stiffness [CN^*]	$2000 MPa/m$
Shear Stiffness [CT^*]	$2000 MPa/m$

* Parameter as defined in LS-DYNA control cards see in [17]

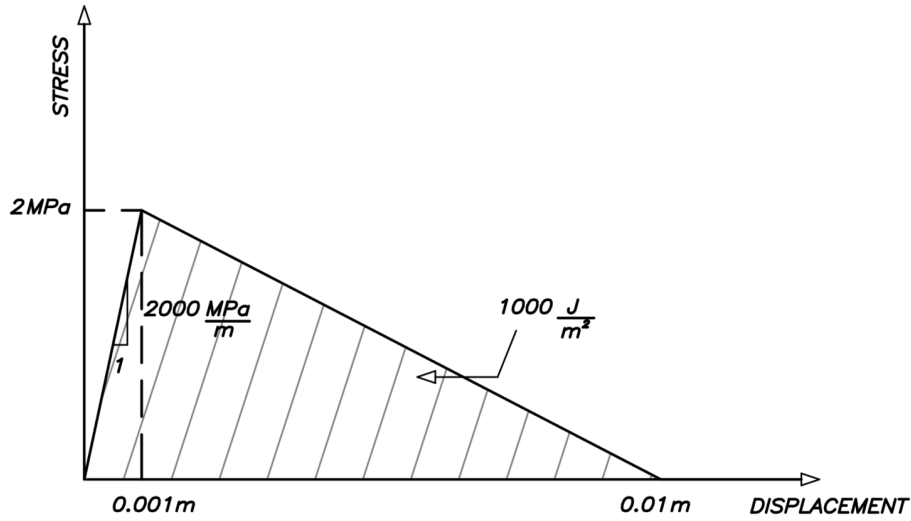


Figure 5.4: Bilinear cohesive law

The contact definition plays a critical role in the simulation by also determining the exact moment of the steel tendon rupture during the explicit run. This is achieved through the *death time* parameter within the contact type definition. The steel tendon was modeled as two independent geometries (Steel A and Steel B) as shown in Figure 5.1b connected by a kinematic constraint contact (tied contact). The release of this contact (i.e., contact death) is specified at a predetermined time, triggering the rupture event (see Appendix A for details on the 'DT' parameter in contact definition).

5.1.5 Prestressing Load

A prestressed concrete element is defined by the prestressing load applied to its steel tendons, which is then transferred to the concrete. This prestressing load can be achieved through the methodologies discussed in Section 1.2. In the developed model, the application of the pretensioning load was implemented using the LS-DYNA command (refer to Appendix A for the exact definition of the command):

INITIAL_STRESS_SOLID_SET

This command primarily requires as input parameter the stresses σ in the different directions for a given set of finite elements. For the developed model, the relevant stress direction referred to in the reference system was σ_{zz} . Referring to the theory detailed in Section 1.2, and considering that the prestress in the steel tendon is approximately 80% of its strength, Table 5.4 shows the specific value of the prestressing load used in the model.

Table 5.4: Prestressing load definition

Parameter	Value
Prestressing load [σ_{zz}]	800 MPa

5.1.6 Damping Definition

Throughout the simulations, various values of the damping coefficients and different types of damping (stiffness and/or mass-weighted damping) were applied. The same geometry and conditions were used across different cases, with varying types and levels of damping for the first model, to enable comparison and contrast with real data. Table 5.5 summarizes the different types of damping introduced in the first model and their respective damping coefficient values ζ_K or ζ_M if is Rayleigh or mass-weighted damping, respectively. As for the second model, just one case of damping definition was utilized, equal to case 7 of the first model.

Table 5.5: Damping types and values for different models

Case	Damping type	Value (ζ_K, ζ_M)
1	None	0%
2	Rayleigh	2%
3		4%
4	Mass-weighted	2%
5		4%
6	Both	2% + 2%
7		4% + 4%

The application of them was introduced by two different commands. In one hand, the Rayleigh damping was implemented with the command (refer to Appendix A for the exact definition of the command):

DAMPING_PART_STIFFNESS

The second type, mass-weighted damping, was introduced using the command (refer to Appendix A for the exact definition of the command):

DAMPING_GLOBAL

Chapter 6

Results

6.1 Overview of the Analysis

This chapter presents the results obtained from the finite element simulations, using LS-DYNA. The simulations were conducted in two distinct phases: an initial implicit analysis (see Section 3.2.2) followed by an explicit analysis (see section 3.2.1). The implicit phase aimed to apply the prestressing load to the steel tendon, as described in Section 5.1.5. This phase, typically used for static or quasi-static conditions, ensured that equilibrium was reached between the steel tendon and the concrete, with the tendon in tension and the concrete in compression.

Due to the nature of prestressed concrete technology and the behavior to be analyzed, it was necessary to transition from an implicit to an explicit analysis. The implicit analysis, which involves longer analysis times, was used to reach an equilibrated solution. Upon achieving this state, a *dynain* file within LS-DYNA containing the equilibrated solution was generated. This file served as the starting point for the explicit analysis, which is commonly used to simulate dynamic, and short-period events, such as the work of the present study, that occur over a very short period (tenths of milliseconds). The explicit analysis allows for accurate modeling of these rapid events, which would be impractical to achieve with a static or quasi-static approach.

To ensure a seamless transition from the implicit to the explicit analysis, it was crucial to maintain consistency in the parameters between both stages. The analysis began with an undeformed geometry to which the initial prestress was applied. After the implicit analysis, a deformed equilibrated configuration was achieved, which then served as the initial state for the explicit analysis. A short verification period

was included at the beginning of the explicit analysis to confirm that the geometry was truly in equilibrium, with minimal vibrations. It was also essential to maintain consistent element formulations and contact definitions between the two phases. Any changes to these parameters could introduce perturbations, leading to incorrect data and unrealistic behavior in the simulation. After verifying equilibrium, the explicit phase proceeded by introducing a cut through the 'death' of the contact tying the two independent steel geometries, as explained in Section 5.1.4 (Contact Definition).

6.2 Type of Results and Relevance

The primary results of interest from this model are the nodal accelerations, as these are directly comparable to experimental datasets obtained from accelerometers. Acceleration was chosen as the main data type because it is a critical indicator of dynamic response, providing insights into how the structure reacts to sudden changes. Acceleration data is particularly useful for structural health monitoring, as it can help detect damage, assess the integrity of the structure, and predict potential failures. Furthermore, the experimental datasets available for comparison were collected using accelerometers, making acceleration the most relevant metric for validating the numerical model.

To capture a representative sample of the dynamic response of the beam, a finite number of key nodes were selected along the boundaries of both the concrete and steel components for both of the realized models. For the first model (shortest one) three nodes were chosen on the concrete boundary, the first one located 0.5 meters from the cut, at the middle of the beam length, then the other two were evenly spaced 0.75 meters from each other. As for the steel boundary, a node 1.25 meters from the cut was selected. This selection was made to observe how the stress waves propagate and reflect along the length of the beam, taking into account factors like wave reflections, attenuation due to damping, and other dynamic effects. Placing nodes at regular intervals allows for a clearer understanding of these wave behaviors over the entire length of the beam. Additionally, selecting at least one node near the cut location was essential to closely monitor the immediate effects of rupture phenomena.

In the second model, three nodes were also selected for the concrete boundary: the first one 1 meter from the cut, the second 2.5 meters from the cut, and the third 4 meters from the cut. In steel one node was analyzed, selected 2.5 meters from the cut. The primary motivation for developing two different models was to analyze and observe the variation in results when fewer wave reflections are present. Since the

length of the first model is significantly shorter than that of the second model, it experiences numerous wave reflections from the geometry section boundary during the analysis time, given the speed of the propagating wave. In contrast, the larger model, due to its increased size, involves very few reflections during the same analysis period.

The analysis referred to the first geometry also included multiple models with varying levels of damping introduced into the system. Damping is a crucial parameter as it affects wave propagation, energy dissipation, and overall structural response. To evaluate the impact of damping, simulations were performed with different damping ratios and different damping types, as specified in section 5.1.6 in table 5.5. These variations in damping were particularly important to compare against experimental data and understand how different damping conditions affect the overall accuracy and reliability of the simulation.

6.3 Results

The results presented below focus on three key concrete nodes, as shown in Figure 6.1 for the first Model and one node for Model 2. These results are primarily in terms of nodal accelerations, providing crucial insights into the dynamic response of the structure. In addition to nodal data, global model data will also be included to compute the velocity of the primary waves propagating through the steel tendon, which serves as an additional means to verify the accuracy of the model. Also, data related to slippage between concrete and steel after the steel tendon rupture is presented. Subsequent chapters will go deeper into model validation, addressing any discrepancies between the simulated and experimental results.

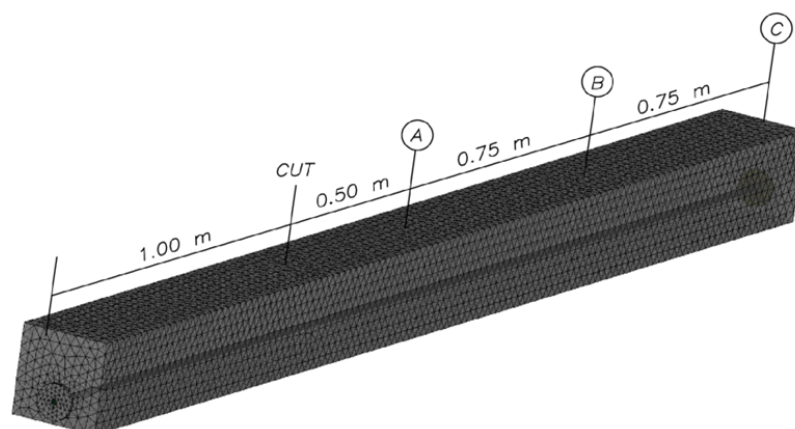


Figure 6.1: Points for data recollection - Model 1

6.3.1 Nodal Accelerations - Concrete Boundary

This section presents the results of the nodal acceleration data in the concrete boundary nodes from the finite element simulations. The results are presented in three formats to facilitate a comprehensive understanding of the data: the time-domain representation of the nodal acceleration signals, their corresponding frequency-domain representation obtained through the Fourier transform and the short time fourier transform representation to evaluate the evolution of frequency over time. Due to the extensive data collection, only a selected portion of the results is presented below as representative examples. For a complete set of graphs and data extracted from all the models, please refer to Appendix B.

Model 1

Images from 6.2 to 6.8 correspond to the results obtained from Model 1 from the same concrete node, positioned 0.5 meters from the cut, for varying values of damping.

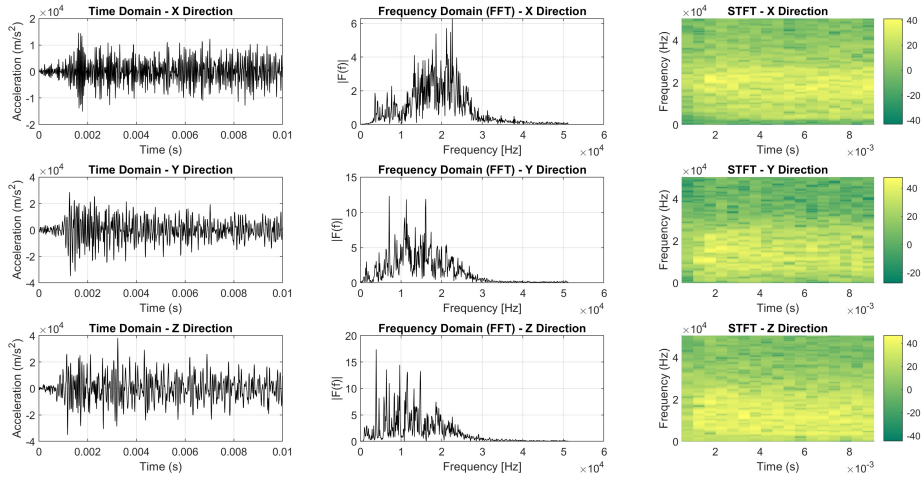


Figure 6.2: Acceleration of concrete node A, $\zeta = 0\%$ - Model 1

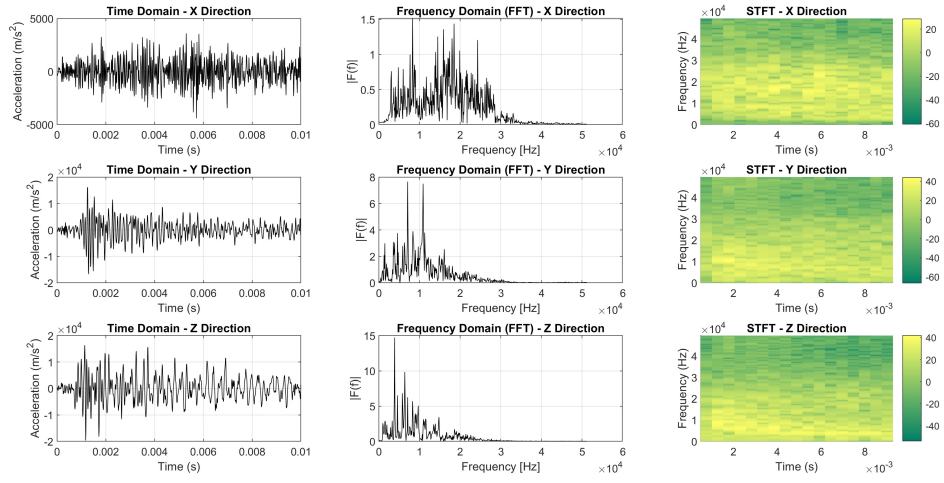


Figure 6.3: Acceleration of concrete node A, $\zeta_K = 2\%$ - Model 1

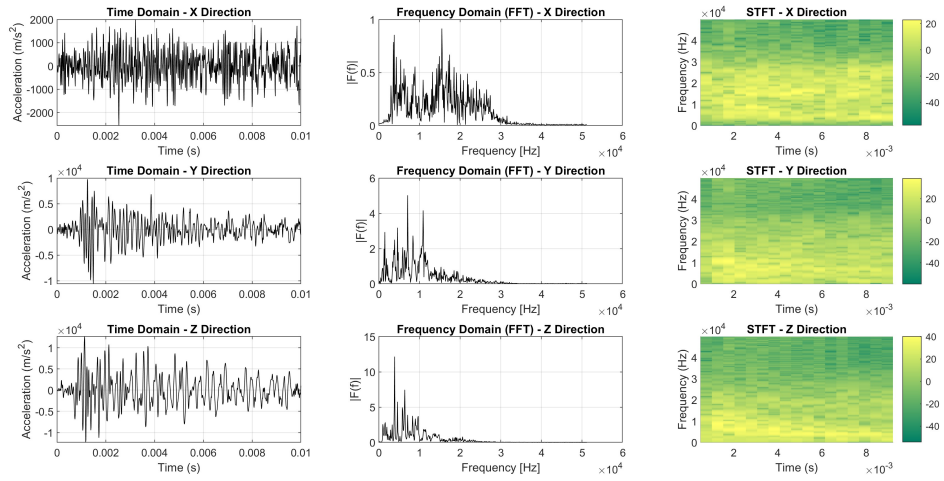


Figure 6.4: Acceleration of concrete node A, $\zeta_K = 4\%$ - Model 1

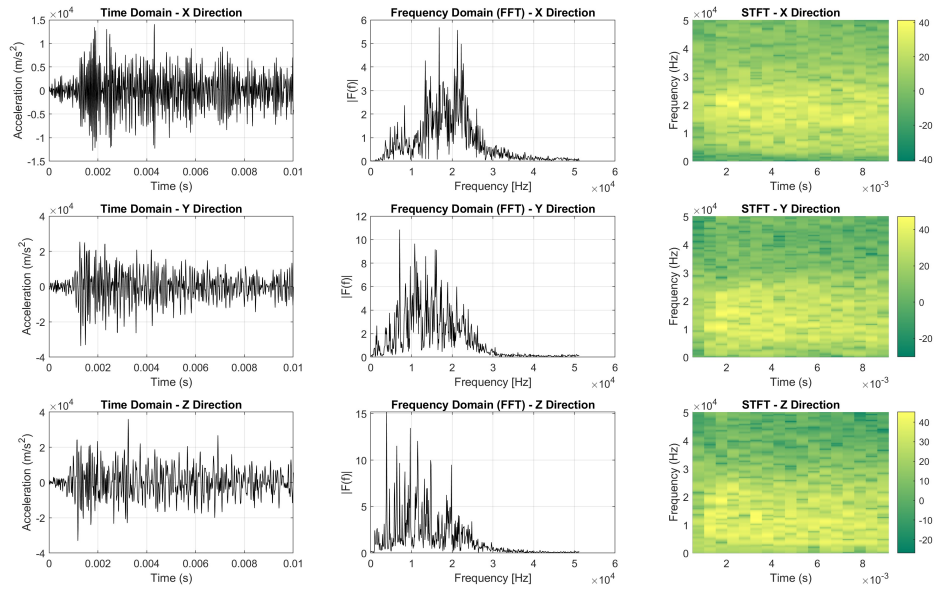


Figure 6.5: Acceleration of concrete node A, $\zeta_M = 2\%$ - Model 1

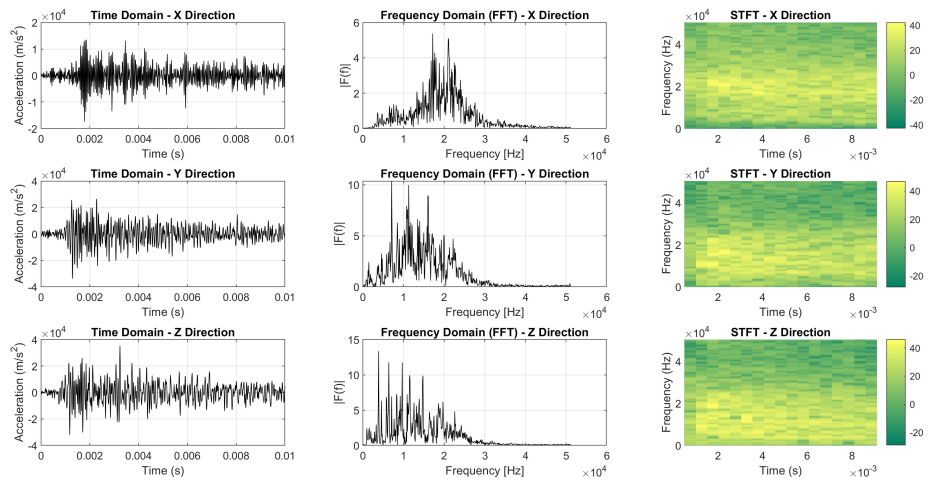


Figure 6.6: Acceleration of concrete node A, $\zeta_M = 4\%$ - Model 1

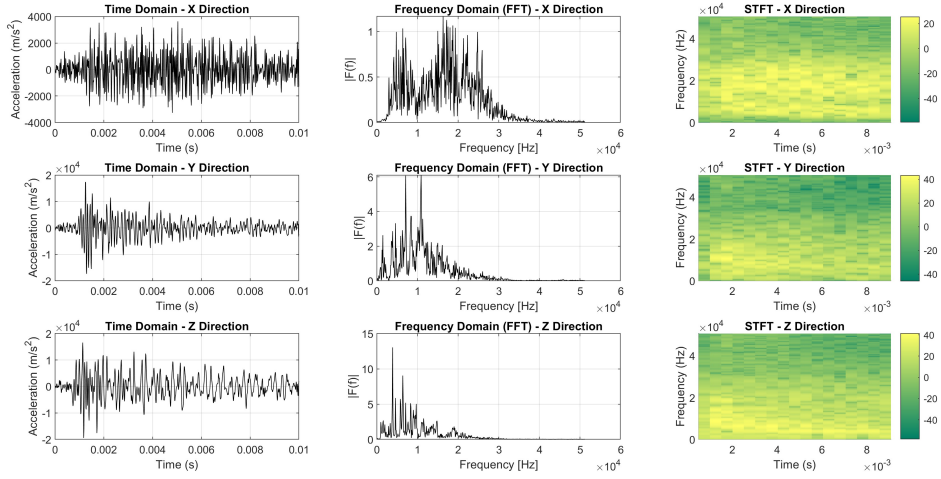


Figure 6.7: Acceleration of concrete node A, $\zeta_M = 2\%$, $\zeta_K = 2\%$ - Model 1

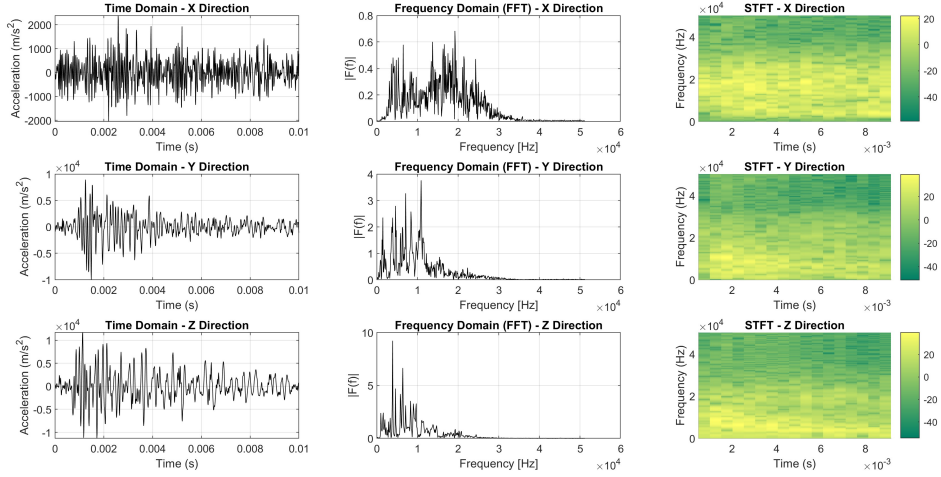


Figure 6.8: Acceleration of concrete node A, $\zeta_M = 4\%$, $\zeta_K = 4\%$ - Model 1

From the presented results, a clear trend is evident, with two main aspects depending on the damping type definition. First, in the undamped result, it is apparent that very little attenuation is present. As stiffness-proportional damping increases, higher frequencies tend to be filtered, and some vibration attenuation is observed. In contrast, as mass-proportional damping increases, lower frequencies are filtered, resulting in a higher degree of attenuation. This is consistent with the fact that the dominant frequencies for the system's vibration tend to be lower ones, meaning this type of damping has a more significant effect on energy dissipation. This behavior aligns with the theoretical understanding that stiffness-proportional damping primarily affects higher frequencies, while mass-proportional damping influences the lower ones.

Model 2

Images 6.9 to 6.11 illustrate the results for the larger Model, for these results, the analysis time is equal as for Model 1, and the damping type is the same as for the last case, meaning 4% for both stiffness and mass proportional damping. As for the position of the nodes, relative to the position of the cut, node A is located 1 meter away, node B 2.5 meters, and node C 4 meters.

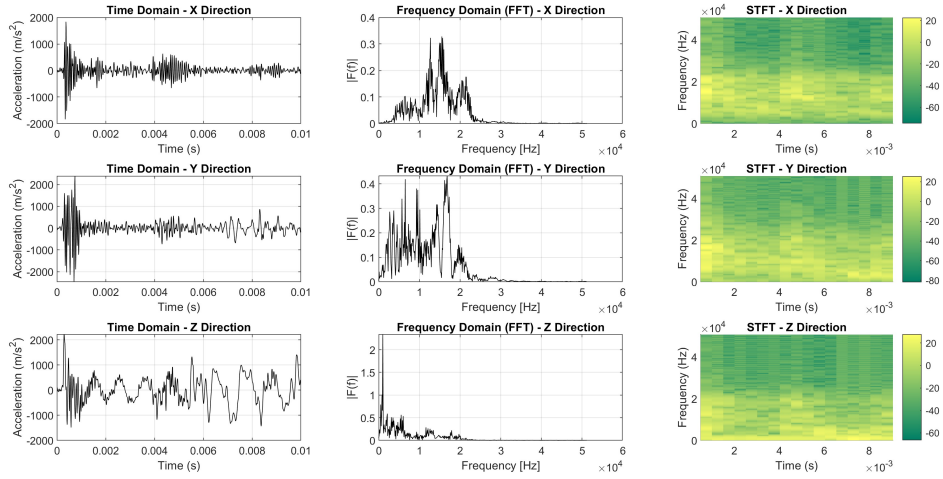


Figure 6.9: Acceleration of concrete node A, $\zeta_M = 4\%$, $\zeta_K = 4\%$ - Model 2

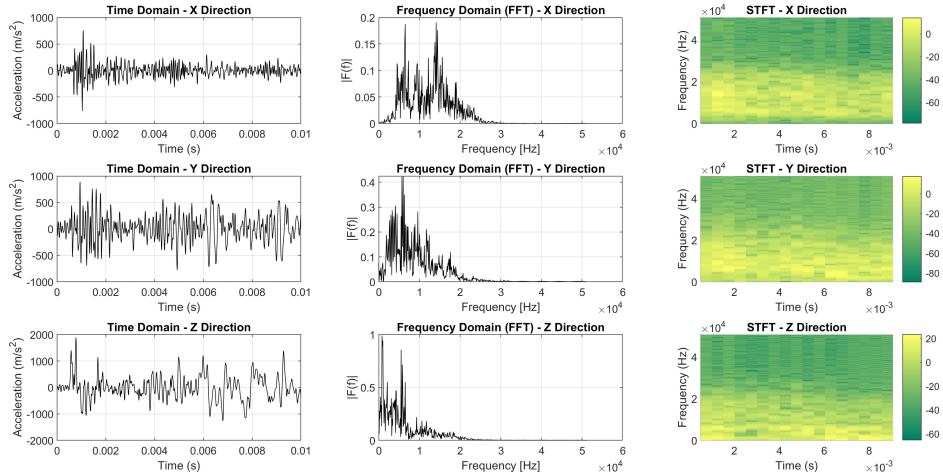


Figure 6.10: Acceleration of concrete node B, $\zeta_M = 4\%$, $\zeta_K = 4\%$ - Model 2

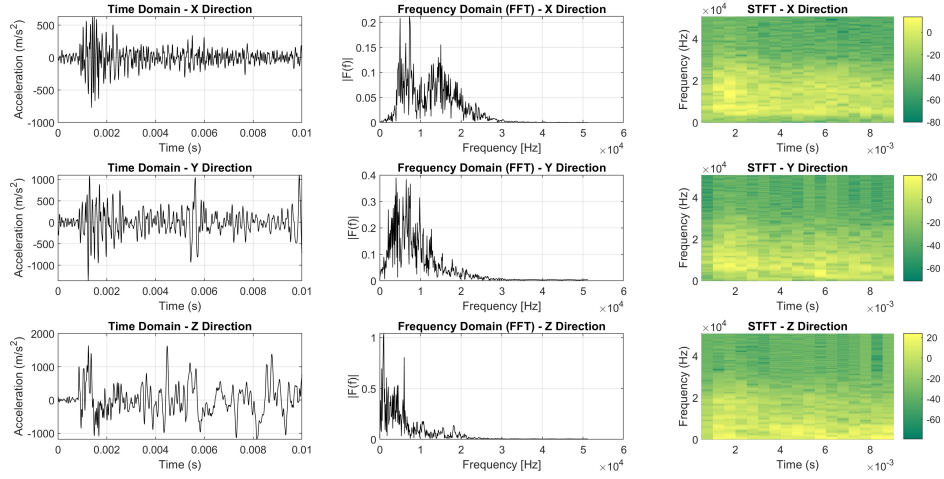


Figure 6.11: Acceleration of concrete node C, $\zeta_M = 4\%$, $\zeta_K = 4\%$ - Model 2

Some observations can be made from the results of the developed larger model. Considering that the purpose of this model was to be able to achieve a cleaner wave without reflections from the section boundary for a significant period of time, it can be seen in the time-domain representation that there is a moment in which the wave reaches the node in analysis, followed by a dissipation phase and once again the wave which has traveled from the point in analysis to the section boundary comes back, this is evident due to the amplitude increase of the peaks past the attenuation phase. As for the frequency-domain plots the results are coherent with the smaller model given that the concentration of dominant frequencies is primarily focused on the lower ones.

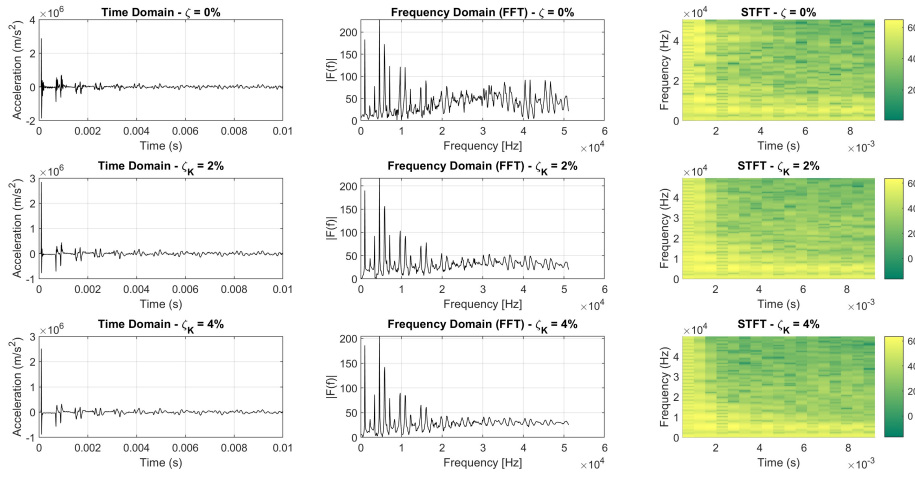
6.3.2 Nodal Accelerations - Steel Boundary

The present section displays the nodal data from the selected nodes on the steel boundary for both developed models. As for Model 1, similar to the previous section, data will be presented for a single node positioned 1.25 meters from the cut, in total, seven datasets are shown each one representing each of the submodels defined by different damping definitions. Data from Model 2 is referred also to just one node located 2.5 meters from the cut. Contrary to the displayed datasets from the concrete boundary, since steel acts as a waveguide, this section will only display the accelerations in the longitudinal direction (Z-axis for the defined coordinate system).

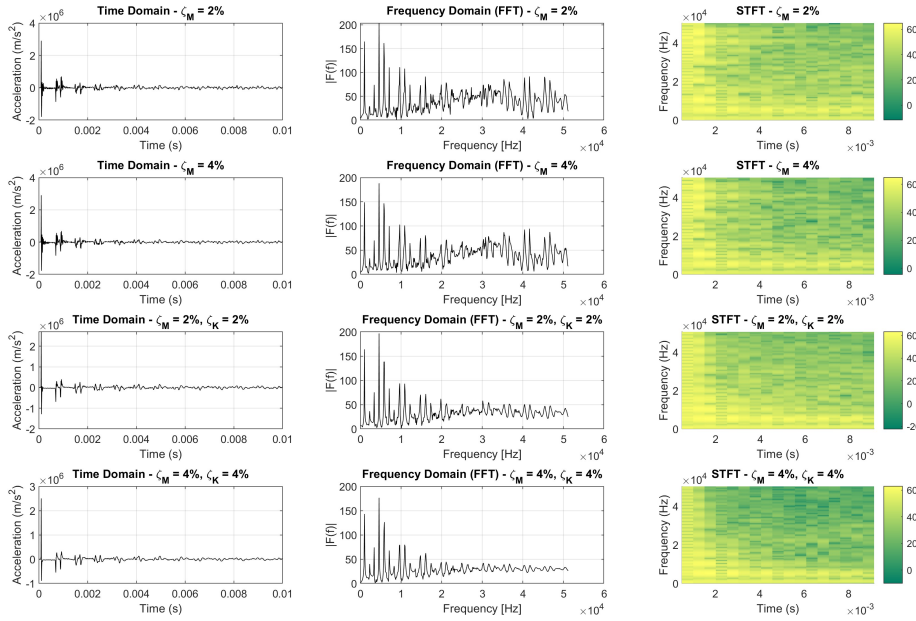
Model 1

Figures 6.12a and 6.12b summarize the data collected from the node of Model 1 for all the different cases of damping used. The data is displayed both in time and

frequency-domain.



(a)



(b)

Figure 6.12: Acceleration of steel node - Model 1

Regarding the acceleration data from the steel node, several interesting observations can be made. First, there is a clear distinction between waves propagating through the steel compared to those in the concrete. Since the steel tendon acts as a waveguide, it is possible to observe each individual wave passing through the node under analysis. Furthermore, in the absence of damping, the wave maintains high-frequency components for a longer duration. As stiffness-proportional damp-

ing is introduced, higher frequencies are gradually suppressed, with a value of 4% being the most effective in suppressing the higher frequencies of the system. In contrast, the introduction of mass-proportional damping has a minimal effect on the higher frequencies. Also, the spectrogram provided by short time Fourier transform (STFT) offers insightful information, near the time of the cut is observable that not just the lower frequencies are the ones with the most power spectral density but a broad range of frequencies are being excited. Finally, the combination of both mass and stiffness-proportional damping at 4% provides the most stable response in the frequency domain.

Model 2

As for Model 2, figure 6.13 displays the results obtained for the node positioned 2.5 meters from the cut on the steel boundary.

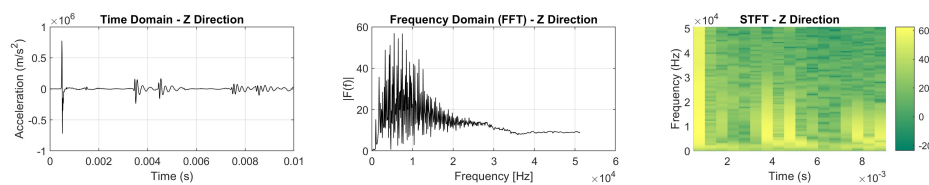


Figure 6.13: Acceleration of steel node - Model 2

Given the larger size and, consequently, the greater distances the propagating wave must travel before reflecting back, it is easier to observe each individual wave as it reaches the node under analysis. Since the position of the node is closer to the cut than to the section boundary, it is clear when the wave passes through the node, allowing us to distinguish whether the reflection is caused by the section boundary or the steel cut location. The first peak represents the initial instance when the wave reaches the node coming from the cut location. Subsequently, the wave travels through the steel tendon twice the distance from the node to the section boundary, reaching the node again (evident in the second peak). It then continues traveling to the cut location and returns (a distance of 5 meters), which is indicated by the third peak, closely separated from the second peak by a few milliseconds.

As a means of validating the model, it is possible to compute the velocity of the wave based on the traveled distance and the time it takes to reach the node (derived from the different peaks and node location), and compare it to the theoretical primary wave velocity computed from equation 3.22 for the steel material properties.

$$v_{p\text{theoretical}} = \sqrt{\frac{E(1-\nu)}{\rho(1+\nu)(1-2\nu)}} = 5890 \text{ m/s (theoretical)} \quad (6.1)$$

$$v_{p\text{numerical}} = \frac{2 \times (Z_{\text{end}} - Z_{\text{node}})}{t_{\text{peak}_2} - t_{\text{peak}_1}} = \frac{2 \times (20 - 12.5)}{0.00415 - 0.00152} = 5700 \text{ m/s (numerical)} \quad (6.2)$$

The theoretical primary wave velocity calculated from equation 3.22 for the steel material properties is 5890 m/s, while the results from the numerical model indicate 5700 m/s. There is a slight discrepancy between the theoretical and numerical values, which falls within an acceptable range. Considering factors such as numerical approximation, time step used, and mesh discretization, the difference between the computed values remains at around 3%. Overall, the close numerical relation between these values supports the accuracy of the model and its reliability in representing wave propagation.

Additionally, something more evident from the results of the larger model compared to the smaller one is the presence of residual higher frequencies, noticeable in the frequency domain plot of figure 6.13. A deeper analysis revealed that these residual frequencies originate from the transient effects caused by the initial release of energy due to the steel tendon's rupture, also observable from the STFT spectrogram. In figure 6.14, which represents a section of the data presented in figure 6.13 without considering the first arrival of the wave to the node, the results indicate that this first peak is responsible for generating the residual higher frequencies, just as the STFT spectrogram shows, coming from the immediate and transient response of the steel rupture.

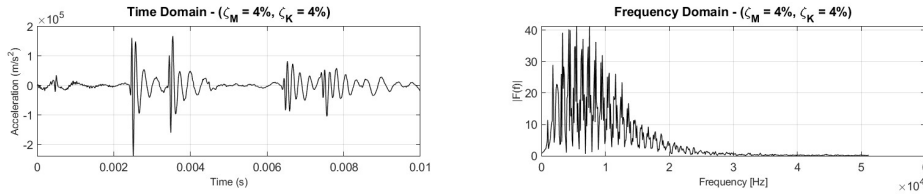
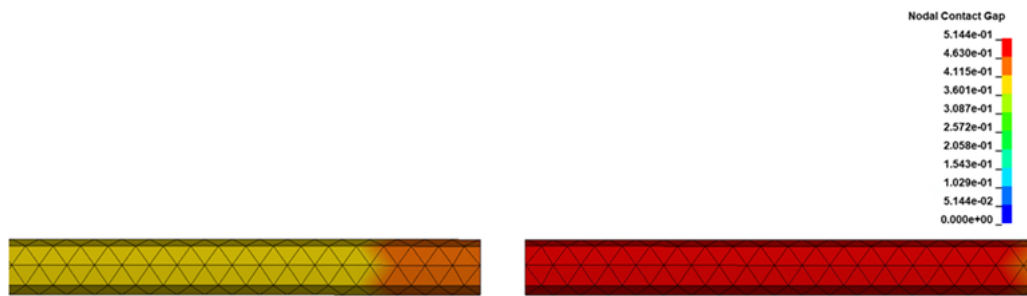


Figure 6.14: Trimmed acceleration of steel node - Model 2

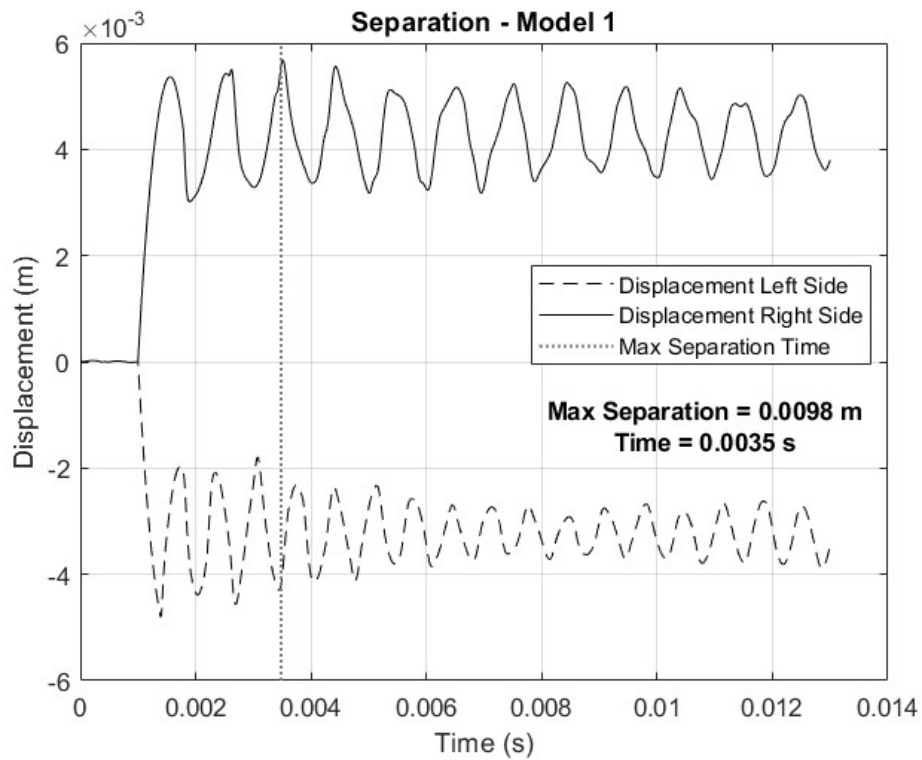
6.3.3 Slippage behavior - Steel separation

This section is dedicated to evaluating the slippage behavior in the contact between steel and concrete for both models. Displacement data is important as it allows us to verify if the contact definition between concrete and steel has been properly defined,

and whether the values from the numerical simulations are coherent with the expected values from the real phenomenon. Figures 6.15 and 6.16 display the results for the two developed models.

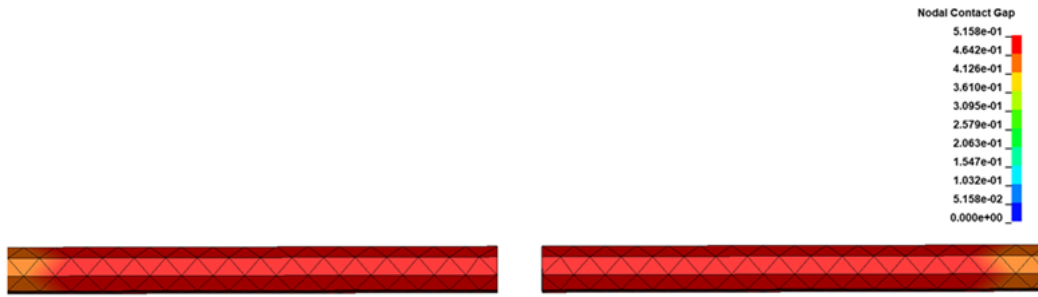


(a)

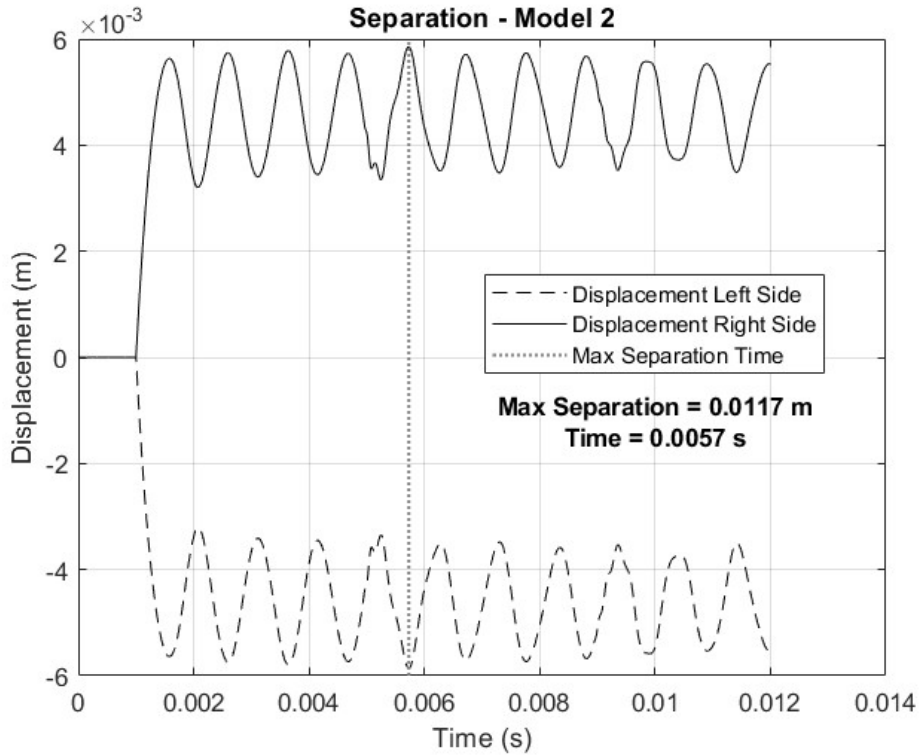


(b)

Figure 6.15: Steel parts separation - Model 1



(a)



(b)

Figure 6.16: Steel parts separation - Model 2

Based on the results presented above, both models show similar values of maximum separation between the cut steel tendons, roughly averaging 1 centimeter. This outcome is consistent with the expected values from real behavior, suggesting that the contact definition between material parts was well defined. Even though the sizes of both models differ significantly, the separation between steel parts primarily depends on the anchorage length. This is because not all of the contact length between material parts will be equally affected by the rupture phenomenon. Referring to the bilinear cohesive law defined in figure 5.4, near the cut, the contact behaves plastically (2nd phase of the bilinear behavior), which is where slippage occurs, while the rest of the contact behaves elastically (1st phase of the contact), with no plastic deformation

or slippage. Therefore, if the contact length is sufficiently large to develop the necessary anchorage, enlarging the problem in the longitudinal axis should not significantly affect the separation between steel tendon parts.

Chapter 7

Model & Data Validation

7.1 Mesh

As stated in Section 4.2.5, mesh control is of primary importance in ensuring that the model accurately represents real-world behavior. From the parameters defined in the referenced section, we can validate that the model's mesh is appropriately defined. The quality of the mesh is crucial because it directly influences both the geometric and physical characteristics of the problem. If the mesh parameters significantly deviate from the recommended thresholds, it is a clear indicator that the results may be inaccurate or unreliable.

7.1.1 Mesh Control Parameters Verification

Two key parameters are defined for evaluating the mesh and element quality: the element Jacobians and the aspect ratio. The element Jacobians provide essential information about the shape and geometry of the mesh elements, helping to detect any distortions that could affect the simulation's accuracy. The aspect ratio serves as a metric to assess the shape quality of the elements, ensuring they meet the required standards for reliable modeling.

Elements Jacobians

Following the recommended values for element Jacobians described by the literature, specified in Section 4.2.5, for the realized mesh, Figure 7.1 show the results for the element Jacobians.

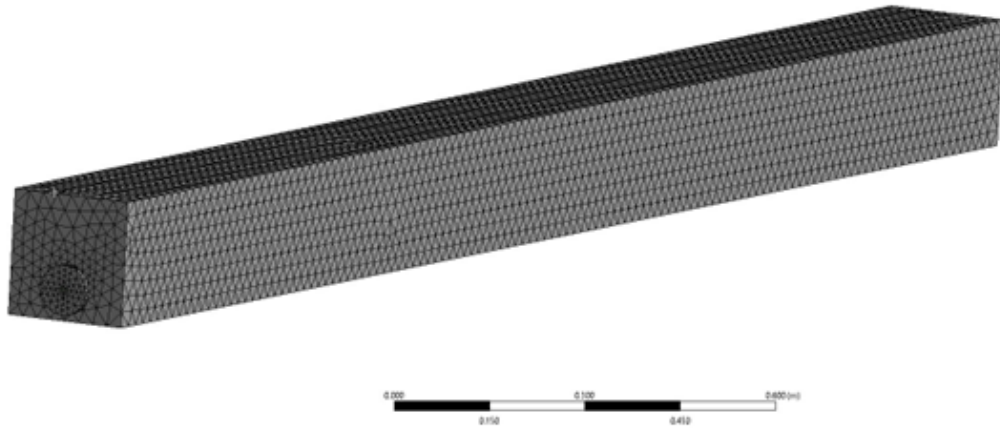


Figure 7.1: Element Jacobians

It is also shown using the histogram referenced in Figure 7.2 the total amount of elements for each value, as seen, all of the elements Jacobians belong to the value of unity which states that the mesh evaluated by this means is of good quality.

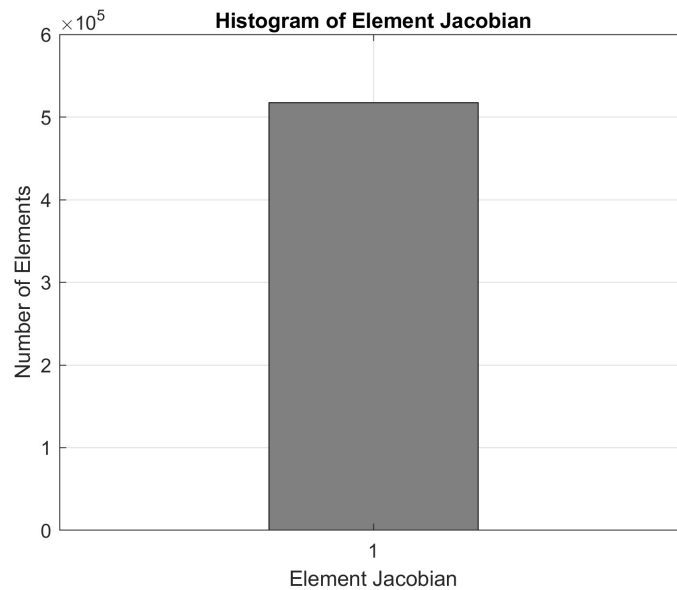


Figure 7.2: Element Jacobians Histogram

Aspect Ratio

The verification of the aspect ratio for the different elements of the mesh was realized once again following the criteria stated in the different literature, expressed in Section 4.2.5. Figure 7.3 shows the different results obtained for the different values of aspect ratio of the elements, specifically Figure 7.3a shows the elements with values

of aspect ratios close to 1.6, Figure 7.3b shows aspect ratios of 2.5, and Figure 7.3c shows elements with aspect ratios above 4.

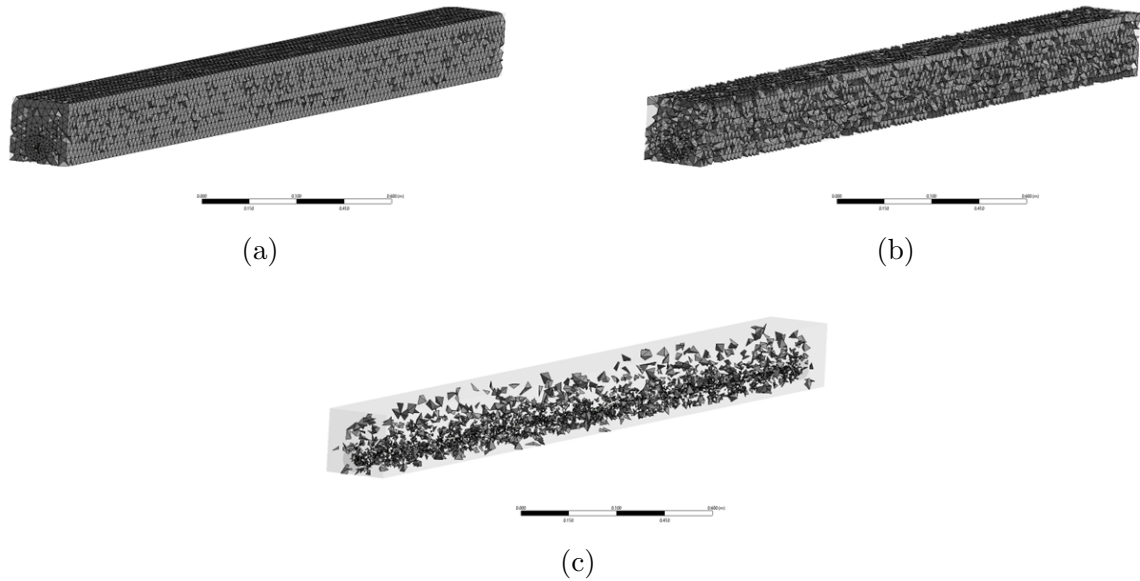


Figure 7.3: Aspect ratio results

Similarly to the analysis done for element Jacobian verifications, it is presented in Figure 7.4 a histogram in which is possible to appreciate the different values of aspect ratios with its corresponding number of elements

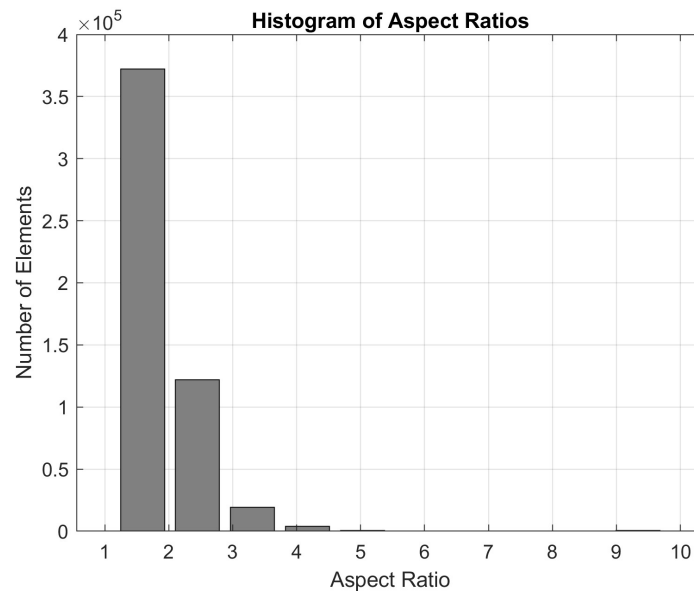


Figure 7.4: Aspect Ratio Histogram

Consequently is is verified the mesh quality by means of the pre-established criteria,

99% of the element's aspect ratios are below the value of 4, where 73% have aspect ratios of 1.6, and less than 1% are above 4.

Skewness

The skewness value should be near zero for a better-defined mesh and below 0.9 in every case, for best accuracy the majority of the elements should have values below 0.5. Figure 7.5 shows the results for the different threshold values. Figure 7.5a illustrates the elements with skewness below 0.5, Figure 7.5b elements with more than 0.5, and Figure 7.5c shows elements with skewness values above 0.65.

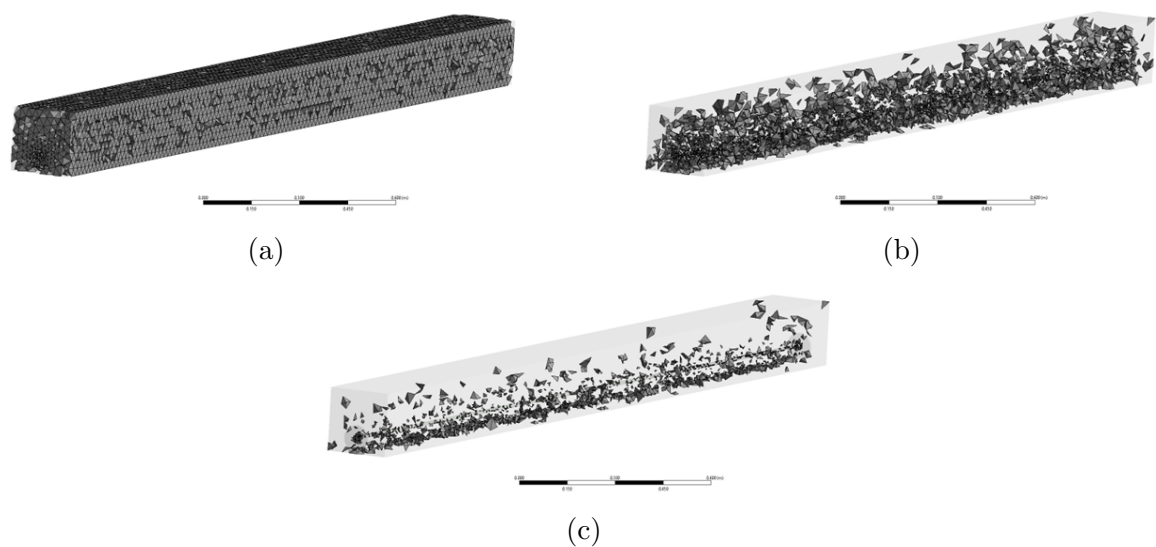


Figure 7.5: Skewness results

Finally, the data is also presented in the histogram illustrated in Figure 7.6.

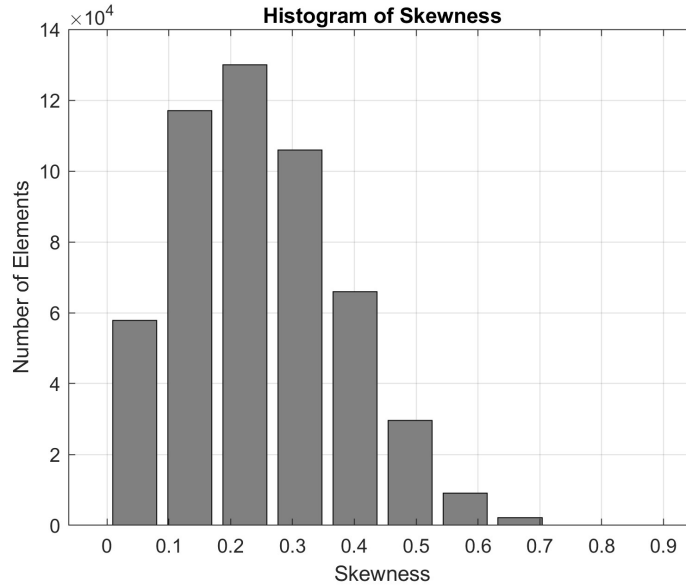


Figure 7.6: Skewness Histogram

The total amount of elements with skewness values above 0.5 is 2.2%, and 58% of the total number of elements have skewness values below 0.25, which is sufficient to establish the validation of the model in terms of mesh shape and geometry.

7.1.2 Mesh Sensitivity

Mesh sensitivity analysis is a critical aspect of FEA, which involves evaluating how the results of a simulation vary with changes in the mesh size and configuration. The accuracy, convergence, and computational cost of FEM solutions heavily depend on the choice of mesh elements, their size, and the refinement strategy employed. Mesh sensitivity is directly related to with the influence of numerical diffusion on the solution [34] which can be understand as the variation from the simulation results compared to the real physical system.

Mesh sensitivity analysis is essential to ensure the reliability and accuracy of FEM results. The discretization of a continuous domain into finite elements introduces numerical errors that can affect the solution. These errors are influenced by the element type, size, shape, and distribution within the mesh. Numerical diffusion needs to be minimized by either refining the mesh and/or using higher-order discretization schemes [34].

For the present study, since element size is directly correlated to wave propagation and wavelength resolution (see section 4.2.3) a variation in the mesh size was applied in order to appreciate how the utilization of a finer mesh affects the simulation results.

A model following the same parameters from them ones used to obtain the results was made with the distinction of the size, going from 35 millimeters of maximum size at the boundary of the concrete to 15 millimeters, in this way a reduction of 55% was realized for the maximum element size. As for the steel, element size was varied between models between 8 to 6 millimeters. In total 6 models were developed Table 7.1 specified the considerations for each one of them.

Table 7.1: Sensitivity Analysis Models

Model	Element Size [mm]		Total Elements	Total	
	Concrete	Steel		Nodes	Running Time
1	35	8	61,497	14,854	51 min
2	35	6	75,111	18,202	1 hr 18 min
3	25	8	90,241	20,716	1 hr 5 min
4	25	6	103,629	24,029	1 hr 35 min
5	15	8	264,309	54,086	2 hr 20 min
6	15	6	277,020	57,280	3 hr 46 min

The comparison analysis between models will be done regarding system energy and acceleration at points equally spaced from the cut for all the models.

First, acceleration data is plotted, figures 7.7 and 7.8 show the data in time and frequency domain for all the cases considered.

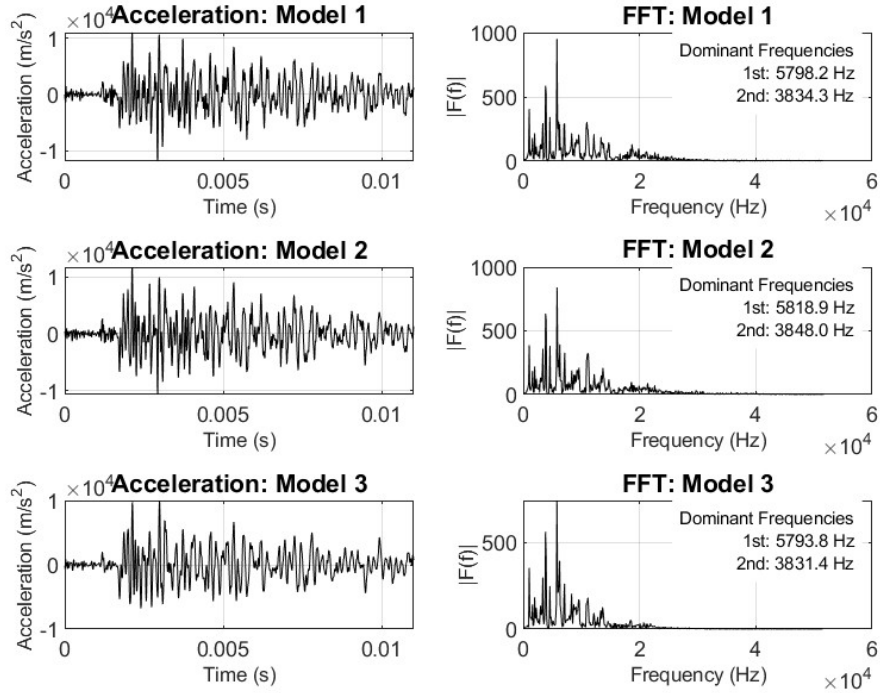


Figure 7.7: Acceleration Models 1, 2 and 3

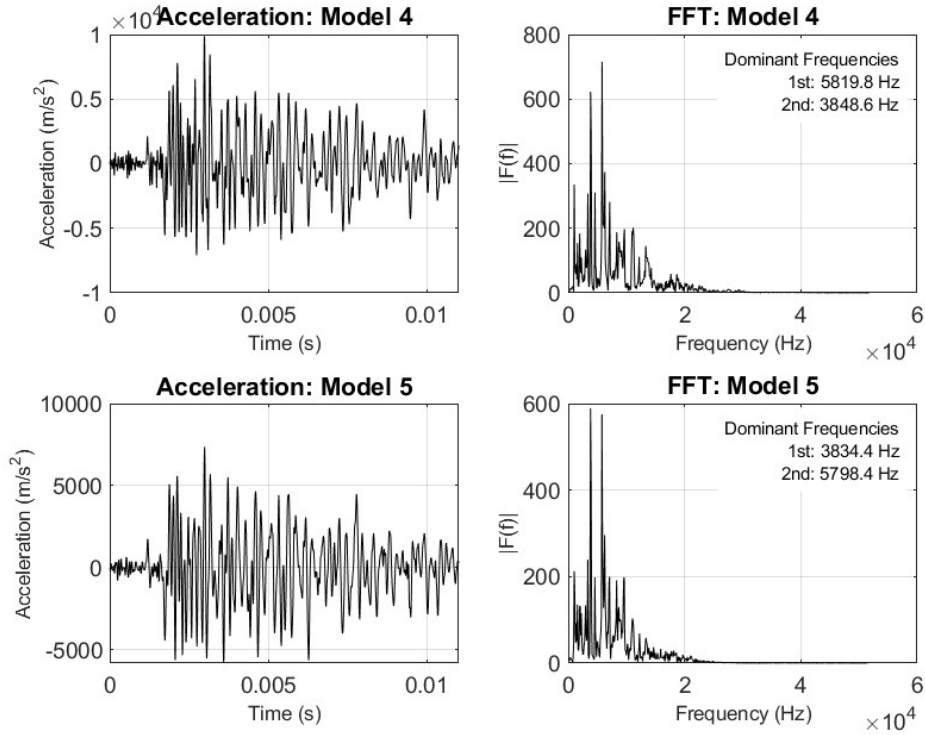


Figure 7.8: Acceleration Models 4 and 5

From the model's data collection, a summarized table with the relevant results is shown, the total energy referred to in table 7.2 is computed approximating the area under the time-history curve with trapezoidal rule, and the root mean square amplitude represents a measure to determine the magnitude variation between signals.

Table 7.2: Time Domain Sensitivity Results

Model	Max Amplitude	Time at Max (s)	RMS Amplitude	Total Energy
1	10973.0	0.00212	2832.4	88376
2	11722.0	0.00213	2861.0	90131
3	9957.5	0.00299	2338.7	60246
4	9877.4	0.00298	2394.6	63162
5	7362.8	0.00299	1980.8	43247
6	7413.6	0.00299	2075.8	47474

From the time domain results, key aspects between models are present. First, the variation between max amplitude and RMS amplitude values, with the coarser Models 1 and 2 having the greater ones signifying a greater degree of energy in the system. In contrast, as mesh size decreases, in Models 5 and 6 a clear reduction in amplitude is observed, highlighting how finer meshes lead to a more accurate representation of

the system's energy, due to its limited resolution, coarser meshes tend to overestimate the system's energy.

Table 7.3: Frequency Domain Sensitivity Results

Model	Dominant Frequency (Hz)	2nd Dominant Frequency (Hz)
1	5798.2	3834.3
2	5818.9	3848.0
3	5793.8	3831.4
4	5819.8	3848.6
5	5798.4	3834.4
6	3848.7	5819.9

From the frequency domain analysis, an interesting pattern arises. The relation between mesh size and dominant frequency is evident, coarser meshes such as Model 1 and 2 tend to both intensify higher frequencies and diminish or not accurately capture lower frequencies. This pattern is appreciable as higher frequencies tend to be the dominant ones for coarser meshes while lower frequencies are for the finer mesh models. As the element size is reduced the second dominant frequency becomes the dominant one. this shift highlights the capability of finer meshes to better represent and capture the lower frequency content of the system.

Finally, the systems energy data are also plotted, from figure 7.9 to 7.14 the relevant energy components variation for each model are displayed.

Energy Components Variation - Model 1

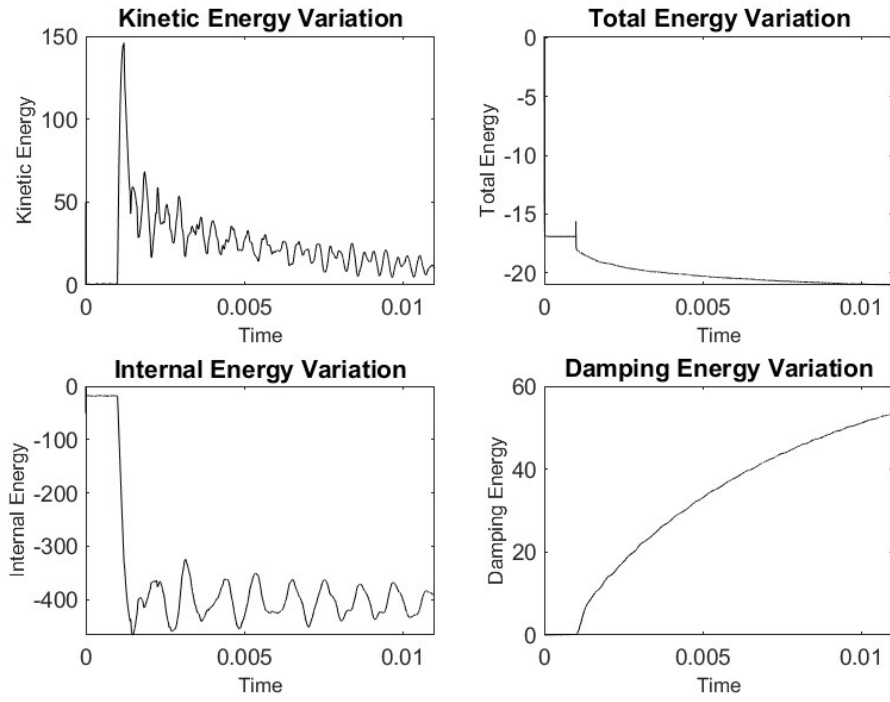


Figure 7.9: Energy Components Variation - Model 1

Energy Components Variation - Model 2

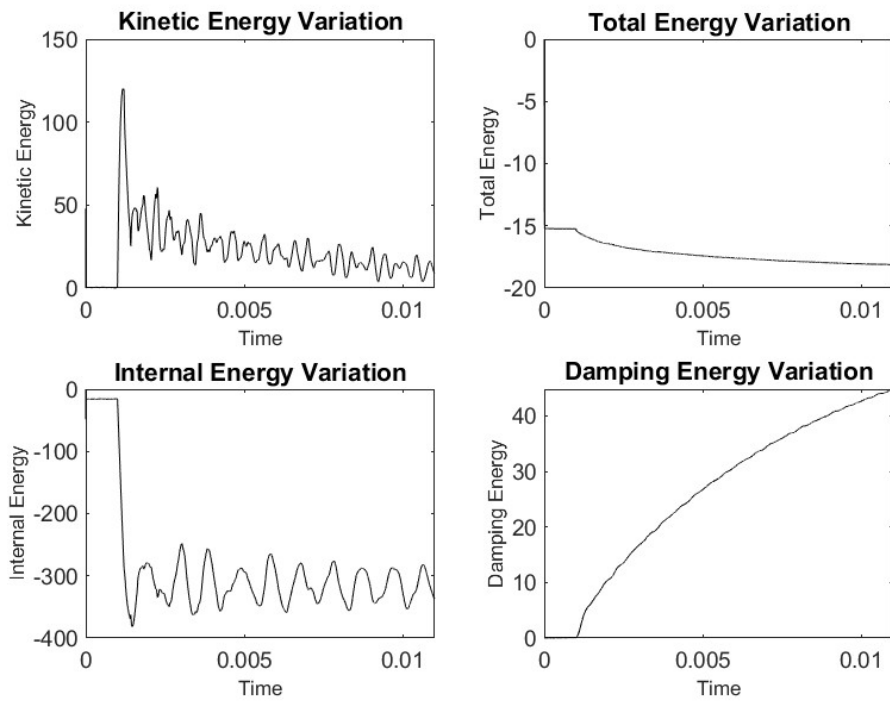


Figure 7.10: Energy Components Variation - Model 1

Energy Components Variation - Model 3

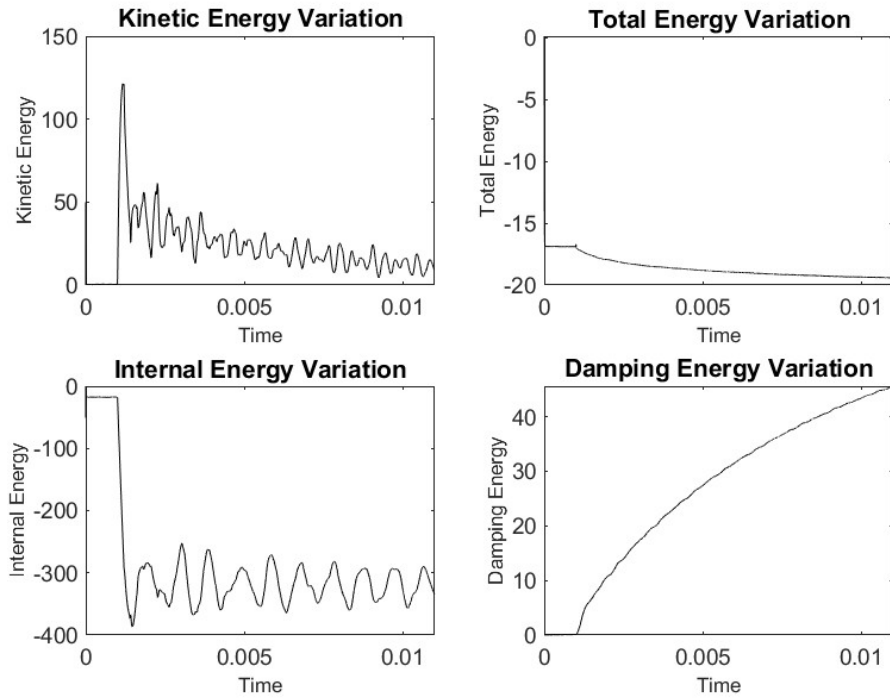


Figure 7.11: Energy Components Variation - Model 1

Energy Components Variation - Model 4

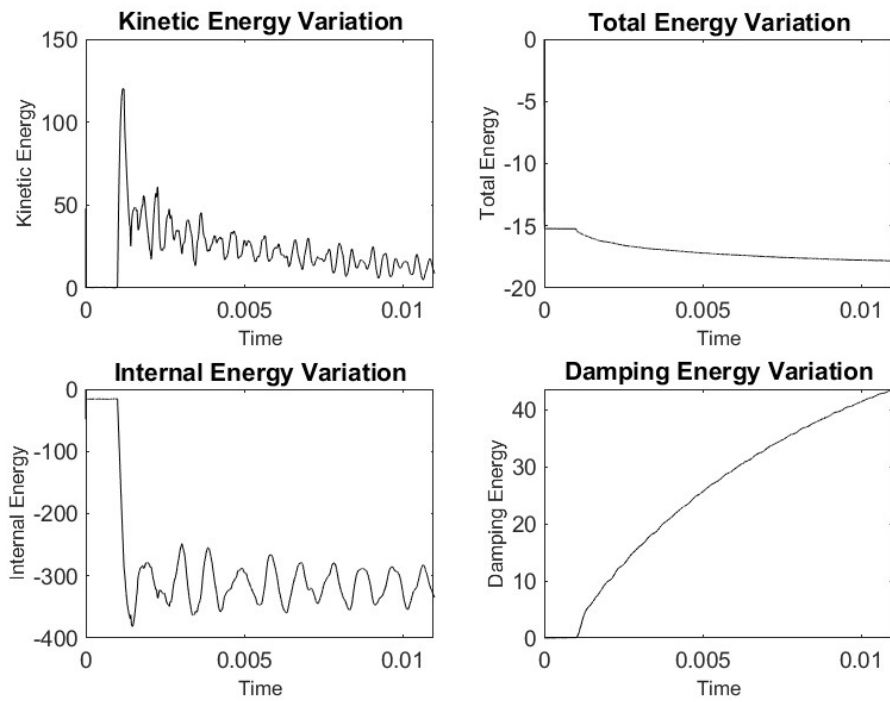


Figure 7.12: Energy Components Variation - Model 1

Energy Components Variation - Model 5

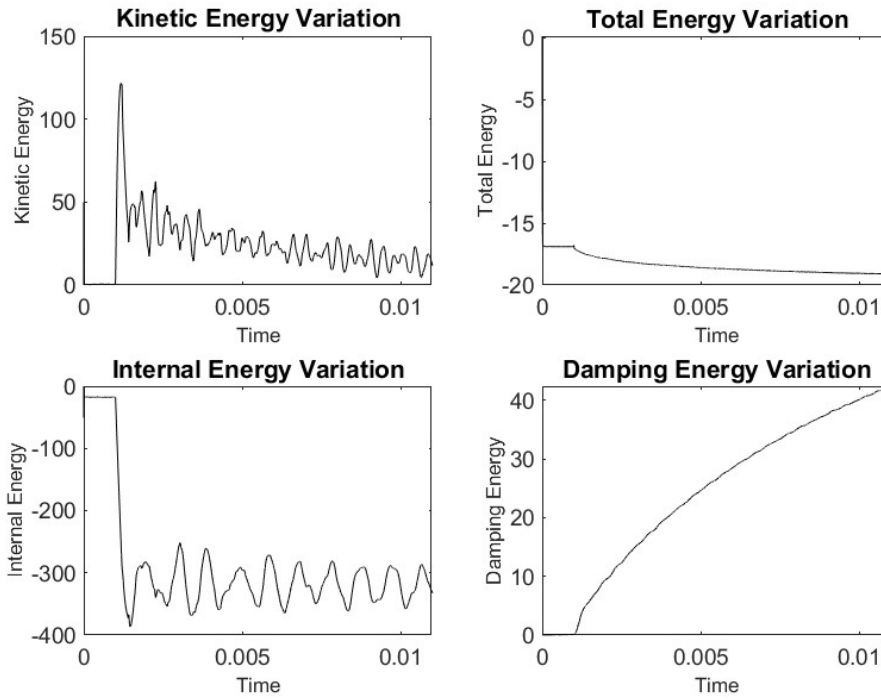


Figure 7.13: Energy Components Variation - Model 1

Energy Components Variation - Model 6

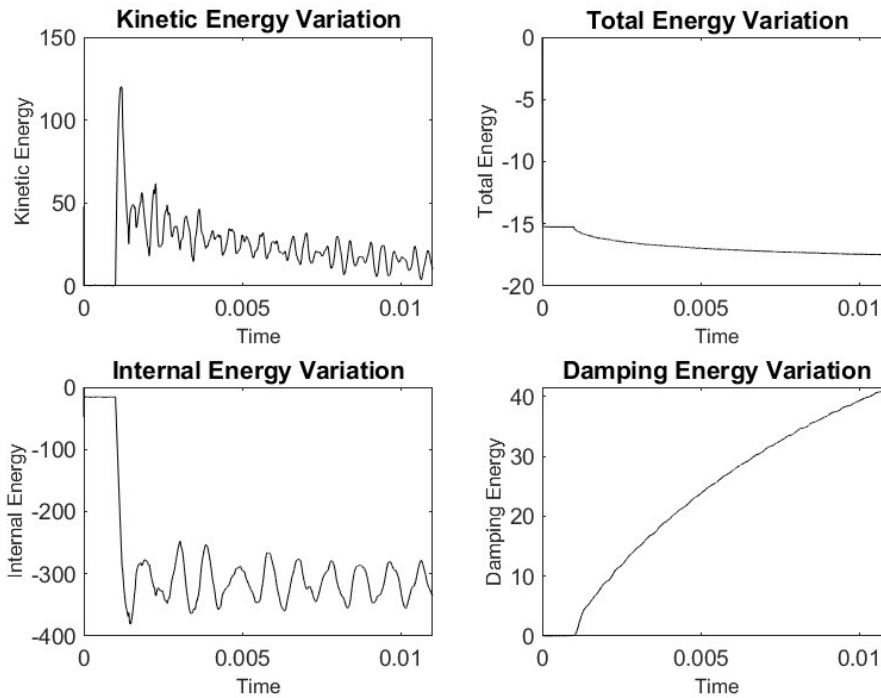


Figure 7.14: Energy Components Variation - Model 1

As a comparative way, the plots between the coarser model (Model 1) and the finer

one (Model 6) are plotted superposed in figure 7.15.

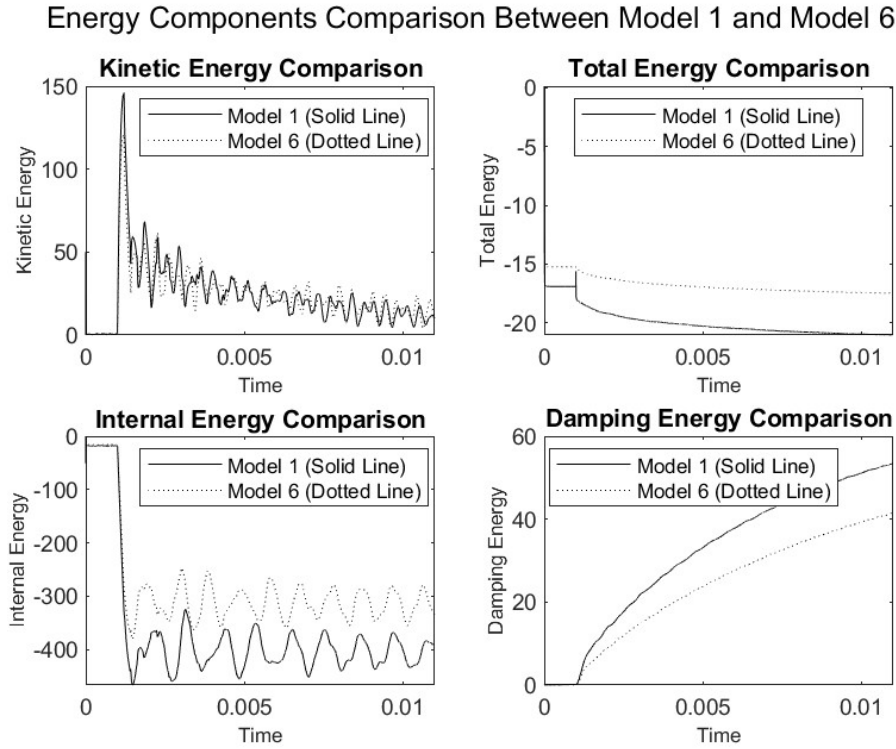


Figure 7.15: Energy Components Comparison - Model 1 and 6

From the energy components comparison between Model 1 and Model 6, significant differences are evident. Concerning the kinetic energy plot, the coarser Model shows higher initial peaks indicating its tendency to retain and amplify kinetic energy. As for the total energy, Model 1 shows a faster energy decay than Model 6, which is consistent with higher numerical dissipation and less controlled energy decay, this pattern is also evident in the damping energy plot. Finally, the internal energy plot further supports this trend. As seen in Table 7.2 Model 1 amplifies the energy, contributing to the observed shift in the system's energy and the higher less controlled energy decay.

7.2 Energy Balance

The present section focuses on verifying the developed models through an energy balance approach. Ensuring that the models aligns with the fundamental principles of physics is essential to validating their accuracy and reliability. The energy balance method is a crucial step in model verification as it assesses whether the system's energy remains consistent throughout the simulation, indicating that the model behaves as expected under the conditions imposed. This chapter presents the energy data ob-

tained from the numerical simulations and discusses how these results support the validity of the model. Given the nature of ensuring precise model behavior results presented in this section will be limited to the larger model, Model 2, being the coarser one.

Model assurance verification searches to confirm that the model behaves the following the basic laws of physics [23], for this, the total energy must be checked for balance, to be certain that no major inconsistencies in the energy of the system are present on the model [26]. This can be achieved by considering a variation less than 10% on the total energy of the system [23].

Energy data of the system over time is summarized in a condensed table, referenced in table 7.4.

Table 7.4: Energy data

Time (s)	Kinetic	Internal	Damping	Sliding	Total
1.51e-05	6.69	-117.26	0.05	0.15	-110.37
1.35e-03	89.35	-578.79	2.18	373.49	-113.77
2.68e-03	36.61	-654.49	5.62	498.15	-114.11
4.01e-03	45.63	-503.28	9.05	334.12	-114.49
5.34e-03	45.53	-506.55	12.03	334.35	-114.64
6.67e-03	26.65	-637.76	14.91	481.46	-114.74
8.00e-03	43.45	-602.32	17.34	426.65	-114.89
9.33e-03	19.91	-470.91	19.80	316.23	-114.98
1.07e-02	47.08	-579.80	22.31	395.37	-115.04
1.20e-02	20.90	-648.27	24.74	487.49	-115.13

From the extended data collected from the model, the different energy components are plotted in figure 7.16 and 7.17.

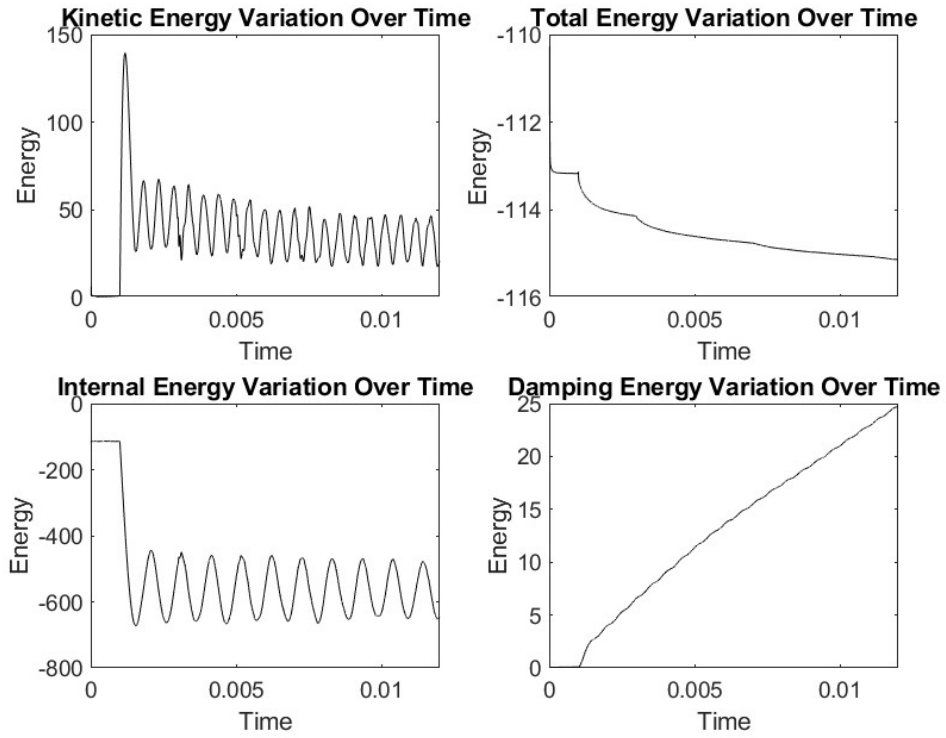


Figure 7.16: Energy components - Model 2

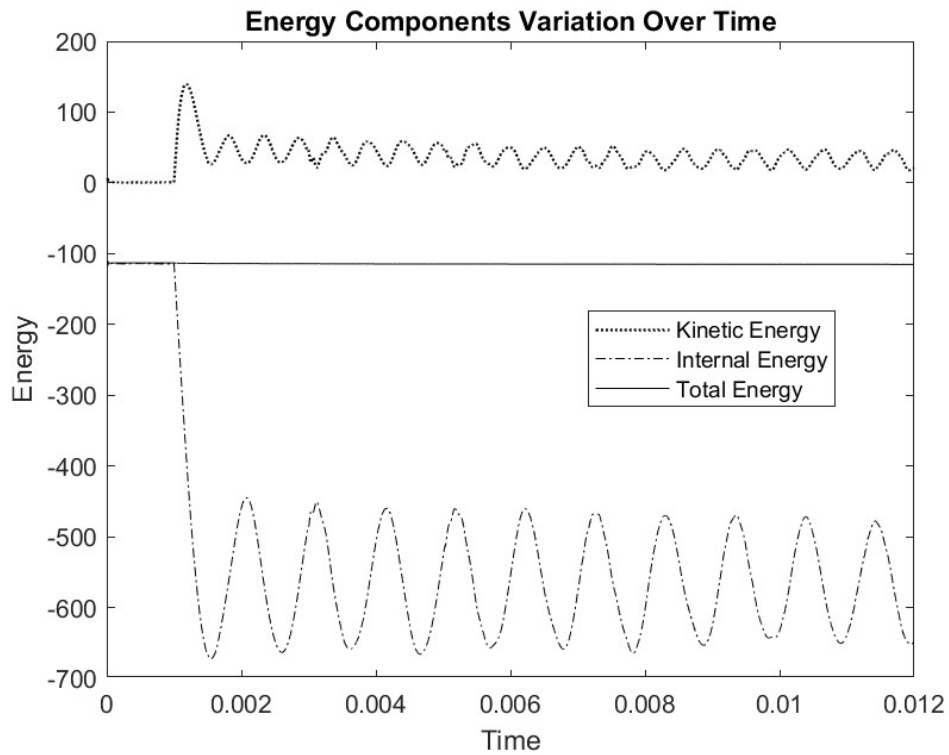


Figure 7.17: Energy Balance - Model 2

Several key observations can be made from the energy data. First, the kinetic

energy initially remains low, indicating minimal displacement, but it significantly increases after the introduction of the cut, as expected. Subsequent, energy levels noticeable start decreasing returning to lower levels, this behavior is coherent with the transient effect given by the introduction of the cut. This rise reflects the dynamic response of the system.

Secondly, the internal energy remains negative, which aligns with the model's behavior, as the system is primarily in a compressive state, releasing stored strain energy, also the internal energy oscillating by a lower value rather than the initial one follows the real behavior, as some permanent deformations are present even though the material is elastic. The nature of the separation of the steel tendons induces an unrecoverable deformation.

On the other hand, the damping energy, which consistently shows positive values contributes decreasing the internal energy as the event proceeds. The sliding energy, related primarily to the cohesive contact behavior defined in Section 5.1.4, represents the energy loss due to relative movement between contact interfaces. Lastly, the total energy, resulting from the combination of these components, remains primarily negative, driven by the internal energy but stays relatively constant, without spikes or unusual behavior, the overall variation of total energy of the system is less than 5% which confirms that the system behaves in a physically coherent manner.

7.3 Data Validation

The results are validated through comparison with experimental data. This data was obtained by physically cutting a tendon in a prestressed reinforced concrete beam, with accelerometers placed approximately 4.5 meters from the cut to collect the data. The measurements were processed as an audio signal. to be able to compare them with the numerical data, the same format as the one used in Section 6.3 is presented.

7.3.1 Experimental Results

From Figure 7.18 to 7.27 experimental results are displayed.

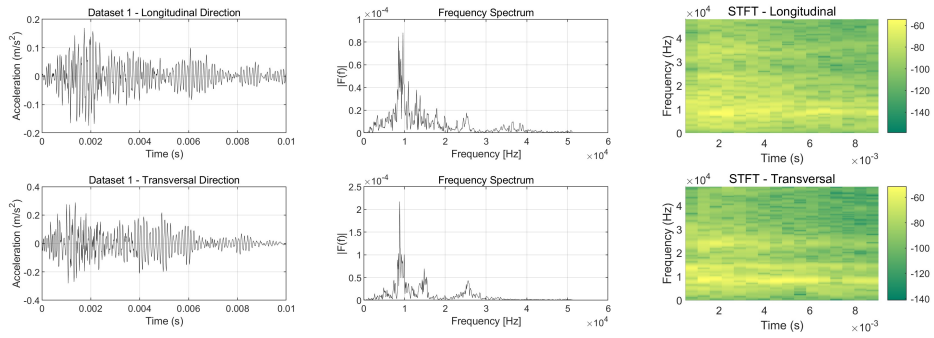


Figure 7.18: Acceleration - Experimental dataset 1

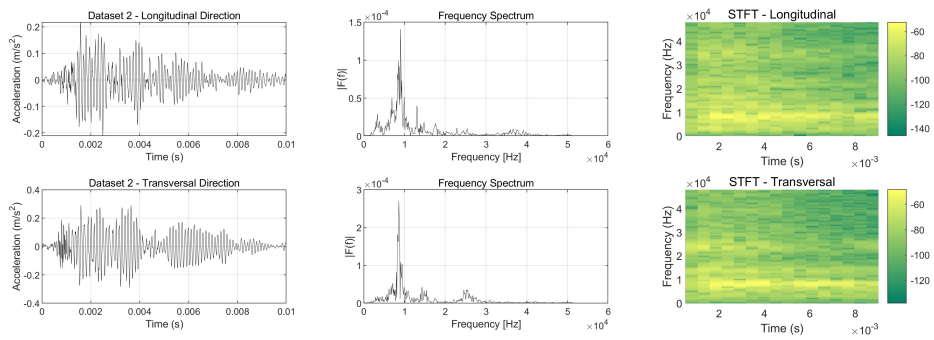


Figure 7.19: Acceleration - Experimental dataset 2

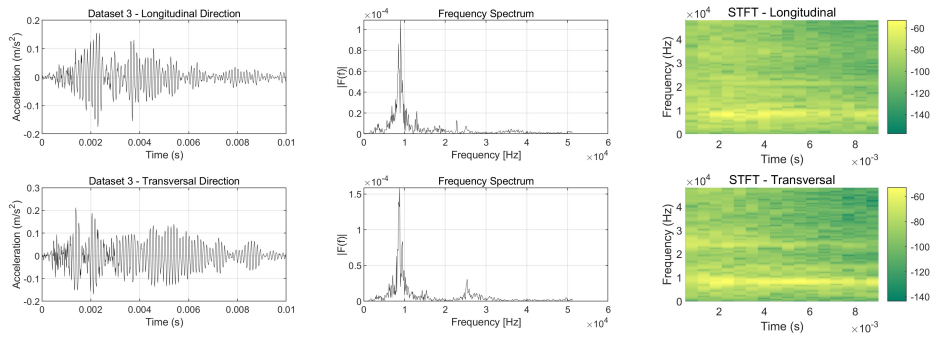


Figure 7.20: Acceleration - Experimental dataset 3

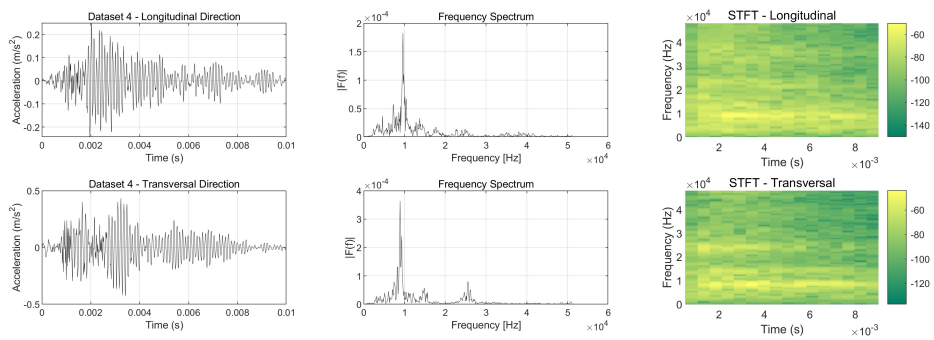


Figure 7.21: Acceleration - Experimental dataset 4

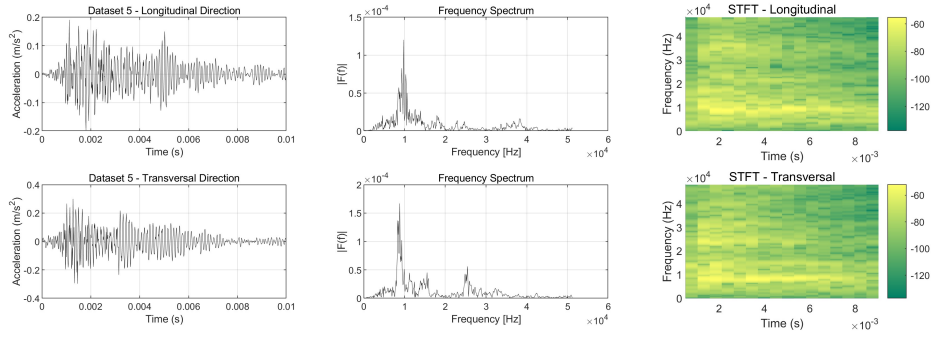


Figure 7.22: Acceleration - Experimental dataset 5

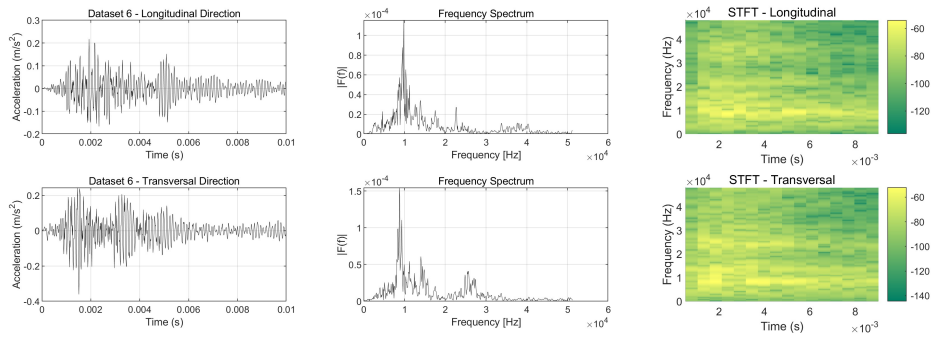


Figure 7.23: Acceleration - Experimental dataset 6

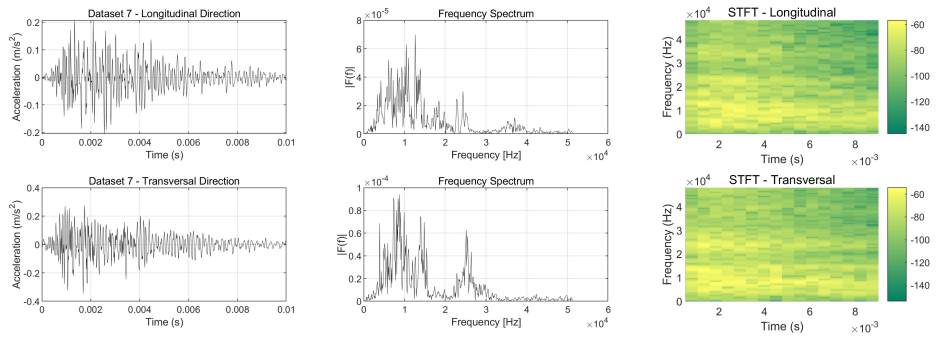


Figure 7.24: Acceleration - Experimental dataset 7

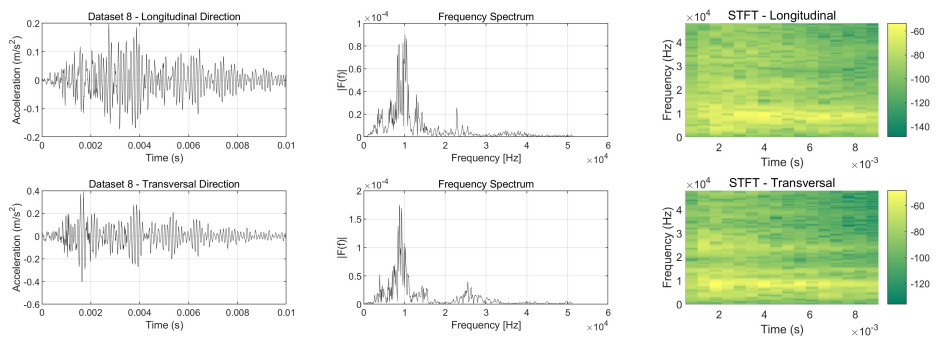


Figure 7.25: Acceleration - Experimental dataset 8

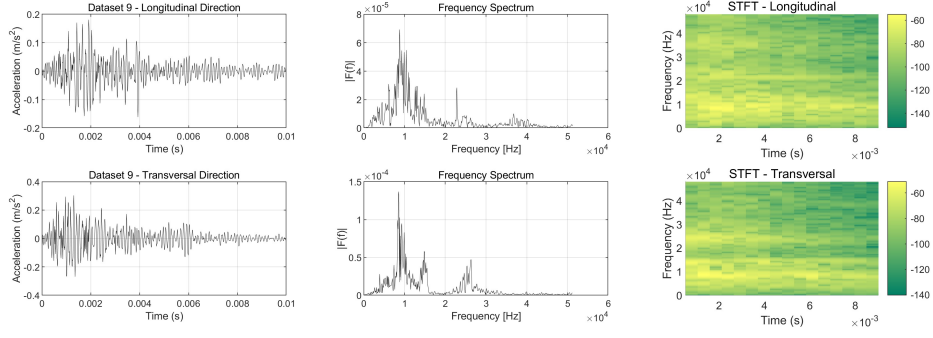


Figure 7.26: Acceleration - Experimental dataset 9

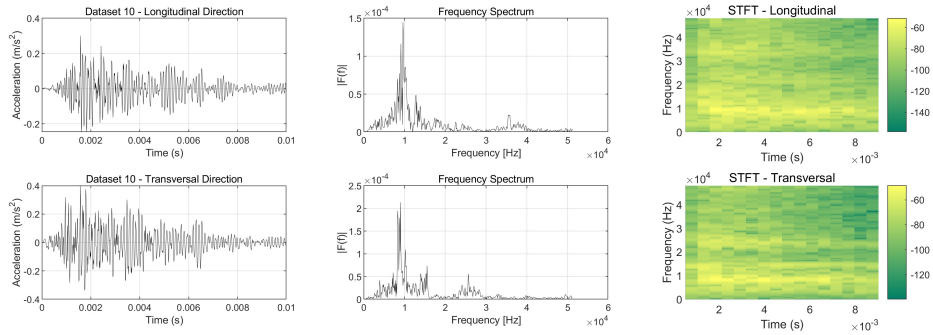


Figure 7.27: Acceleration - Experimental dataset 10

From the real datasets, some relevant observations are noticeable. First, the time it takes for the signal to significantly reduce is around 10 milliseconds. Dominant frequencies are located in the lower frequency range, and for most of the datasets, a highly dominant frequency is present. There are some high-frequency components, but they are significantly lower in magnitude compared to the lower frequencies.

7.3.2 Comparison Between Experimental and Numerical Data

Given the discrepancies between geometries, boundary conditions, and other factors in the numerical models compared to the experimental real case, a direct quantitative comparison could lead to misleading conclusions. For this reason, a qualitative approach offers a more suitable means of achieving a representative comparison.

Building on this qualitative approach, several similarities between the numerical damped cases and experimental data are apparent. Both share predominant frequencies in the low-frequency range (i.e. between 0 and 20,000 Hz). However, while the numerical results display a broader range of predominant frequencies, the experimental data generally shows just one dominant frequency. It's also worth noting that in the numerical undamped case displayed in figure 6.2, the higher frequency components

observed do not align with the experimental results. In contrast, the damped cases, especially those involving stiffness-proportional damping, such as the one shown in figure 6.8, align more closely with the experimental data. This highlights the importance of including damping to achieve a behavior close to reality of the model. As for Model 2 also lower frequencies are the dominant ones visible even in the time domain plots (see 6.9) but they are located in much smaller values than for the experimental results.

Furthermore, in the time domain, the results from Model 1 appear to be more consistent with of the experimental ones because, qualitatively, the waveform are more similar between results. This is based on visual analysis, as the shape of the wave in Model 1 closely resembles that of the experimental data. It's important to note that this model includes many wave reflections from the geometry boundaries during the analysis period, which seems to be contributing to its similarity with the experimental behavior.

On the other hand, the purpose of Model 2 was to extend the length of the model to track a wave without reflections for a significant period of time. However, when comparing its results to the experimental case, they do not align as well. In Model 2, wave dissipation, meaning the loss of acceleration over time, occurs much more quickly than in the experimental results. This could suggest that in the experimental case, there are also reflections present that help maintain the wave with a gradually decreasing amplitude over a longer period of time.

Additionally, when comparing Model 2 to the experimental data, before the reflected wave arrives, the acceleration amplitude in Model 2 has already significantly decreased. In contrast, in the experimental case, the amplitude has not yet reduced as much by that time, further suggesting that reflections may play a role in prolonging the wave behavior in the experimental results.

Chapter 8

Conclusion and Recommendations

8.1 Summary of Findings

This work has developed a series of numerical models, exploiting modern simulation software to simulate real behaviors accurately. Utilizing LS-DYNA, the numerical models have proved reliable in simulating the behavior of prestressed concrete beams, specifically modeling and analyzing the post-breakage dynamics. The integration of both implicit and explicit analyses was critical, with the implicit phase simulating the initial construction and stress equilibrium between the concrete and steel parts, and the explicit phase examining the dynamic rupture phenomena.

The comparison of numerical and experimental data shows an accurate alignment, validating the finite element models for simulating failure scenarios in the dynamic regime. To further validate the model and the result conveyed an analysis in terms of energy balance, mesh quality and mesh sensitivity was developed showing and reinforcing the validity of the results and its possibility to be used in structural health monitoring systems (SHM) as a predictive tool.

The study's focus on wave propagation, specifically on post-breakage dynamics offers key insights into how stress waves measured through acceleration travel through both steel and concrete parts, being crucial information for SHM applications as they can inform designed monitoring systems focused on detecting changes in wave patterns caused by structural damage. As the theoretical values align with the results found in the models, specifically in regards to wave speed for the different materials parts, key insights can serve to refine SHM systems by identifying distinct damage material-based wave propagation.

While an exact representation of a real system may be unattainable, the data

obtained from the numerical models aligned consistently with the results from real datasets. Geometry and boundary conditions of the beam elements play significant roles in how waves propagate, the presence and understanding of wave reflections from the different boundaries are essential for SHM systems to be calibrated.

Validation of the numerical model was achieved by comparison with experimental acceleration data recorded from a real beam. Even though the direct quantitative comparison was not realized given the differences between problems, the semi-qualitative comparison showed a sufficient degree of agreement, supporting the model's reliability in simulating the involved phenomenon. Specifically, the model's ability to replicate nodal acceleration patterns was critical, as these parameters are directly related to SHM sensors for analyzing structural integrity.

Energy balance analysis served as a tool for both validating the model and acquiring a better understanding of the phenomenon. Analyzing different energy components such as damping, internal, and kinetic energy, and their interactions helped determine if the model behavior aligns with the fundamental principles of physics while offering insights into how the models were behaving.

The cohesive type of contact used in the models yielded values consistent with real-world expectations. It accurately represented the behavior between steel and concrete after breakage, specifically the slippage, enhancing the model's conformity with actual scenarios.

A detailed analysis was conducted to understand the effects of different damping definitions and values on the system. Given that damping, and energy dissipation in general, is not a straightforward phenomenon in real systems, it was essential to analyze how changes in damping affected the overall results. Damping coefficients, particularly stiffness and mass-proportional damping, were varied to study their impact on energy dissipation. It was observed that both damping definitions, due to their distinct effects on the model's behavior, aligned in obtaining results compatible with those from real cases.

A comprehensive sensitivity analysis was done to understand the effects of different mesh sizes on the model's accuracy. As expected, finer mesh sizes resulted in more accurate wave propagation and representation, primarily in regards to lower frequencies. However, as the mesh size was increased, lower frequencies were partially filtered, and its amplitude was diminished. In contrast, as the mesh size decreased the computational demand was greatly increased, highlighting the importance of finding an efficient tradeoff between precision and efficiency.

One of the primary objectives of the present study was to be able to produce synthetic data that could be directly applied to SHM systems for real-time monitoring of prestressed concrete structures, an objective that was achieved and thoughtfully validated. This data allows the understanding of how the waves produced post tendon breakage propagate through the different material parts, SHM systems can be calibrated to detect these changes and allow sufficient time for maintenance and intervention and work as a prevention tool.

8.2 Study Limitations

Several considerations and limitations arise from numerical modeling, as it is always an approximated representation of reality. Aiming for a model that exactly mirrors real life is not realistic, since real case scenarios often involve a higher degree of heterogeneity. In the developed models, linear material properties were assumed for both steel and concrete, which do not fully account for the complex behavior of these materials, particularly under localized effects such as the steel rupture. Furthermore, nonlinearities in material behavior such as plastic deformation, were not considered, limiting the capacity of the models to represent the real scenario.

Boundary conditions were simplified to reduce computational complexity. In reality boundary conditions in bridges can be far more complex, including the type of connections, and varying load, this simplification may limit the model's applicability to highly detailed real conditions. Additionally, assuming homogeneity in materials, particularly in concrete, does not accurately represent the material real characteristics. The presence of different size aggregates directly affects the way the waves propagate through the medium and the waves sensors would be able to record.

Due to the high computational cost of explicit simulations, as the grade of fineness increases, the size of the problem had to be reduced. This was explicitly seen between Model 1 and Model 2. Model 1 utilized elements up to 35% smaller than those in Model 2. The coarsening of the mesh allowed the realization of a model 200% longer while maintaining acceptable running times but at the cost of reduced precision. Larger models with finer meshes required significantly more computational resources, exceeding the scope of this thesis. This tradeoff between computational efficiency and simulation accuracy was a key limitation, particularly in large-scale simulations, highlighting the need for more efficient computational methods or higher-performance computing resources in future studies.

Environmental and other external factors such as temperature and traffic loads

were not included in the simulations. Even though the rupture phenomenon is a "quasi-instantaneous" event, external factors can influence the material properties and existing stress states of the structure, potentially affecting the conditions under which the rupture occurs. When these factors are combined with the system's response, they can produce varied outcomes. Therefore, considering the combination of these external factors could lead to simulations that more accurately represent real-world behaviors.

The experimental validation was based on a limited amount of datasets, which may not fully capture the entire structural behavior. Contrary to the results provided by the models, the experimental datasets were all derived from just one accelerometer positioned in a constant location. Expanding the experimental datasets could provide a better means to further validate the model.

8.3 Practical Applications

The results of the present work could, as previously stated, be integrated into SHM systems for monitoring bridges, specifically the structural elements developed with prestressed concrete. By analyzing and collecting data on wave propagation, these systems could detect signs of tendon rupture, which are useful for damage prevention and early intervention. The specific data developed, mainly in terms of acceleration, serve as a mean to calibrate SHM systems for recognition of the phenomenon both in position and time of occurrence.

The findings of this study could contribute to enhancing the overall safety of critical infrastructure by providing more accurate methods for detecting structural failure. The numerical model could be used to set safety thresholds for prestressed concrete beams.

8.4 Recommendation for Future Research

Future research should focus on incorporating external factors, to achieve a more representative model. Factors such as temperature changes and the complexity of boundary conditions could be included in simulations to provide a more complete and comprehensive understanding of structural behavior.

Expanding the selection of material models to include nonlinearities and plastic deformation would improve the accuracy of the model. Additionally, a higher degree of mesh refinement could yield more accurate results for larger models. Although

the geometrical characteristics were under actual dimensions, increasing the variety of models varying both the section of the concrete beam and the diameter of the steel tendon would provide a broader range of information and results. Finally, variation both in prestressing load and contact shear strength across different models could add to the completeness and depth of the analysis.

Bibliography

- [1] Nawy Edward G. *Prestressed Concrete: A Fundamental Approach*. Pearson College, 2005.
- [2] Andrea E. Del Grosso. “Structural Health Monitoring: research and practice”. In: *Second Conference of Smart Monitoring* (2013).
- [3] K.F Faherty. “An Analysis of a Reinforced and a Prestressed Concrete Beam by Finite Element Method”. PhD thesis. University of Iowa, 1972.
- [4] H. A. Mang and G. Meschke. “Nonlinear finite element analysis of reinforced and prestressed concrete structures”. In: *Engineering Structures* 13.April (1991), pp. 211–225.
- [5] Jeeho Lee and Gregory L. Fenves. “Plastic-Damage Model for Cyclic Loading of Concrete Structures”. In: *Journal of Engineering Mechanics* 124.8 (1998), pp. 892–900.
- [6] Amir A. Arab, Sameh S. Badie, and Majid T. Manzari. “A methodological approach for finite element modeling of pretensioned concrete members at the release of pretensioning”. In: *Engineering Structures* 33.7 (2011), pp. 1918–1929.
- [7] P. K. Yapar O. Basu and N. Nordendale. “Accurate finite element modeling of pretensioned prestressed concrete beams”. In: *Engineering Structures* 101 (2015), pp. 163–178.
- [8] S.K. Padmarajaiah and Ananth Ramaswamy. “A finite element assessment of flexural strength of prestressed concrete beams with fiber reinforcement”. In: *Cement & Concrete Composites* 24.2 (2002), pp. 229–241.
- [9] Sasan Farhadi et al. “Prestressing wire breakage monitoring using sound event detection”. In: *Computer-Aided Civil and Infrastructure Engineering* 39.2 (2023), pp. 186–202.
- [10] Sasan Farhadi, Mauro Corrado, and Giulio Ventura. “Automated Acoustic Event-Based Monitoring of Prestressing Tendon Breakage in Concrete Bridges”. In: *Computer-Aided Civil and Infrastructure Engineering* (2024).
- [11] RILEM Technical Committee. “Recommendation of RILEM TC 212-ACD: acoustic emission and related NDE techniques for crack detection and damage

- evaluation in concrete Measurement Method for Acoustic Emission Signals in Concrete”. In: *Materials and Structures* 43 (2010), pp. 1177–1181.
- [12] RILEM Technical Committee. “Recommendation of RILEM TC 212-ACD: Acoustic Emission and Related NDE Techniques for Crack Detection and Damage Evaluation in Concrete Test method for damage qualification of reinforced concrete beams by acoustic emission”. In: *Materials and Structures* 43 (2010), pp. 1183–1186.
- [13] RILEM Technical Committee. “Recommendation of RILEM TC 212-ACD: acoustic emission and related NDE techniques for crack detection and damage evaluation in concrete Test Method for Classification of Active Cracks in Concrete Structures by Acoustic Emission”. In: *Materials and Structures* 43 (2010), pp. 1187–1189. DOI: 10.1617/s11527-010-9640-6.
- [14] J.N Reddy. *An Introduction to the Finite Element Method*. McGraw-Hill, Inc, 1994.
- [15] Klaus-Jürgen Bathe. *Finite Element Procedures*. Prentice Hall, 1996.
- [16] Klaus-Jürgen Bathe. “On a composite implicit time integration procedure for nonlinear dynamics”. In: *Computers and Structures* 83 (2005).
- [17] *LS-DYNA Keyword user’s Manual, Volume I*. 2007.
- [18] *LS-DYNA Support*. <https://www.dynasupport.com/faq/general/what-are-the-differences-between-implicit-and-explicit>. Accessed: 21/08/2024.
- [19] Karl Scheweizerhof. “Quasi-static Structural Analysis with LS-SYNA - Merits and Limits”. In: *CAD-FEM GmbH* (1999).
- [20] Terry C. Wallace Throne Lay. *Modern Global Seismology*. Elsevier, 1995.
- [21] *LS-DYNA Theory Manual*. 2022.
- [22] J. Burton J. Bonet. “A simple average nodal pressure tetrahedral element for incompressible and nearly incompressible dynamic explicit applications”. In: *Communications in Numerical Methods in Engineering* (1998).
- [23] et al Malcolm H. Ray. *Procedures for Verification and Validation of Computer Simulation Used for Roadside Safety Applications*. National Cooperative Highway Program, 2010.
- [24] Michael E. Plesha Robert D. Cook David S. Malkus. *Concepts and applications of finite element analysis*. John Wiley and Sons, 1988.
- [25] P. M. Knupp. “Remarks on Mesh Quality”. In: *Aerospace Science Meeting and Exhibit* (2007).
- [26] Cynthia. E. Dunning T. A. Burkhart D. M. Andrews. “Finite element modeling mesh quality, energy balance and validation methods: A review with recommen-

- dations associated with the modeling of bone tissue”. In: *Journal of Biomechanics*, Vol 46, Issue 9, Pgs 1477-1488 (2013).
- [27] C. A. Felippa. *Introduction to Finite Element Methods*. Department of Aerospace Engineering Science and Center for Aerospace Structures University of Colorado, 2004.
- [28] Costin Untaroiu. “A Finite Element Model of the Lower Limb for Simulating Pedestrian Impacts”. In: *Stapp Car Crash Journal*, Vol 49, Pages 157 - 181 (2005).
- [29] John R. Rice. “Is the Aspect Ratio Significant for Finite Element Problems?” In: *Computer Science Department Purdue University* (1985).
- [30] Alexander Planks Igor Tsukerman. “Comparison of Accuracy Criteria for Approximation of Conservative Fields on Tetrahedra”. In: *IEEE Transactions on Magnetism* (1998).
- [31] John Robinson. “CRE method for element testing and the jacobian shape parameters”. In: *Engineering computations* (1986).
- [32] ANSYS. https://ansyshelp.ansys.com/public/account/secured?returnurl=////////Views/Secured/corp/v242/en/wb_msh/msh_skewness.html. Accessed: 09/09/2024.
- [33] Andrey V. Kravtsov Nickolay Y. Gnedin Vadim A. Semenov. “Enforcing the Courant-Friedrichs-Lewy condition in explicitly conservative local time stepping schemes”. In: *Journal of Computational Physics* 359 (2018).
- [34] et al Hyunbin Jo. “Detailed assessment of mesh sensitivity dor CFD simulation of coal combustion in a tangential-firing boiler”. In: *Journal of Mechanical Science and Technology* 34 (2020).
- [35] *LS-DYNA Keyword user’s Manual, Volume II Material Models*. 2024.

Appendix

- **Appendix A:** Includes the input cards used for the LS-DYNA model
- **Appendix B:** Includes Figures showing nodal accelerations in time and frequency domain for the different realized models for different definitions of damping values

A Input Cards on LS-DYNA

The following appendix outlines the command cards used for the development of the model following the inputs from [35], and [17]. Input units are meters, kilograms, and seconds, the "-" over a parameters means it's being unused, so default values are introduced.

Command:

CONTACT_AUTOMATIC_SURFACE_TO_SURFACE_TIEBREAK

Card:

Variable	OPTION	NFLS	SFLS	PARAM	ERATEN	ERATES	CT2CN	CN
Type	9	$2 * 10^6$	$2 * 10^6$	1	$1 * 10^4$	$1 * 10^4$	1	$2 * 10^9$

Where:

- OPTION 9: Defines a discrete crack model type of contact
- NFLS: Normal failure stress
- SFLS: Shear failures stress
- PARAM: 1 when shell thickness offsets are to be ignored
- ERATEN: Normal energy release rate
- ERATES: Shear energy release rate
- CT2CN: Ratio tangential stiffness to the normal stiffness
- CN: Normal stiffness

Command:

CONTACT_TIED_SURFACE_TO_SURFACE_CONSTRAINED_OFFSET

Card:

4

Variable	SSID	MSID	STYP	MSTYP	SBOXID	MBOXID	SPR	MPR
Type	SET ID	SET ID	-	-	-	-	-	-

5

Variable	FS	FD	DC	VC	VDC	PENCHK	BT	DT
Type	-	-	-	-	-	-	0	**

6

Varibale	SFS	SFM	SST	MST	SFST	SFMT	FSF	VSF
Type	-	-	-1	-1	-	-	-	-

Where:

- SSID: Slave segment set ID
- MSID: Master segment set ID
- BT: Birth time
- DT: Death time (** longer than the termination time for Plate - Concrete contact, 0.002 seconds for Steel A - Steel B contact = time of tendon breakage)
- SST: Thickness of slave surface (negative value for determination if nodes are tied)
- MST: Thickness of master surface (negative value for determination if nodes are tied)

Command:

INITIAL_STRESS_SOLID_SET

Cards:

1

Variable	SID	NINT	NHISV	LARGE	IVEFLG	IALEGP	NTHINT	NTHHSV
Type	SET ID	1	-	-	-	-	-	-

2

Variable	SIGXX	SIGYY	SIGZZ	SIGXY	SIGYZ	SIGZX	EPS
Type	-	-	$8 * 10^8$	-	-	-	-

Where:

- SID: Solid set ID
- NINT: Number of integrations points
- SIGZZ: Initial stress 33 component

Command:

MAT_ELASTIC

Cards:

1

Where:

Variable	MID	RO	E	PR	DA	DB	NOT USED
Type	MAT ID	**	**	**	-	-	-

** Refer to Subsection 5.1.3 for specific values depending on the material defined

- MID: Material ID
- RO: Mass density
- E: Young's Modulus
- PR: Poisson's ratio

Command:

DAMPING_PART_STIFFNESS

Card:

1

Variable	PID	COEF
Type	PART ID	**

** Refer to Subsection 5.1.6 (Damping Definition) for specific values depending on the model

Where:

- PID: Part ID
- COEF: Rayleigh damping coefficient

Command:

DAMPING_GLOBAL

Card:

1

Variable	LCID	VALDMP	STX	STY	STZ	SRX	SRY	SRZ
Type	-	**	-	-	-	-	-	-

** Refer to Subsection 5.1.6 (Damping Definition) for specific values depending on the model

Where:

- VALDMP: System damping constant

B Nodal Accelerations

The following appendix presents the results obtained from the different models (7 in total), with the key variations being the damping parameters. These variations include both the damping values — 0%, 2%, and 4% — and the types of damping applied: stiffness proportional damping and mass proportional damping.

Model 1: $\zeta_K = 0\%$, and $\zeta_M = 0\%$

Nodes in concrete:

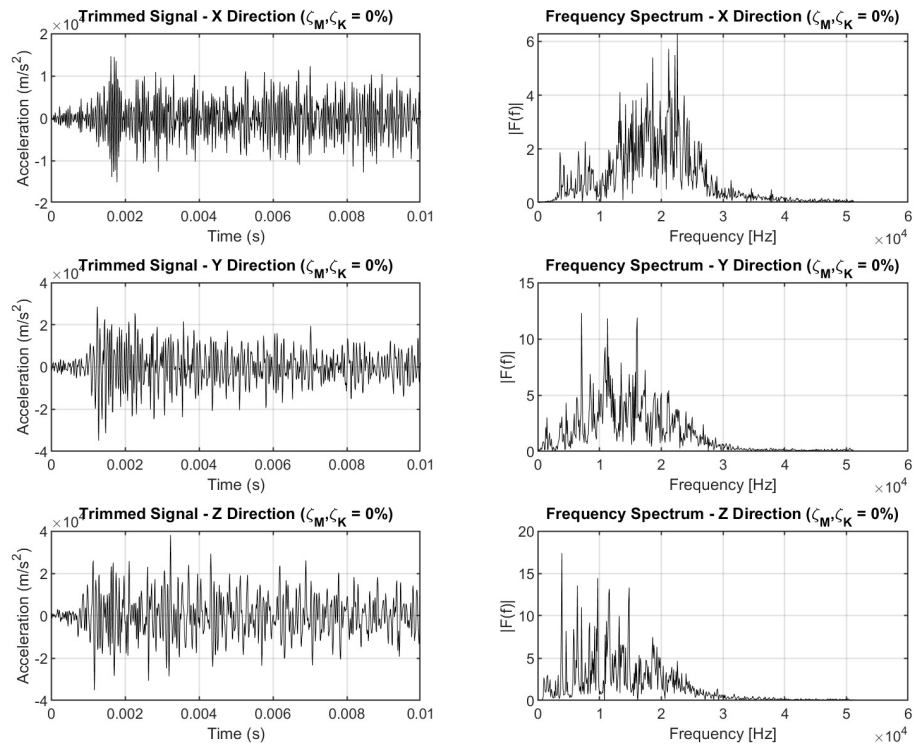


Figure 1: Acceleration of node A, $\zeta = 0\%$

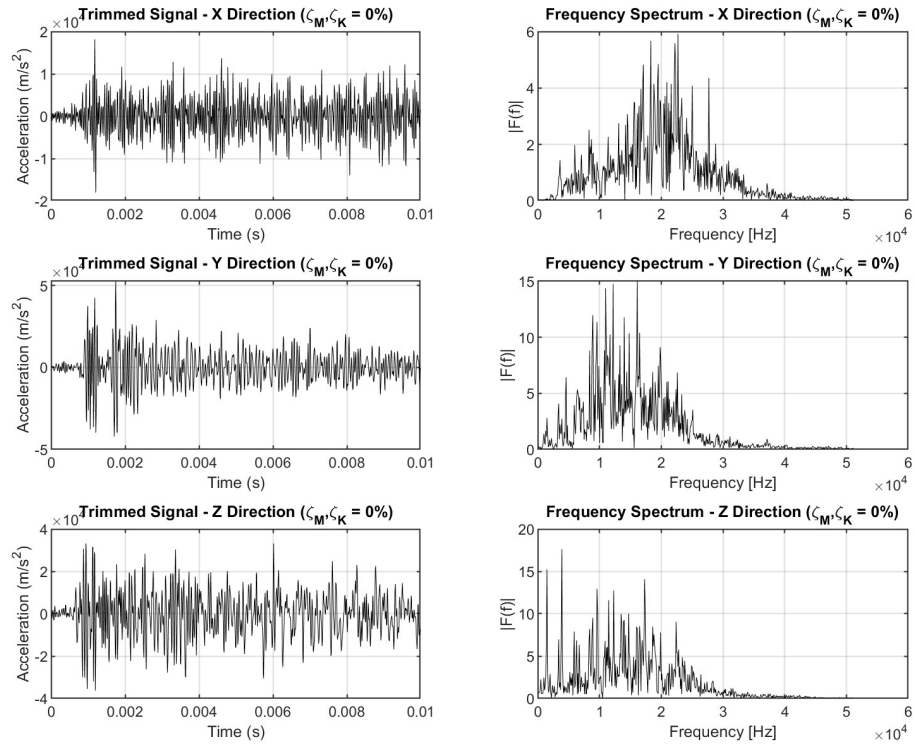


Figure 2: Acceleration of node B, $\zeta = 0\%$

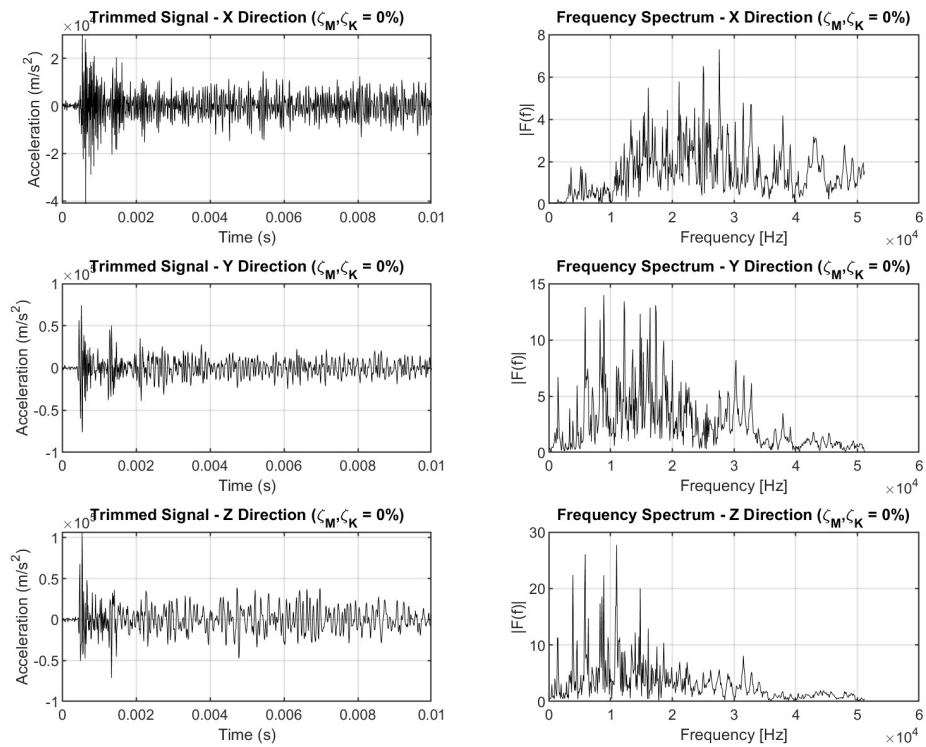


Figure 3: Acceleration of node C, $\zeta = 0\%$

Model 2: $\zeta_K = 2\%$, and $\zeta_M = 0\%$

Nodes in concrete:

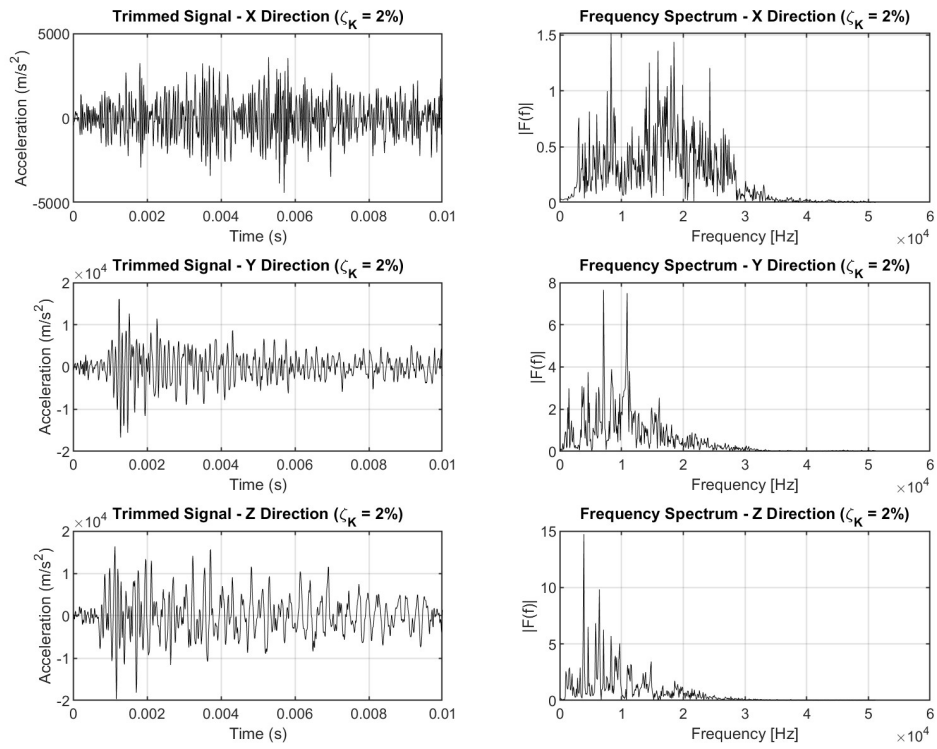


Figure 4: Acceleration of node A, $\zeta_K = 2\%$

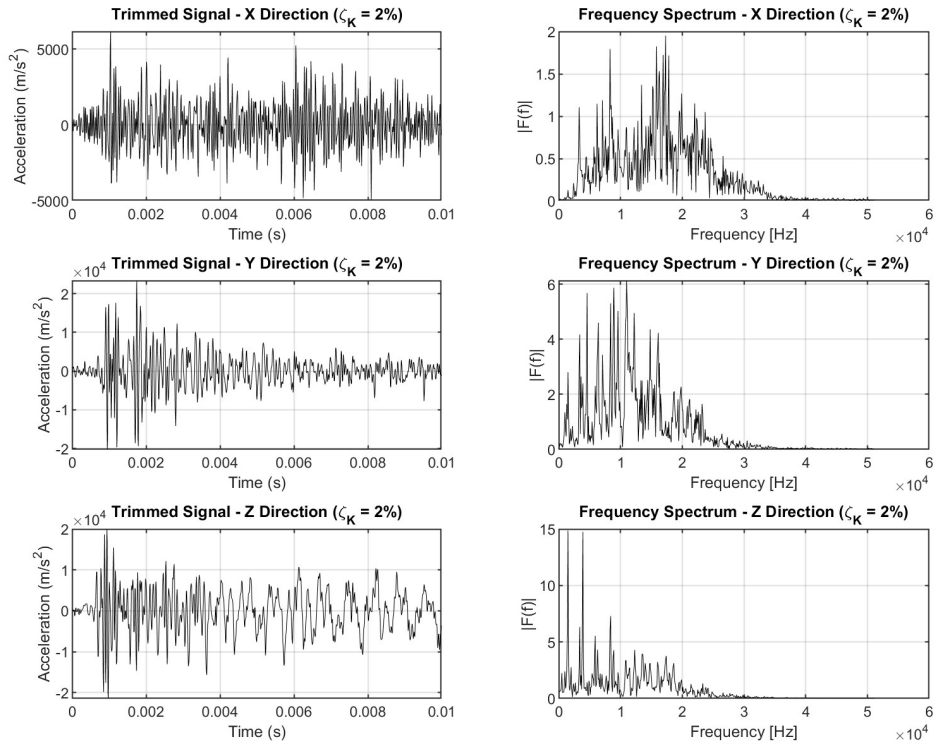


Figure 5: Acceleration of node B, $\zeta_K = 2\%$

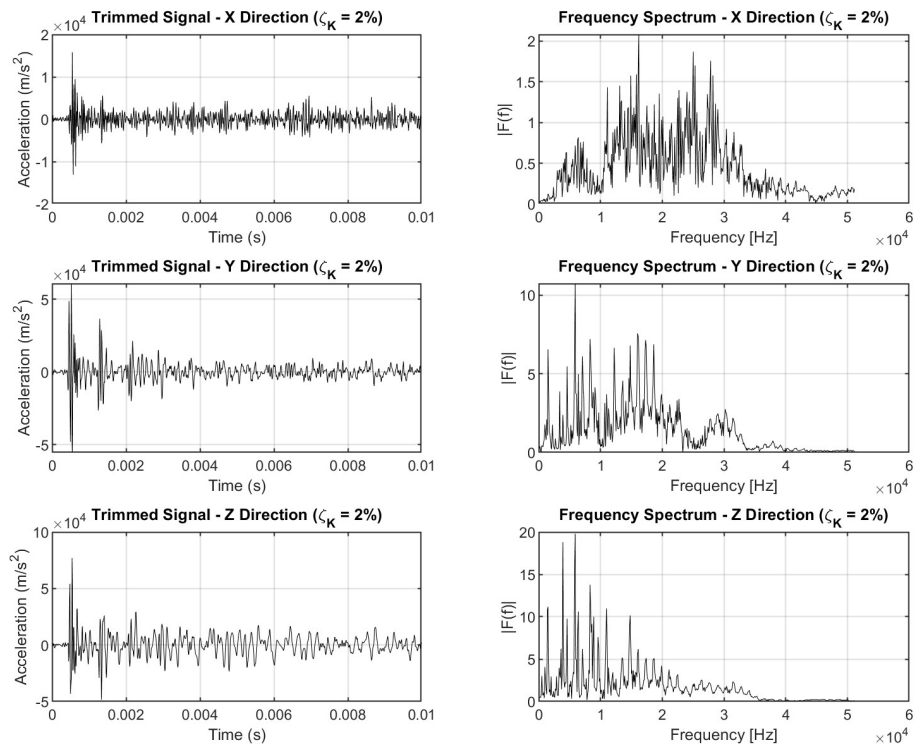


Figure 6: Acceleration of node C, $\zeta_K = 2\%$

Model 3: $\zeta_K = 4\%$, and $\zeta_M = 0\%$

Nodes in concrete:

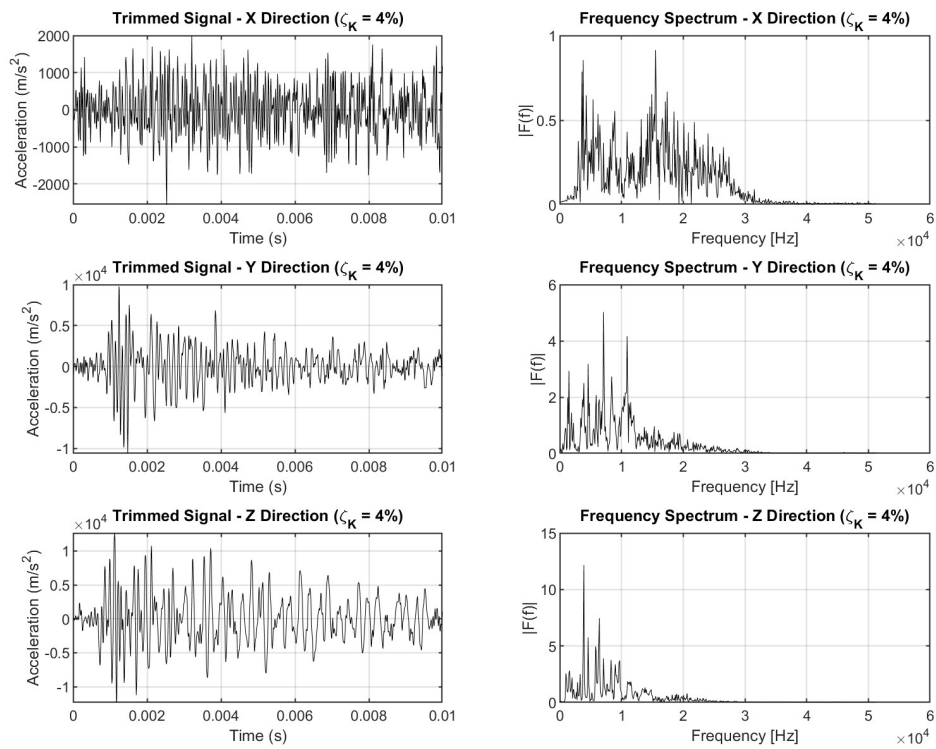


Figure 7: Acceleration of node A, $\zeta_K = 4\%$

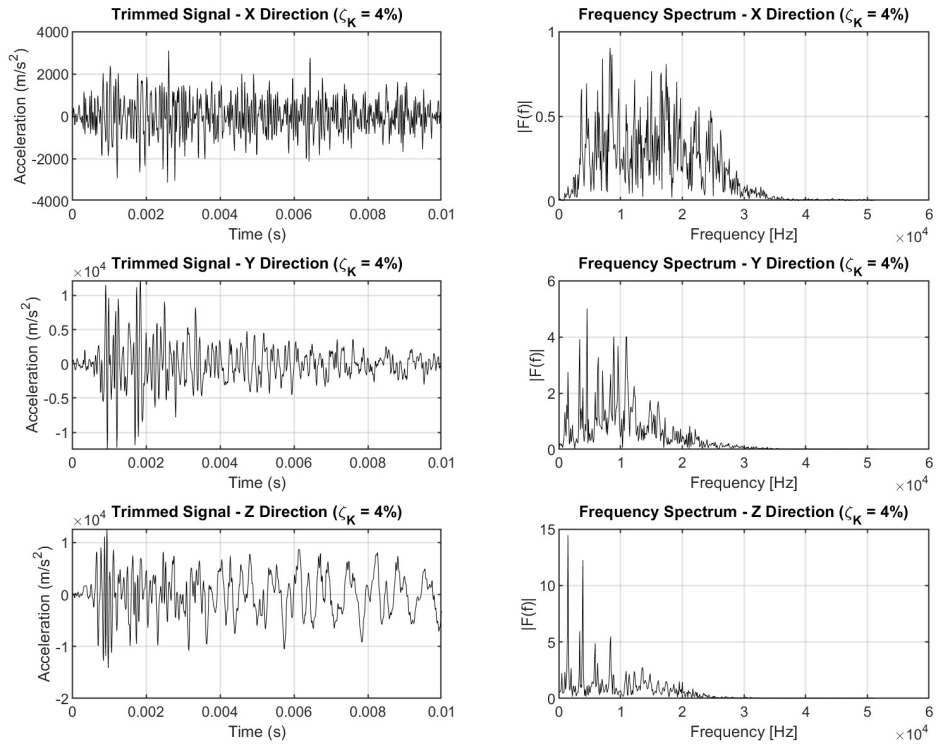


Figure 8: Acceleration of node B, $\zeta_K = 4\%$

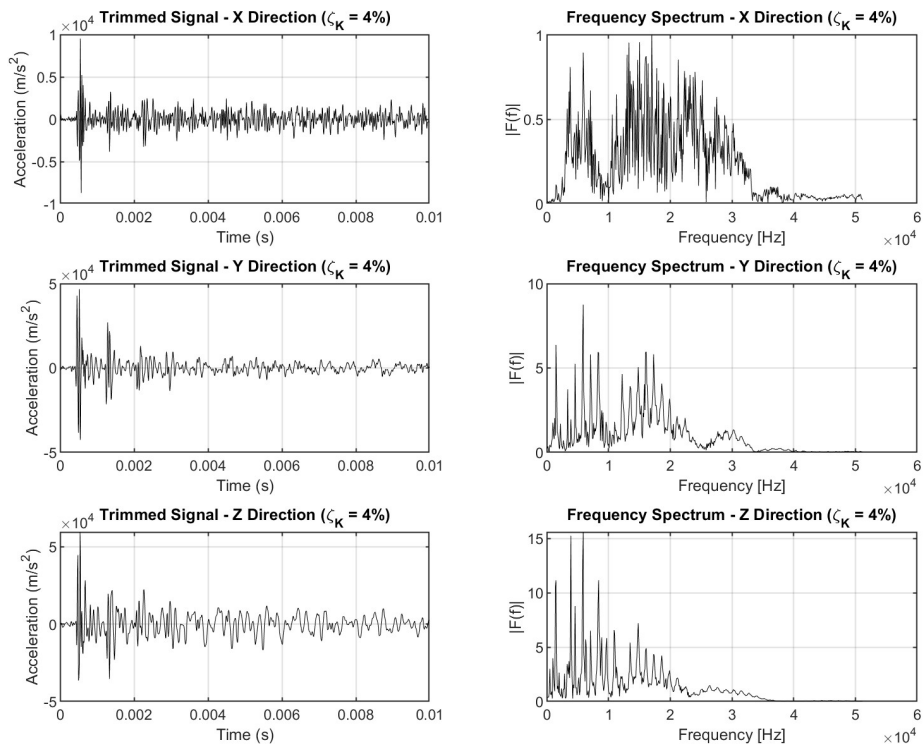


Figure 9: Acceleration of node C, $\zeta_K = 4\%$

Model 4: $\zeta_K = 0\%$, and $\zeta_M = 2\%$

Nodes in concrete:

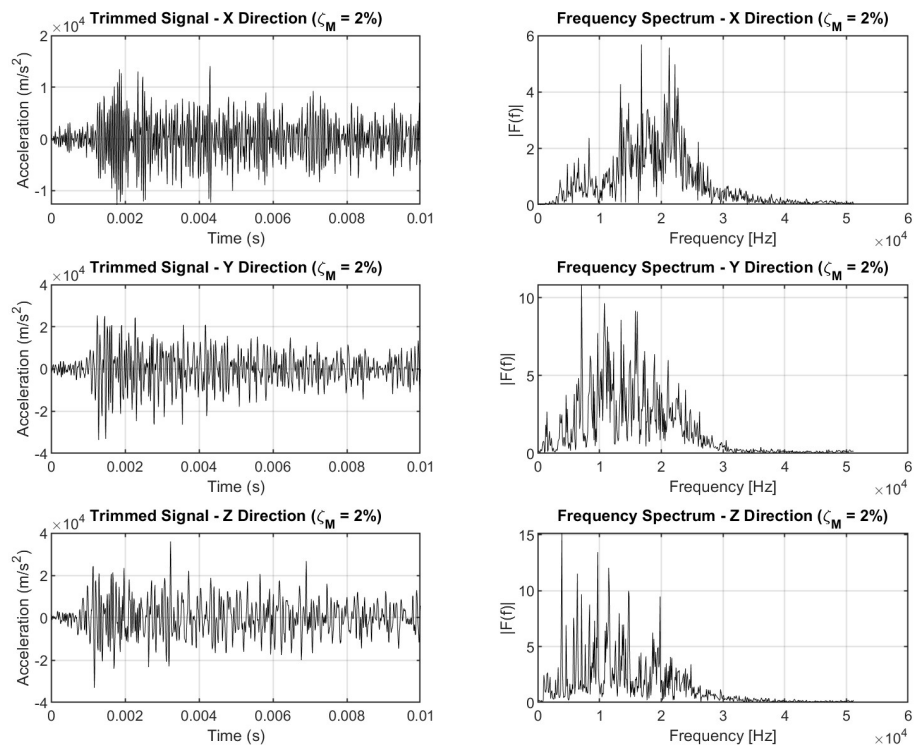


Figure 10: Acceleration of node A, $\zeta_M = 2\%$

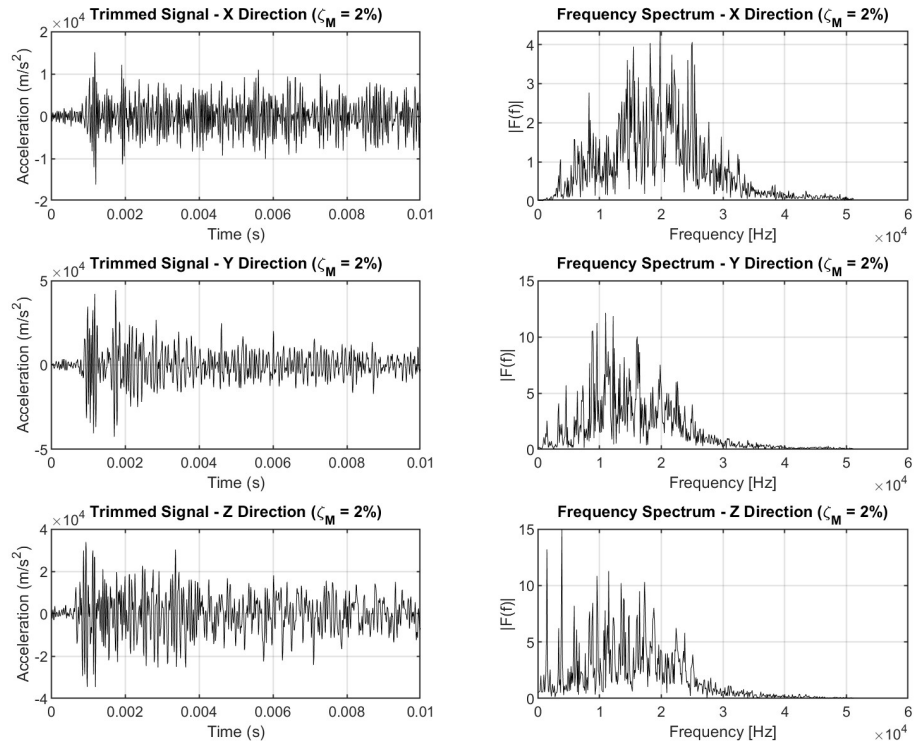


Figure 11: Acceleration of node B, $\zeta_M = 2\%$

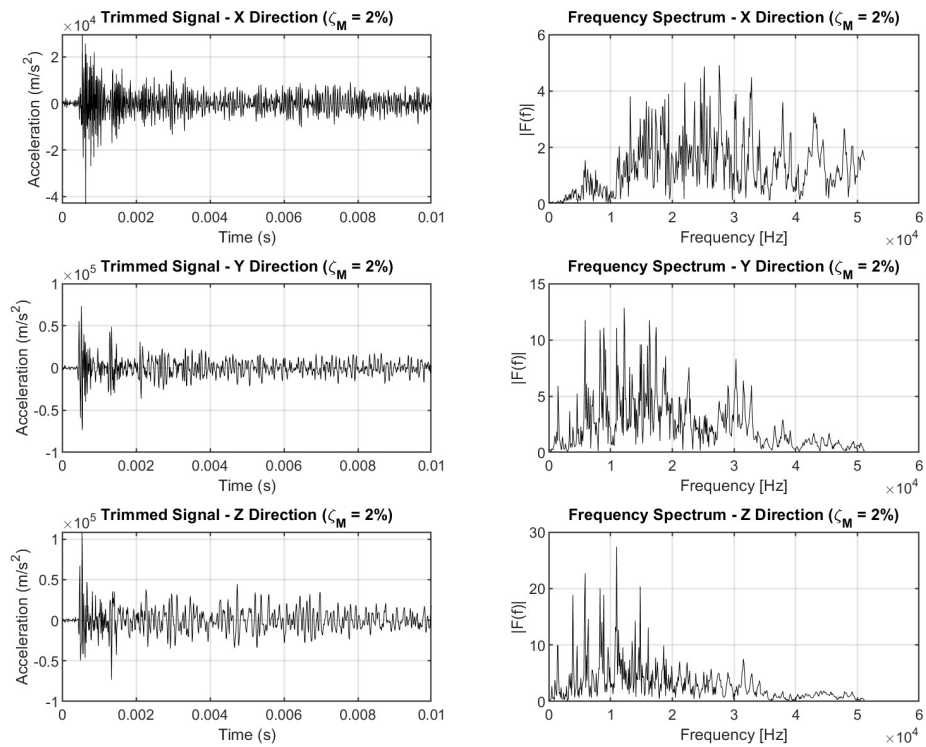


Figure 12: Acceleration of node C, $\zeta_M = 2\%$

Model 5: $\zeta_K = 0\%$, and $\zeta_M = 4\%$

Nodes in concrete:

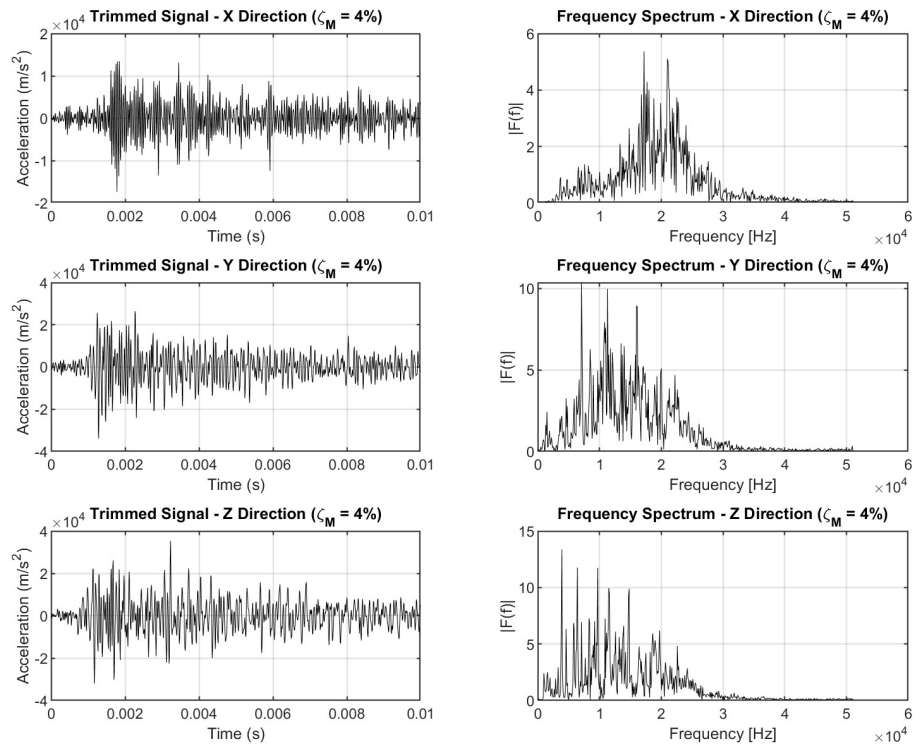


Figure 13: Acceleration of node A, $\zeta_M = 4\%$

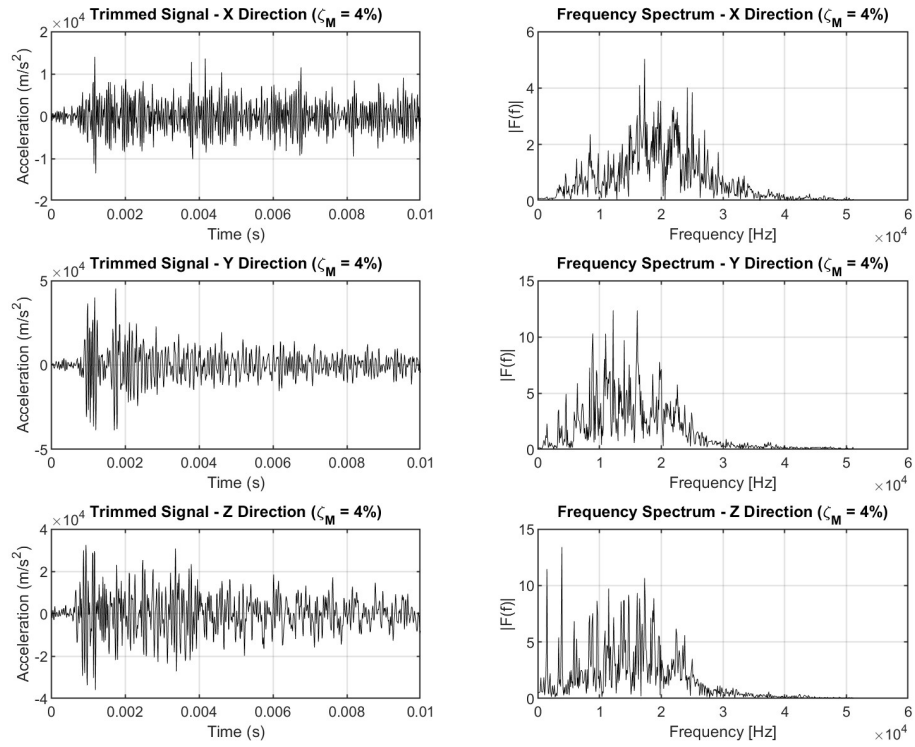


Figure 14: Acceleration of node B, $\zeta_M = 4\%$

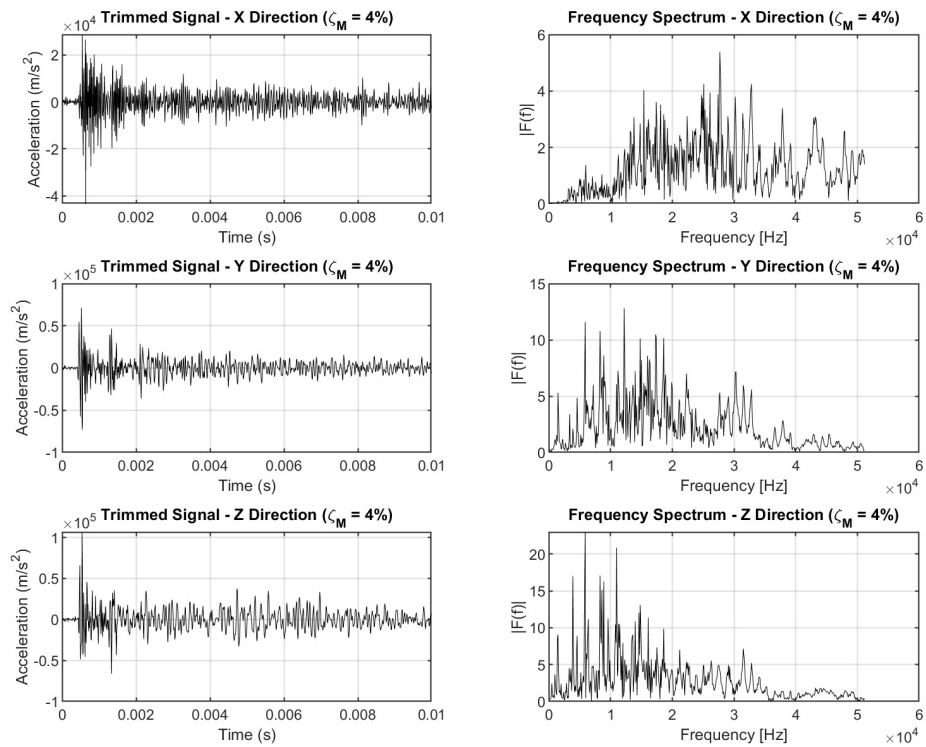


Figure 15: Acceleration of node C, $\zeta_M = 4\%$

Model 6: $\zeta_K = 2\%$ and $\zeta_M = 2\%$

Nodes in concrete:

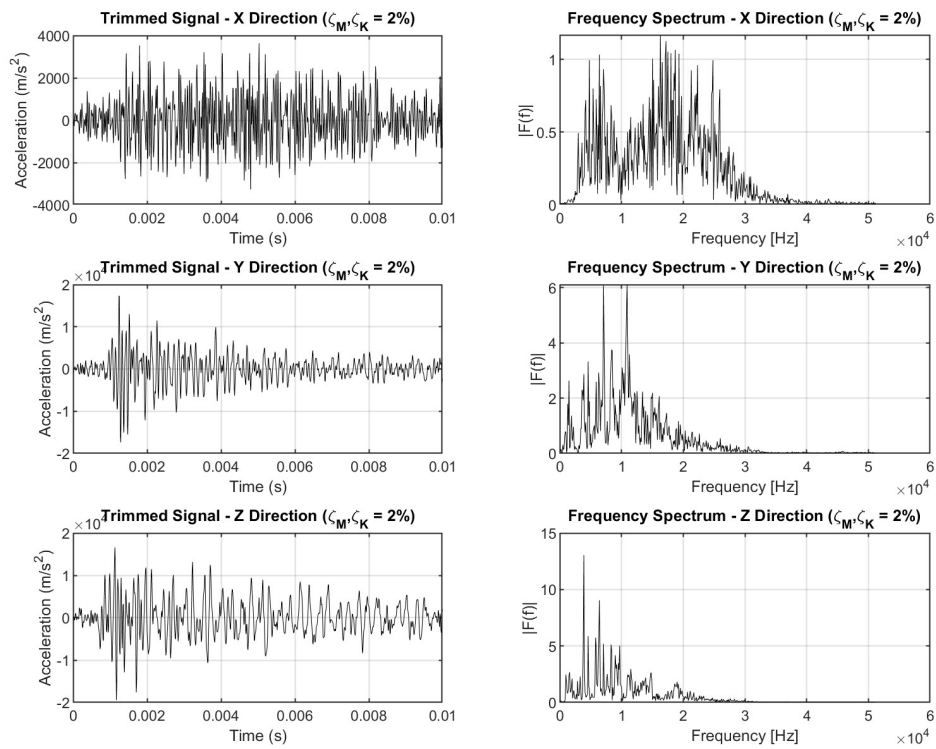


Figure 16: Acceleration of node A, $\zeta_M = 2\%$, $\zeta_K = 2\%$

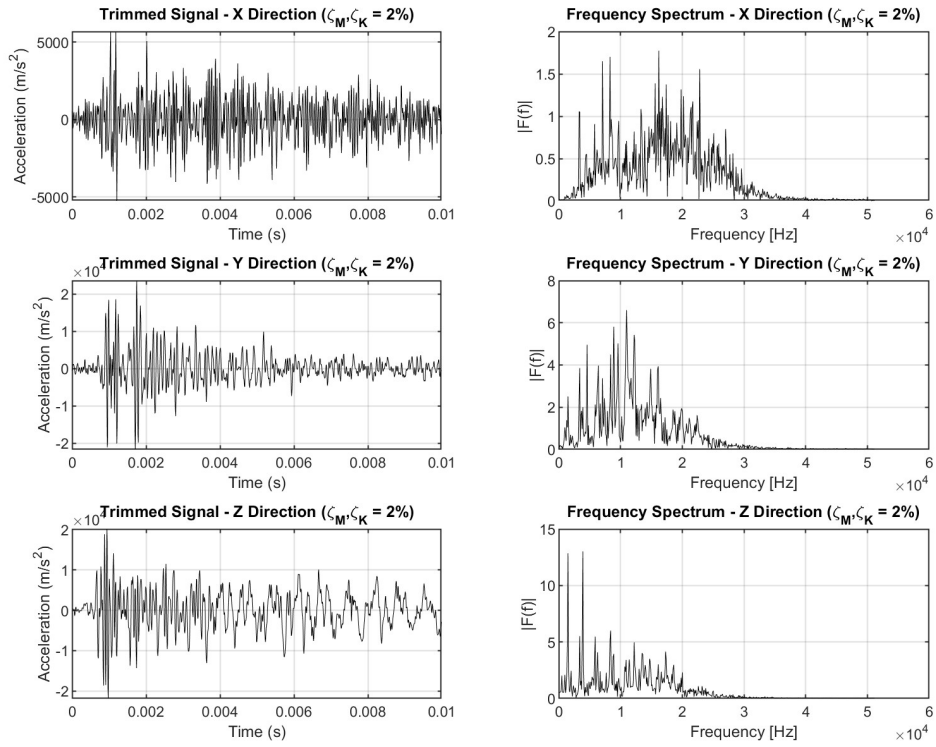


Figure 17: Acceleration of node B, $\zeta_M = 2\%$, $\zeta_K = 2\%$

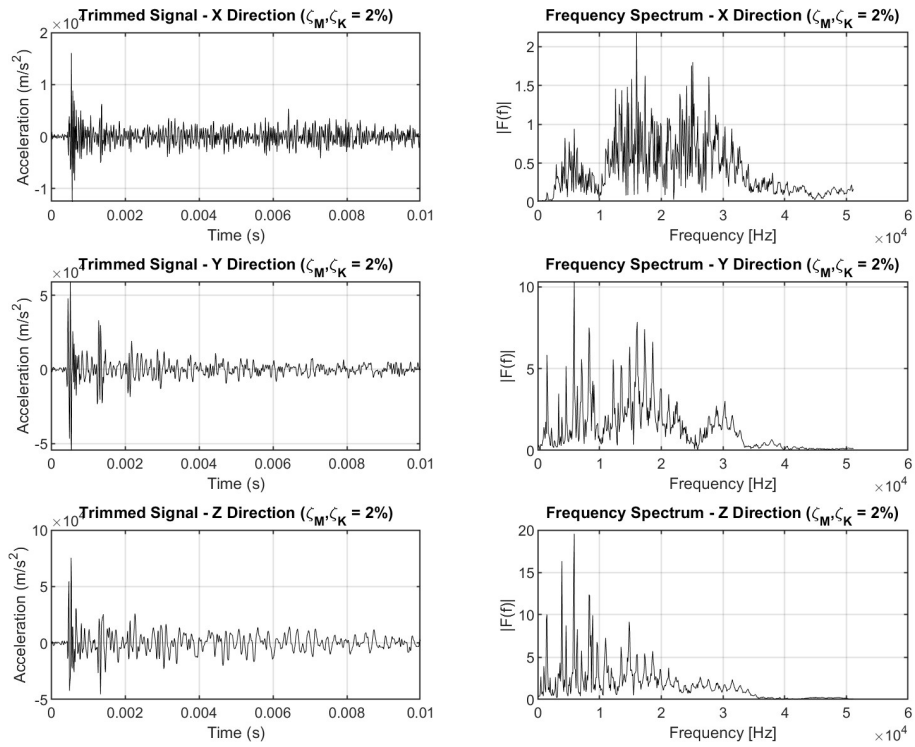


Figure 18: Acceleration of node C, $\zeta_M = 2\%$, $\zeta_K = 2\%$

Model 7: $\zeta_K = 4\%$ and $\zeta_M = 4\%$

Nodes in concrete:

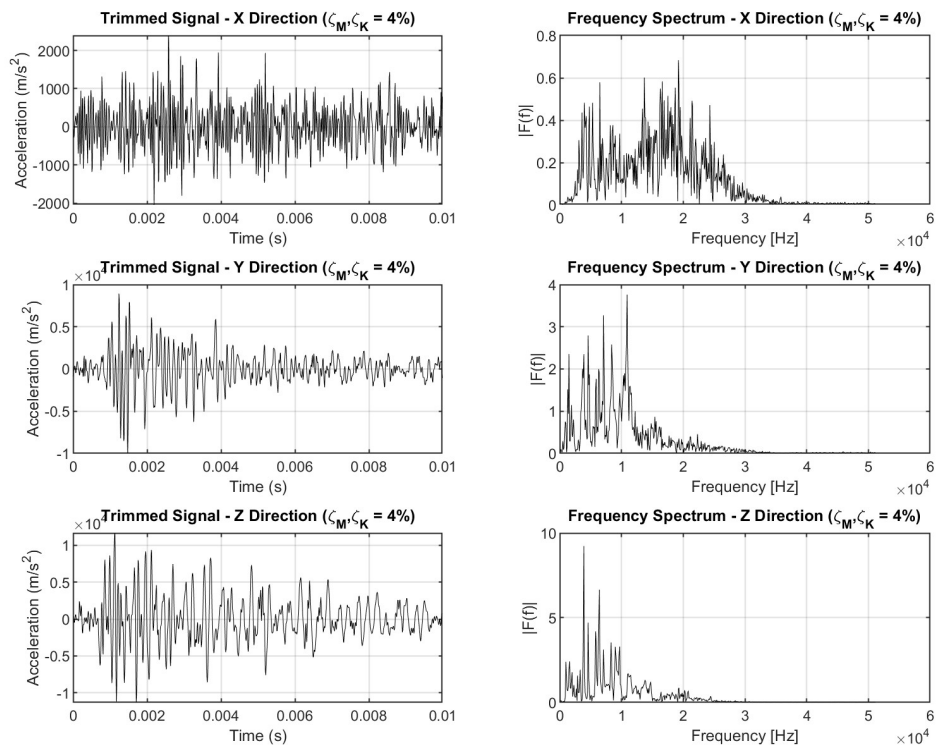


Figure 19: Acceleration of node A, $\zeta_M = 4\%$, $\zeta_K = 4\%$

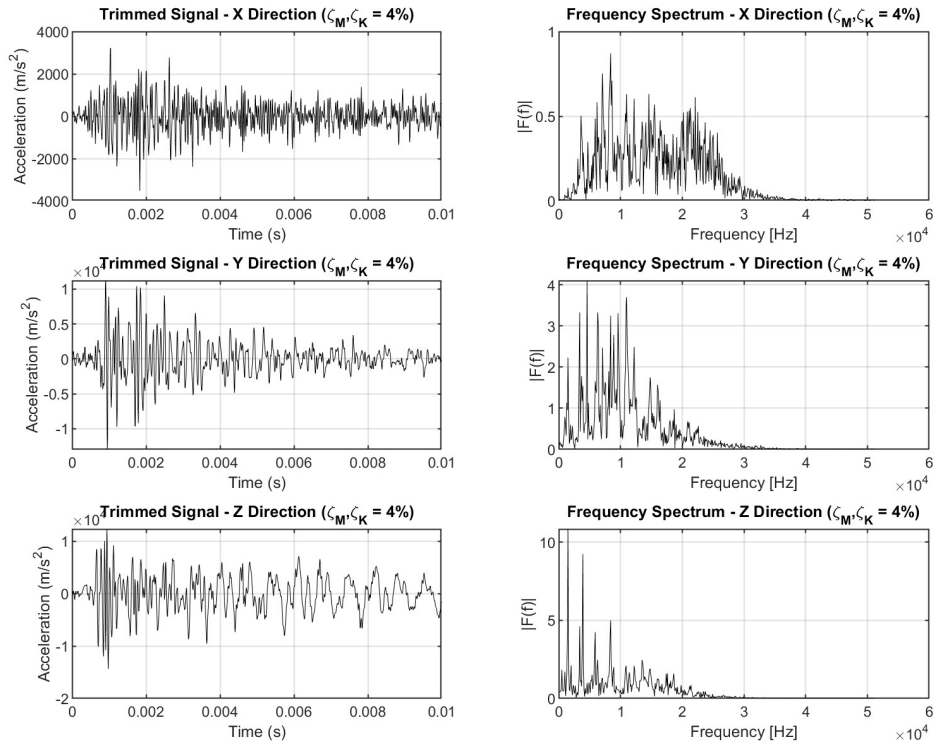


Figure 20: Acceleration of node B, $\zeta_M = 4\%$, $\zeta_K = 4\%$

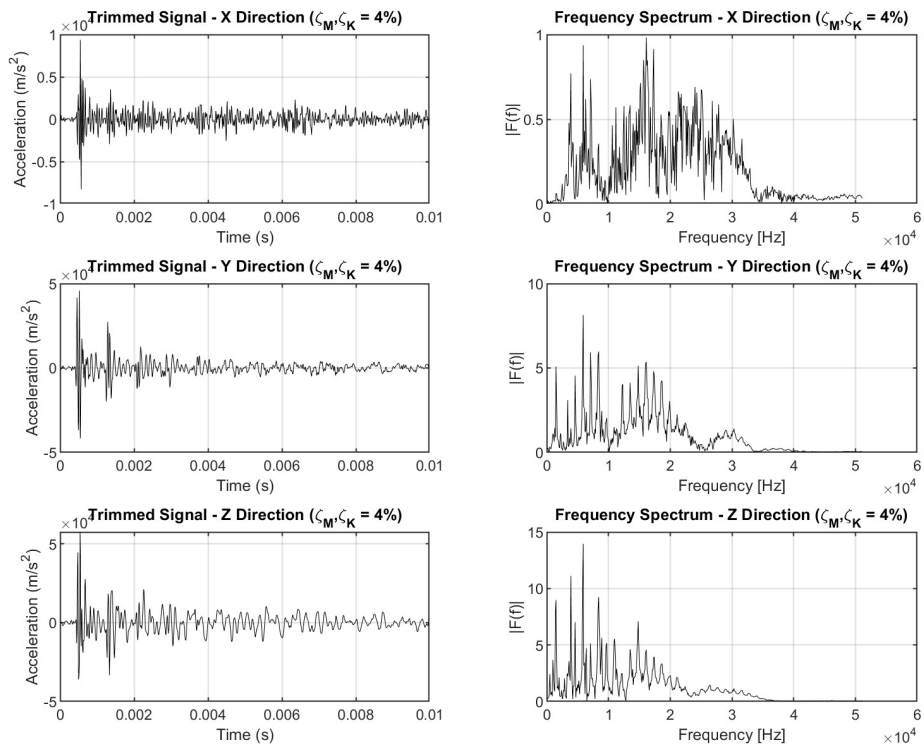


Figure 21: Acceleration of node C, $\zeta_M = 4\%$, $\zeta_K = 4\%$